Laboratory and Field Characterization of Additive-Modified Asphalt Concrete Mixtures

by

Matthew Hampton Kmetz

A thesis submitted to the Graduate Faculty of
Auburn University
in partial fulfillment of the
requirements for the Degree of
Master of Science

Auburn, Alabama
December 9, 2023

Keywords: Asphalt additives, Asphalt mixture testing, Pavement instrumentation

Approved by

Dr. David Timm, Chair, Brasfield & Gorrie Professor Civil and Environmental Engineering
Dr. Fan Yin, Assistant Director and Research Professor National Center for Asphalt Technology
Dr. Benjamin Bowers, Associate Professor Civil and Environmental Engineering

ABSTRACT

There is a need for a more rapid system of evaluation and implementation for new and existing asphalt additives, especially due to the prohibitive cost of full-scale performance evaluations. To help to meet this need, the Additive Group (AG) experiment at the National Center for Asphalt Technology (NCAT) was developed. A comprehensive laboratory evaluation of six asphalt mixtures has been completed. Each mixture was modified with a popular additive type that was selected by the AG's state DOT sponsors. Simultaneously, full-scale test sections were constructed at the NCAT Test Track to evaluate the field performance and structural behavior of each modified mixture. Trafficking of these test sections began in the Fall of 2021 and is currently underway at the writing of this thesis. Trafficking is estimated to be completed in 2024, at which point a framework for rapid additive evaluation, the primary goal of the AG experiment, will be developed. This thesis presents the completed laboratory evaluation of each AG mixture via dynamic modulus (E*), direct tension cyclic fatigue, and bending beam fatigue testing. Additionally, pavement layer strain response measurements, performance data (rutting, cracking, and ride quality), and backcalculated layer moduli gathered from the full-scale test sections are presented within this thesis. All Test Tack data presented was gathered from the beginning of trafficking through June 2023. Relevant links between the laboratory and field-testing results were established. Finally, a layered-elastic simulation tool was used to model strain responses of the pavement sections using their in-situ layer moduli and surveyed layer thicknesses. Key findings within this thesis included the following: For the AG mixtures, average initial flexural stiffness provided a better correlation with backcalculated pavement modulus and measured pavement strain response in comparison to average dynamic modulus (E*). WESLEA simulated strain responses (using the surveyed layer thicknesses and backcalculated layer moduli for each test section) closely approximated the measured strain responses (with the exception of the control section). Through June 2023, the S_{app} parameters computed for each AG mixture have not provided good agreement with the observed levels of cracking in the field. However, computing the number of cycles to failure (N_f) for each mixture, using its individual fatigue life transfer function (from beam fatigue testing) and its average measured thickness- and temperature-corrected strain response ($\mu\varepsilon_{cor}$), provided good agreement with the observed levels of cracking so far.

ACKNOWLEDGEMENTS

I would like to express my gratitude towards my graduate advisor, Dr. David Timm, who provided excellent technical guidance and support throughout the development of this thesis. Additionally, I would like to extend my thanks to the other members of my advisory committee, Dr. Fan Yin and Dr. Benjamin Bowers. Also, I'd like to thank Meagan Foshee for her diligent work on her thesis regarding the AG experiment, much of which provided a foundation for my own. Matthew Sasser, Juliana Wood, Hayden Harding, Amir Rahimzadeh also played an invaluable role in data collection and processing for the full-scale test sections. Finally, I'd like to thank my family for their continued support throughout my time at Auburn University.

TABLE OF CONTENTS

LIST OF TABLES

LIST OF FIGURES

LIST OF ABBREVIATIONS

4PB	Four-Point Bending
AASHTO	American Association of State Highway and Transportation Officials
AC	Asphalt Concrete
AG	Additive Group
AMPT	Asphalt Mixture Performance Tester
ASG	Asphalt Strain Gauge
ASTM	American Society for Testing and Materials
BBFT	Bending Beam Fatigue Test
C	Pseudo Secant Modulus
DOT	Department of Transportation
D^R	Pseudo Energy-Based Fatigue Failure Criterion
E*	Dynamic Modulus
E_{68}	Temperature-Normalized Backcalculated AC Modulus
E_{AC}	Backcalculated AC Modulus
E_{GB}	Backcalculated Granular Base Modulus
EPC	Earth Pressure Cell
ESAL	Equivalent Single Axle Loads
$E_{Subgrade}$	Backcalculated Subgrade AC Modulus
FWD	Falling Weight Deflectometer
GB	Granular Base
G-R_m	Glover-Rowe Parameter
GTR	Ground Tire Rubber
IRI	International Roughness Index
LVDT	Linear Variable Differential Transformer
MESALs	Million ESALs
NCAT	National Center for Asphalt Technology

N_f	Number of Cycles to Failure
NMAS	Nominal Maximum Aggregate Size
PCR	Post-Consumer Recycled
PG	Performance Grade
PMLC	Plant-Mixed Laboratory-Compacted
QC	Quality Control
R^2	Coefficient of Determination
RAP	Reclaimed Asphalt Pavement
rPE	Recycled Polyethylene
S	Internal Damage
S_{app}	Cyclic Fatigue Index Parameter
SBS	Styrene-Butadiene-Styrene
SGC	Superpave Gyratory Compactor
S-VECD	Simplified Viscoelastic Continuum Damage
α	Level of Significance
$\mu\varepsilon_{68}$	Temperature-Normalized 95th Percentile Microstrain Response
$\mu\varepsilon_{AC}$	95th Percentile Microstrain Response
$\mu\varepsilon_{cor}$	Thickness-Corrected and Temperature-Normalized 95th Percentile Microstrain Response

CHAPTER 1

Introduction

1.1: Background

Asphalt additives aim to enhance the overall performance and longevity of flexible pavements, and often utilize sustainable, recycled materials. Alternatively, asphalt additives may be used to maintain similar pavement performance while reducing overall cost. Several additive technologies, including post-consumer recycled (PCR) plastics, recycled ground tire rubber (GTR), and fibers have gained popularity over the years. These additive technologies, as well as many others, are frequently marketed to state agencies and contractors with the potential of performance enhancements, cost reductions, or both. While full-scale field testing may be able to validate these claims, it is both cost prohibitive and time consuming, and is an impractical method for evaluating every prospective additive technology. Often, once agencies have become comfortable enough with an additive technology to allow its widespread use, new technologies have already emerged. Therefore, there is an industry-wide need for a more rapid system to accurately evaluate new, and existing, additive technologies.

The Additive Group (AG) experiment, begun in 2021 at the National Center for Asphalt Technology (NCAT) Pavement Test Track, aims to addresses this need by providing a comprehensive laboratory analysis and full-scale field evaluation of a range of additive technologies selected by the state Department of Transportation (DOT) sponsors of the AG experiment. The additive group experiment has been divided into three distinct phases. Phase I of the experiment involved a preliminary laboratory evaluation and predictive structural analysis of ten asphalt mixtures, each modified with popular additive technologies (including those mentioned above). Additionally, an unmodified control mixture and an SBS-modified control mixture were evaluated. The AG's state DOT sponsors selected five modified-mixtures and one control mixture. The modified mixtures that were selected included a wet & dry-process rubber, a dry-process aramid fiber, and wet & dry-process plastic modified mixtures. The SBS-modified was selected for the control mixture. The final selected mixtures represented a wide range of technologies in use by state agencies. Further details regarding Phase I of the AG Experiment have been published previously (Timm et al., 2022)

Phase II of the AG Experiment featured construction of the sections, with embedded instrumentation, in the summer and fall of 2021. After construction, heavy vehicles provided accelerated trafficking to the AG test sections. Each section was instrumented in order to measure the tensile strain at bottom of the AC layer to be linked to cracking performance. Performance data were recorded for each test section, including cracking percentage, rutting depth, and ride quality on a weekly basis. Falling weight deflectometer (FWD) testing was performed several times per month to monitor the in-situ moduli of the subgrade, granular base, and asphalt concrete (AC) layers. Further details regarding the construction and instrumentation of the AG test sections have been published previously (Foshee, 2022).

Phase III the AG Experiment began in the Spring of 2022 and is currently ongoing at the time of writing. It involved the laboratory characterization (concluded) of the AG mixtures as well as

monitoring of the full-scale test sections (on-going). The laboratory characterization of the plant-mixed laboratory-compacted (PMLC) mixtures included the dynamic modulus (E*) test, direct tension cyclic fatigue test, and bending beam fatigue test. These tests primarily provide modulus, phase angle, and fatigue characterizations for the mixtures. Additionally, the results of laboratory testing were linked with the pertinent data available from the full-scale test sections. Test Track data gathered through June 2023 are presented in this thesis. Trafficking of the AG sections is expected to conclude in the spring of 2024, when a complete investigation linking the laboratory and field results will be conducted.

1.2: Objectives

Given the context of the AG Experiment as a whole, the primary objectives of this specific thesis were to:

- Provide a comprehensive laboratory characterization of the AG asphalt mixtures.
- Evaluate the performance data, backcalculated layer moduli, and strain responses that were recorded from the full-scale AG test sections though June 2023 (6.19 million ESALs).
- Establish relevant links between the results of the laboratory testing and available field data.

1.3: Scope of Work

In order to achieve these objectives, full-scale test sections were constructed for each of the modified mixtures. These test sections were instrumented with asphalt strain gauges (ASGs) and thermocouple temperature probes to measure the strain response of each section during trafficking as well as apply a temperature normalization. Heavy weight vehicles were used to provide accelerated trafficking to the sections, and performance data (rutting, cracking, and ride quality measurements) were recorded via a Pathways van. The AC, granular base, and subgrade in-situ layer moduli were backcalculated using EVERCALC 5.0 from falling wight deflectometer (FWD) data. The laboratory testing was conducted on plant-mixed, laboratory-compacted (PMLC) test specimens, the asphalt mixtures for which were each sampled during the construction of their respective full-scale test section. Standard AASHTO procedures were followed during the sampling of the mixtures and the preparation of the test specimens. The suite of laboratory tests included the dynamic modulus (E*) test (AASHTO TP 132-19), direct tension cyclic fatigue test (AASHTO TP 133-22), and bending beam fatigue test (AASHTO T321-22). In total, five additive technologies were evaluated, including a wet and dry-process rubber, a dry-process aramid fiber, and a wet and dry-process plastic. Each asphalt mixture utilized an identical dense-graded mixture design. Within this thesis, laboratory and field data are organized by additive type (i.e., rubber, fiber, and plastic) and referenced versus the SBS-modified control mixture were applicable.

1.4: Organization of Thesis

Chapter 2 provides a literature review regarding the additive technologies featured in this study. Additionally, it cites previous studies that evaluated similar additive technologies via the same laboratory tests conducted as a part of Phase III. Chapter 3 details the asphalt mixture designs, the AASHTO procedures followed during laboratory testing, and the pertinent data analysis tools. Chapter 4 provides a comprehensive overview of the laboratory testing results and how they relate to many of the studies cited in Chapter 2. Chapter 5 gives an overview of the NCAT Test Track trafficking methods, the as-built properties of each AG test section, and the methods followed for data processing. Chapter 6 details the performance, backcalculation, and strain data for each AG test section through June 2023. Chapter 7 establishes relevant links between the laboratory results presented in Chapter 4 and the field results presented in Chapter 6. Finally, Chapter 8 summarizes the findings of this thesis and provides recommendations for future research as it pertains to the AG experiment.

CHAPTER 2

Laboratory Testing – Literature Review

2.0: Introduction

The introduction of additives often modifies the characteristics and performance of an asphalt mixture. Depending on the additive type, dosage rate, or even modification method, the degree of asphalt mixture performance and/or behavior modification will vary. The AG Experiment investigated five different additive technologies, including their effects on laboratory and field performance. These technologies included a wet-process and dry-process recycled ground tire rubber (GTR), wet-process and dry-process post-consumer recycled (PCR) plastics, and dry-process aramid fibers. *Table 3.2.1* in the following chapter provides a comprehensive breakdown of the additive technologies used for each mixture, their dosage rates, and the final asphalt binder performance grades (PGs). This chapter will provide a brief overview of each additive technology and its documented effects on the suite of laboratory tests conducted as a part of the AG experiment.

2.1: Additive Technology Overview

The additive technologies evaluated in this study included wet and dry-process recycled ground tire rubber (GTR), dry-process aramid fibers, and wet and dry-process post-consumer recycled (PCR) plastic. GTR, commonly referred to as “crumb rubber” is most often sourced from PCR “scrap” tires and may be incorporated into an asphalt mixture through wet or dry processes. Under the wet-process, asphalt binder is modified with GTR prior to its introduction with the aggregate at the mixture plant. An asphalt binder is “terminally blended” if it was modified via the wet-process at the asphalt binder distribution terminal rather than on-site at the mixture plant. Alternatively, a dry-process GTR mixture is one that has had the crumb rubber added directly to the heated aggregate inside the mixing drum, before the introduction of any asphalt binder. As previously shown by Foshee, 2022, *Figure 2.1.1* and *Figure 2.1.2* provide examples of wet and dry-process GTR additives, respectively.

Figure 2.1.1: Typical Wet-Process GTR Additive ("Scrap Tires in Asphalt", 2021)

Figure 2.1.2: Dry-Process "SmartMix™" GTR Additive ("SmartMix", 2021)

Fiber modification is most commonly performed via the dry-process due to the relative ease and potential complications with mixture plant equipment that could occur if wet-process modification was used. Though many types of fibers have been investigated for their potential benefits to asphalt mixtures (including glass, cellulose, and many polymer-based fibers), aramid fibers were the type featured in the AG study. *Figure 2.1.3* provides an example of the specific dry-process ACE XP™ aramid fibers that were used. According to the manufacturer, each fiber strand pictured contains over 10,000 individual fibers, which are evenly dispersed within the mixture as the wax coating dissipates (Surface Tech, 2023).

Figure 2.1.3: ACE XP™ Fibers (Surface Tech, 2023)

Similar to GTR additives, PCR plastic additives are incorporated into asphalt mixtures via wet or dry processes. The most commonly utilized PCR plastic additives include linear-low density polyethylene (LLDPE), low-density polyethylene (LDPE), and high-density polyethylene (HDPE) (Foshee, 2022). Both plastic modified mixtures featured in the AG study included a form of recycled polyethylene (rPE). The wet-process mixture included additional polymer components (*Table 3.2.1*). As previously shown by Foshee, 2022, *Figure 2.1.4* and *Figure 2.1.5* provide examples of wet and dry-process PCR plastic additives, respectively.

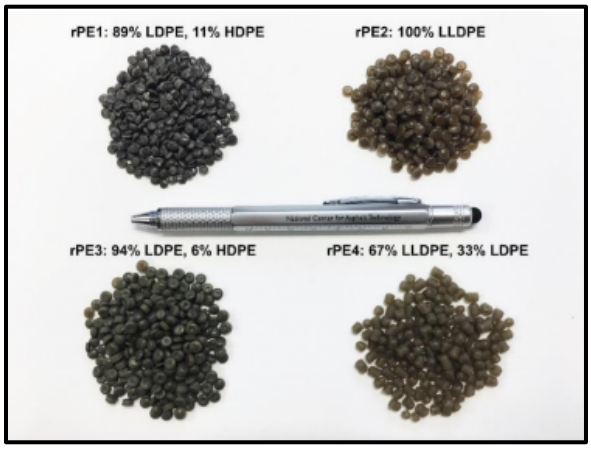

Figure 2.1.4: Typical Wet-Process rPE Additives ("Research Needed on Using Recycled Plastics in Asphalt", 2021)

Figure 2.1.5: Typical Dry-Process rPE Additives (Yin, 2022)

2.2: Complex Dynamic Modulus (E) Test*

Complex dynamic modulus (E*), often referred to as just "dynamic modulus" is measured by performing AASHTO TP 132-19 (Standard Method of Test for Determining the Dynamic Modulus for Asphalt Mixtures Using Small Specimens in the Asphalt Mixture Performance Tester (AMPT)). This test evaluates the modulus and phase angle of asphalt mixtures at different testing temperatures and loading frequencies. Small cylindrical performance test specimens are subjected to repeated controlled haversine compressive loadings. The E* of an asphalt mixture is calculated by dividing the absolute value of the peak-to-peak applied compressive load by the resulting peak-to-peak axial strain (as measured by three linear variable differential transformers (LVDTs) spaced 120° apart). The phase angle of an asphalt mixture is the time-lag between the on-specimen compressive stress and resulting on-specimen axial strain. Phase angle is expressed in units of degrees. *Figure 2.2.1* provides a schematic detailing the measured parameters used in the determination of E*. Dynamic modulus is one of the primary material properties used to characterize an asphalt mixture and is commonly used as a design input into mechanistic-empirical design for pavement structural modeling and performance simulations. E* is also used to determine the initial strain amplitude of the Direct Tension Cyclic Fatigue Test (AASHTO TP 133-22).

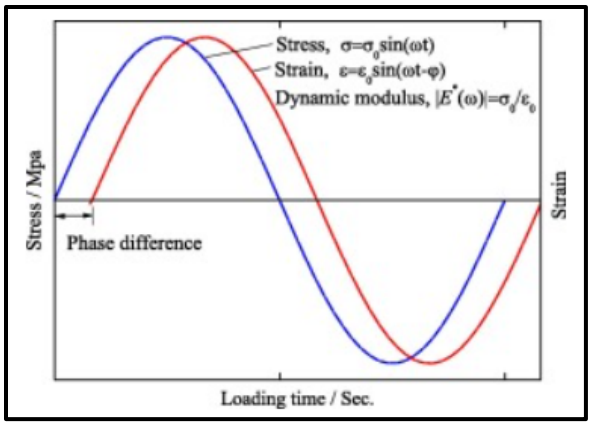

Figure 2.2.1: Sinusoidal Applied Stress, Measured Strain and Time Lag (Zhang and Bao, 2022)

From the results of AASHTO TP 132-19, an E* master curve can be established for a particular asphalt mixture by following the procedures detailed by AASHTO R 84-17 (Standard Practice for Developing Dynamic Modulus Master Curves for Asphalt Mixtures Using the Asphalt Mixture Performance Tester (AMPT)). An asphalt mixture's master curve displays its E* over a wider range of testing frequencies than was actually performed. This is achieved through the use of the time-temperature superposition concept for viscoelastic materials. Whereby the modulus of a viscoelastic material at a high temperature and short loading period is equal to that at a low temperature and long loading period. Thus, the effects of temperature on material modulus can be estimated through the use of a frequency shift factor. The E* master curve is constructed at a single reference temperature (in this case 20°C). A frequency shift factor is applied to the E* values from tests conducted at alternate temperatures (4 and 40°C) to equate them to the reference temperature. The master curve is plotted on a log-log scale, with the log value of the E* on the y-axis, and the log value of the reduced frequency on the x-axis. *Figure 2.2.2* displays a schematic detailing E* master curve construction using horizontal shift factors.

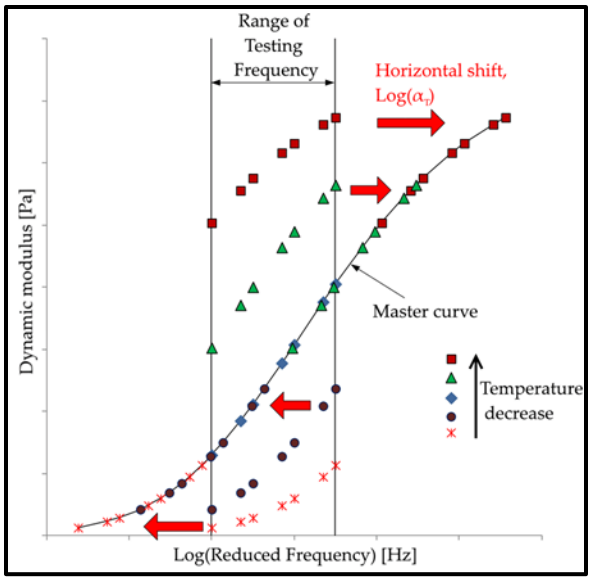

Figure 2.2.2: E Master Curve Schematic with Shift Factors (Hasheminejad et al., 2019)*

Xie and Shen (2016) evaluated the dynamic modulus (E*) of rubber-modified stone matrix asphalt (SMA) mixtures. Dry-process, wet-process, and terminally blended CRM mixtures were compared to an SBS-modified mixture and an unmodified control mixture. In total, the E* of five SMA mixtures was evaluated. E* was measured at temperatures of 4°C, 20°C, and 45°C, and frequencies of 0.1 Hz, 1, Hz, and 10 Hz in accordance with AASHTO 13 TP79-12. *Figure 2.2.3* displays the measured E* values at each testing temperature and frequency. It was observed that rubber modification, regardless of the process (wet, dry, or terminally blended), increased the dynamic modulus of the SMA mixtures at 45°C, but no significant differences in E* were observed at 4°C or 20°C. Additionally, it was observed that the terminally blended rubber-modified SMA mixture exhibited a greater E* at 45°C in comparison to the wet and dry-process rubber-modified SMA mixtures. The terminally blended rubber-modified SMA mixture displayed a similar high temperature dynamic modulus to the SBS-modified SMA mixture.

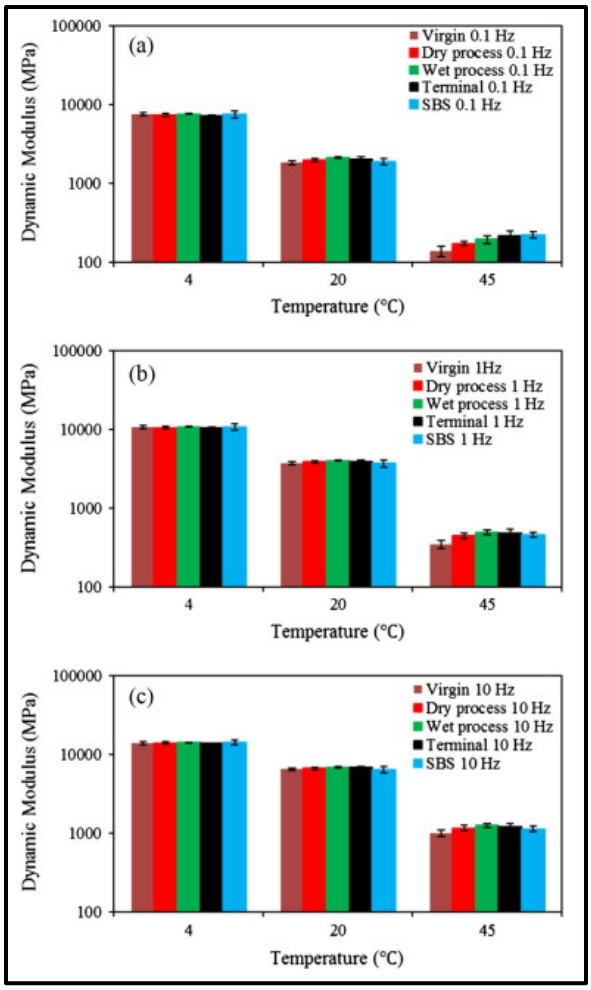

Figure 2.2.3: E Versus Temperature (Xie and Shen, 2016)*

Jin et al. (2023) evaluated the E* of two dry-processed rubber-modified mixtures relative to an unmodified control mixture. Both 12.5 and 19.0mm nominal maximum aggregate size (NMAS) dense-graded mixture designs were tested. In both mixture designs, the CRM dosage rate was approximately 10% by weight of asphalt binder. The E* master curve (constructed at a reference temperature of 21°C) for all four mixtures is shown in *Figure 2.2.4*. It was observed that the dry-process rubber-modified mixtures displayed a greater E* across most of the reduced frequency range relative to the unmodified mixtures of the same NMAS.

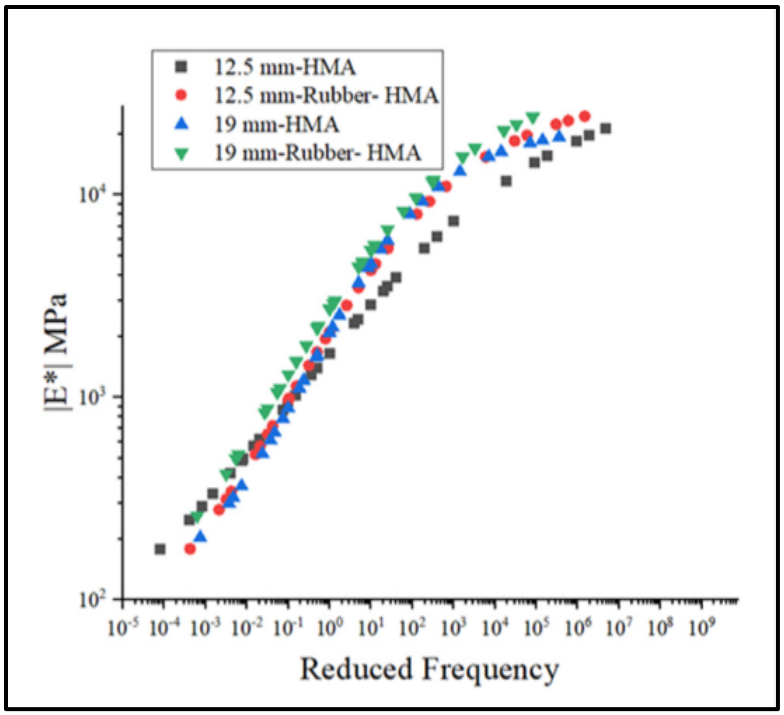

Figure 2.2.4: E Master Curves (Jin et al., 2023)*

Kaloush et al. (2010) provided advanced material characterization of an asphalt mixture modified with synthetic fibers and an unmodified control mixture. Two full scale test sections (unmodified control and fiber-modified) were constructed as part of a larger pavement rehabilitation effort in coordination with the City of Tempe, Arizona. The asphalt concrete was composed of a typical dense graded mixture (PHX C-3/4) and PG 70-10 base asphalt binder. A blend of polypropylene and aramid fibers was added at the batch plant at a dosage rate of approximately 1 lbs per 1 ton of asphalt mixture. Beam and cylindrical specimens were prepared from the asphalt mixtures sampled from the paving locations. This sampled asphalt mixture was compacted in the laboratory. E* was determined for the unmodified control and fiber-modified asphalt mixtures via AASHTO TP 62-03. Testing temperatures of 14, 40, 70, 100, and 130°F and loading frequencies of 25, 10, 5, 1, 0.5, and 0.1 Hz were used. An E* master curve was constructed for both mixtures at a reference temperature of 70ºF (*Figure 2.2.5*). From the E* master curve it was determined that the fiber-modified mixture had greater E* at all loading frequencies in comparison to the unmodified control mixture. An additional comparison of E* at the 10 Hz loading frequency is shown by *Figure 2.2.6*.

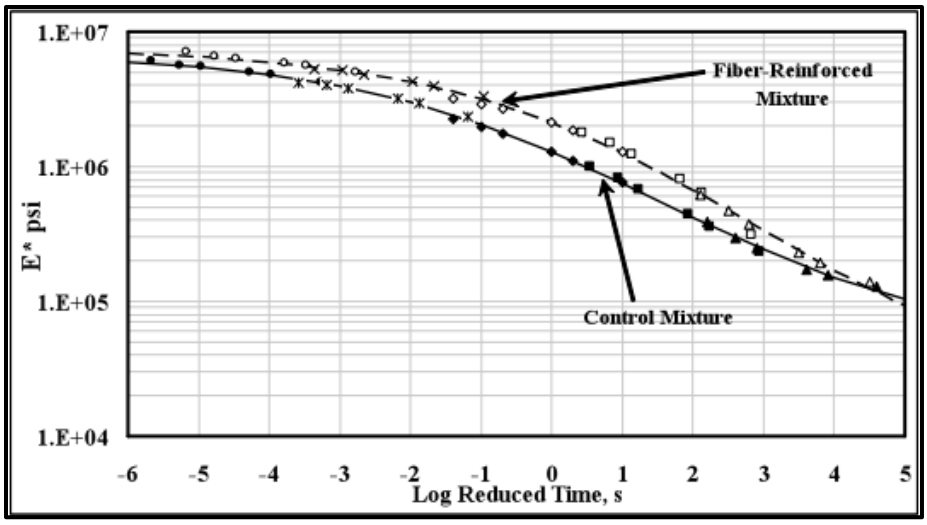

Figure 2.2.5: E Master Curves (Kaloush et al., 2010)*

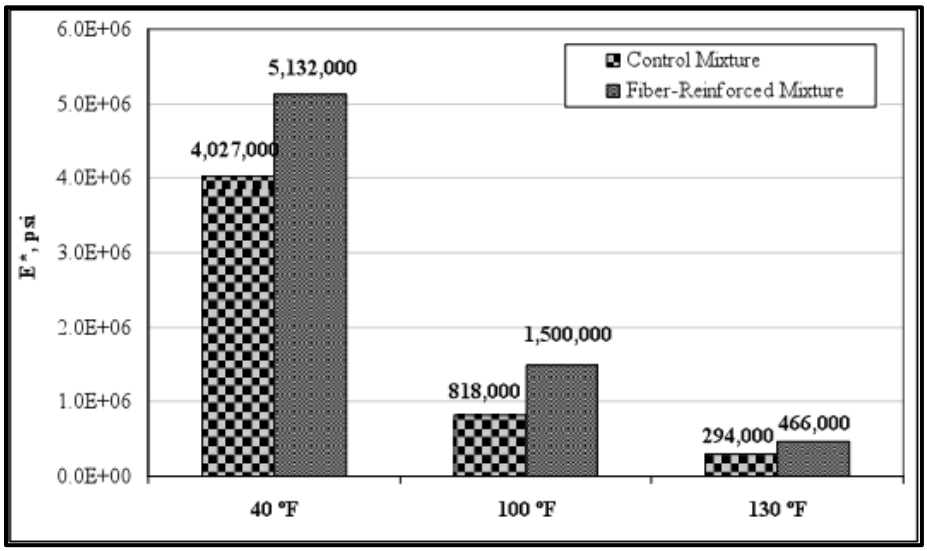

Figure 2.2.6: Comparison of E at 10 Hz (Kaloush et al., 2010)*

Mateos and Harvey (2019) evaluated the mechanical properties of a fiber reinforced asphalt concrete (FRAC). This study evaluated the same ACE XP^{TM} product used for AG fiber-modified test section (N5 (Aramid)). The asphalt mixture evaluated in this study was a typical dense-graded Superpave mixture with a 19mm NMAS. It included 15% RAP and a PG 64-22 base asphalt binder. An unmodified control mixture was compared against the fiber-modified mixture. The latter received a dosage rate of 0.013% (by total weight of mix) of aramid fibers. E* was determined for both the control and ACE XP^{TM} fiber-modified asphalt mixtures. E* was evaluated at temperatures of 4, 20, and 40°C and loading frequencies of 25, 10, 5, 1, 0.5, and 0.1 Hz. *Figure 2.2.7* shows the E* master curve that was constructed for both mixtures at a reference temperature of 20ºC. The

addition of the ACE XP™ fiber provided an increase in E* at the high testing temperature. However, the ACE XP™ fiber-modification had no effect on E* at the intermediate and low testing temperatures.

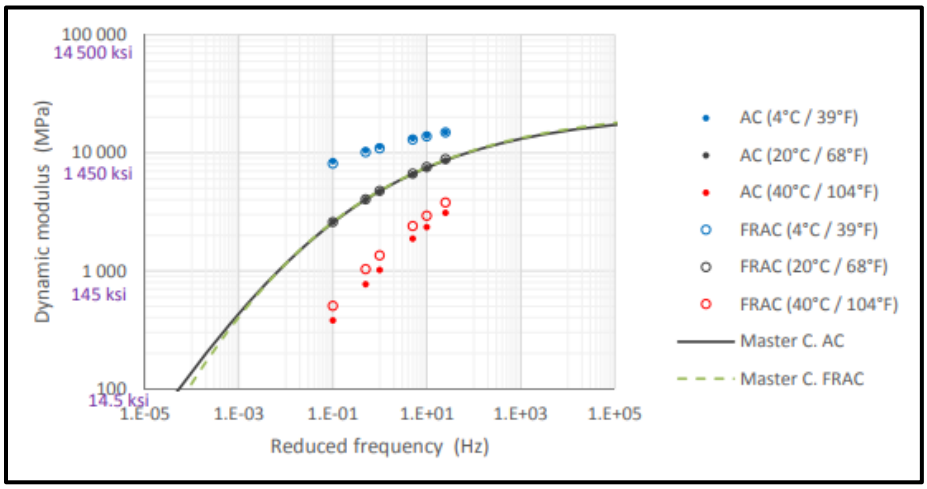

Figure 2.2.7: E Master Curves (Mateos and Harvey, 2019)*

Ibrahim et al. (2022) evaluated the effects of recycled polyethylene (rPE) modification of asphalt mixtures on E*. Both wet-process and dry-process rPE-modified mixtures were evaluated versus an unmodified control mixture. Each of the mixtures utilized a 12.5mm NMAS Superpave HMA design, PG 64-22 base asphalt binder, and 15% reclaimed asphalt pavement (RAP). For the wet-process produced mixture, 2.5% rPE was added to the virgin asphalt binder. For the dry-process produced mixture, 10% rPE was added to the aggregate and RAP (before the introduction of the asphalt binder). E* was evaluated at testing temperatures of 4.4, 21.1, 37.8, and 54.4ºC and loading frequencies of 25, 10, 5, 1, 0.5, and 0.1 Hz. *Figure 2.2.8* displays the E* master curve for each of the asphalt mixtures, and was constructed at a reference temperature of 21.1ºC. Both asphalt mixtures containing rPE had increased E* relative to the unmodified control mixture. Of the two rPE mixtures, the dry-process mixture displayed the highest E*.

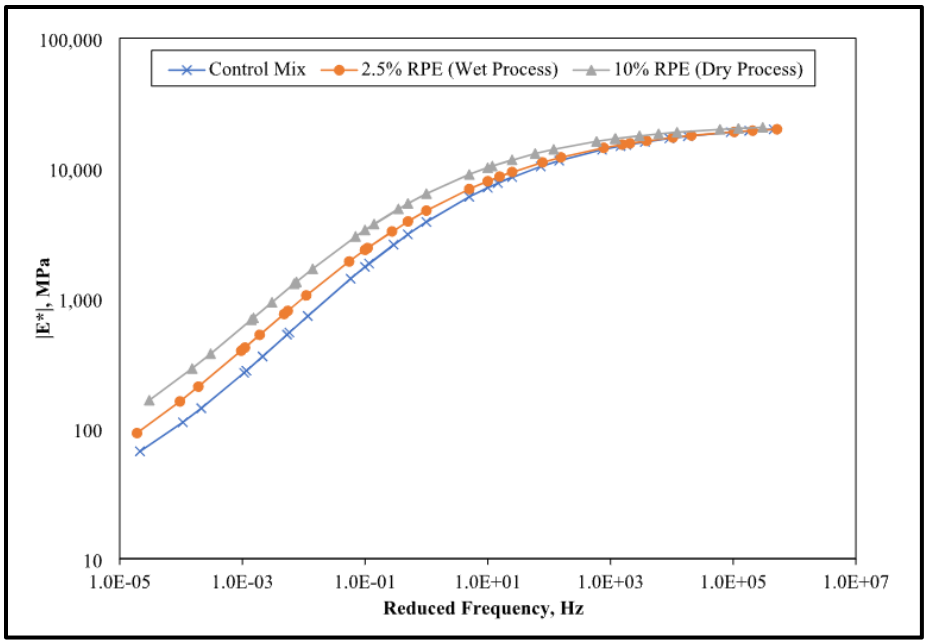

Figure 2.2.8: E Master Curves (Ibrahim et al., 2022)*

The previous research studies detailed in this section have indicated that dynamic modulus (E*) is subject to significant effects depending on the additive technology. Xie and Shen (2016) observed that rubber modification, regardless of the process (wet, dry, or terminally blended), increased the high temperature E*of SMA mixtures. Jin et al. (2023) concluded that dry-process rubber-modification increased the E* of dense-graded mixtures across most of the reduced frequency range. One study found that a blend of polypropylene and aramid fibers added via the dry-process increased asphalt mixture E* across the entire reduced frequency range (Kaloush et al., 2010), whilst another observed little to no change in E* except at the highest testing temperature (Mateos and Harvey, 2019). Ibrahim et al. (2022) evaluated the effects of both wet and dry-process rPE modification of asphalt mixes on E*. It was found that rPE modification, regardless of process, increased E*. However, the dry-process technology provided a greater increase in E* relative to the wet-process, though this could have been due to the increased dosage rate of rPE.

2.3: Direct Tension Cyclic Fatigue Test

The direct tension cyclic fatigue test evaluates the fatigue resistance of asphalt mixtures using the S-VECD (simplified viscoelastic continuum damage) model. The S-VECD model allows for a prediction of fatigue life at any temperature or loading condition by characterizing the fundamental material properties (discussed below) of the asphalt mixture. This test is performed in accordance with AASHTO TP 133-22 (Standard Method of Test for Determining the Damage Characteristic Curve and Failure Criterion Using Small Specimens in the Asphalt Mixture Performance Tester (AMPT) Cyclic Fatigue Test). Under AASHTO TP 133-22, test specimens are subjected to strain-controlled cyclic axial loadings until reaching their failure point, defined as being the cycle at

which the peak-to-peak stress times cycles curve reaches a maximum value. The test output includes the specimen's pseudo secant modulus (C) versus damage (S) curve, also known as its "damage characteristic curve", and its pseudo energy-based fatigue failure criterion (D^R). These parameters, in conjunction with E* data, are direct inputs into the mechanistic-empirical pavement design software FlexPAVE™ for asphalt mixture characterization. Both the damage characteristic curve and D^R are fundamental material properties. This means that they are independent of temperature, frequency, and loading mode effects. The damage characteristic curve defines the material integrity (pseudo stiffness) at a given state of internal damage (S). The level of material integrity at failure may also provide insight into the damage evolution within a mixture. That is, if a mixture reaches its failure point whilst retaining a higher pseudo stiffness than another, it may indicate that that mixture has worse fatigue performance. However, the relative positioning of damage characteristic curves themselves cannot be used to make definitive conclusions about the fatigue performance of asphalt mixtures. This is because fatigue performance is influenced by a multitude of factors, including both the stiffness of a mixture (which the C versus S curve is heavily influenced by) as well as a mixture's damage tolerance. In order to rank mixtures on the basis of fatigue performance the cyclic fatigue index parameter (S_{app}) must be calculated. The S_{app} for a given mixture is calculated using the damage characteristic curve, E* data (obtained from performing AASHTO TP 132-19 prior to this test), and D^R. The D^R failure criterion defines mixture toughness and is derived from the plot of the linear relationship between the sum of 1-C and the number of cycles to failure (N_f) for a mixture. The slope of this linear relationship is the D^R failure criterion. A steeper slope corresponds to a higher value of D^R, and an increase in material toughness. All calculations necessary deriving damage characteristic curves, D^R, and Sapp are provided by AASHTO TP 133-22 and can be automatically performed using FlexMAT™ Cracking v2.0 or newer in conjunction with the IPC Global© test control software. *Figure 2.3.1* provides a schematic detailing the S-VECD model approach. Included are the damage characteristic and D^R failure criterion models used to calculate the S_{app} parameter. Additionally, these models can be used to predict fatigue life (number of cycles to failure (N_f)) for an asphalt mixture.

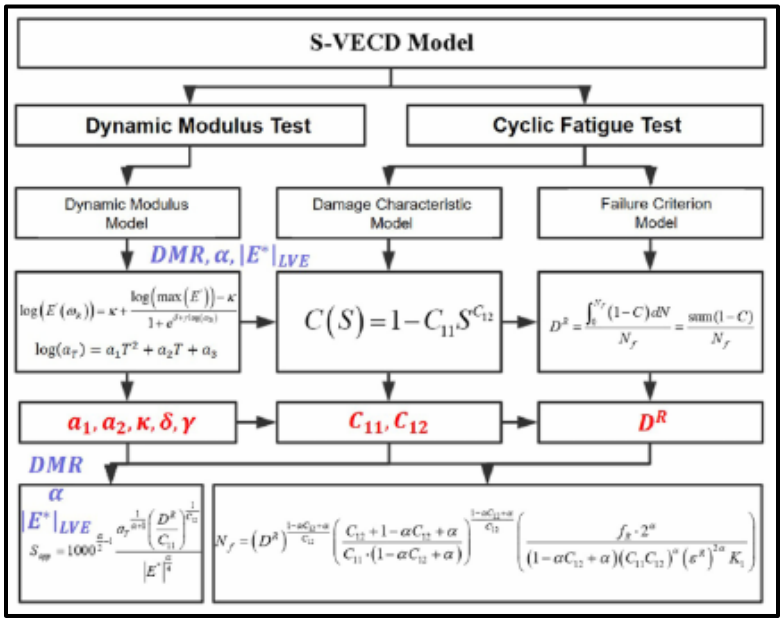

Figure 2.3.1: S-VECD Model Schematic (Ding et al., 2020)

Zeida et al. (2014) evaluated the fatigue performance of wet-process rubber-modified and polymer-modified gap-graded asphalt mixtures using direct tension cyclic fatigue testing. In addition to the two modified mixtures, an unmodified control mixture was also tested. The additive dosage rate used was 6% for the polymer-modified mixture and 20% for the rubber-modified mixture. The same 70/100 penetration grade base binder was used for each mixture design. An identical binder content of 5.6% was used for both the un-modified control and the polymer-modified mixtures. However, the rubber-modified mixture used a binder content of 8.7%. Two test specimens were prepared and tested for each mixture. Pseudo stiffness (C) versus damage (S) curves were constructed for each test sample, and a final damage characteristic curve was fitted for each mixture. *Figure 2.3.2* shows the damage characteristic curves for each of the gap-graded mixtures. The unmodified and polymer-modified mixtures display the more favorable curves in comparison to the rubber-modified mixture. Mixture fatigue life in constant stress and strain applications was predicted using formulas that had previously been derived and validated within other laboratory experiments. This fatigue life prediction method preceded the development of the S_{app} parameter, but offered a better indication of relative fatigue life than could have been inferred from the C versus S plot alone. *Figure 2.3.3* displays the fatigue life predictions for each mixture in a strain-controlled simulation at 5, 20, and 27°C, respectively. The rubber-modified mixture was predicted to have the best fatigue performance despite initially having the least favorably positioned damage characteristic curve. The polymer-modified mixture followed next, with the unmodified control exhibiting the worst predicted fatigue performance.

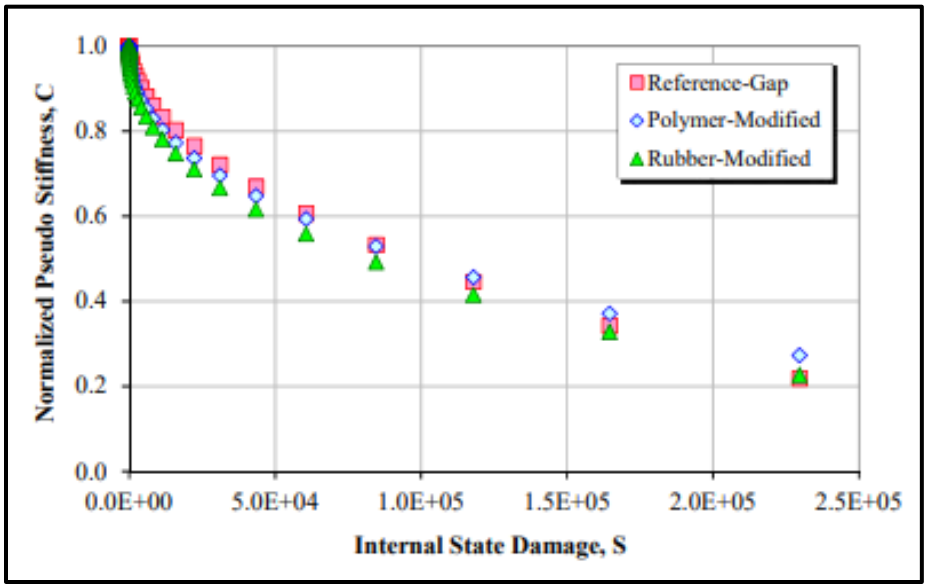

Figure 2.3.2: Damage Characteristic Curves (Zeida et al., 2014)

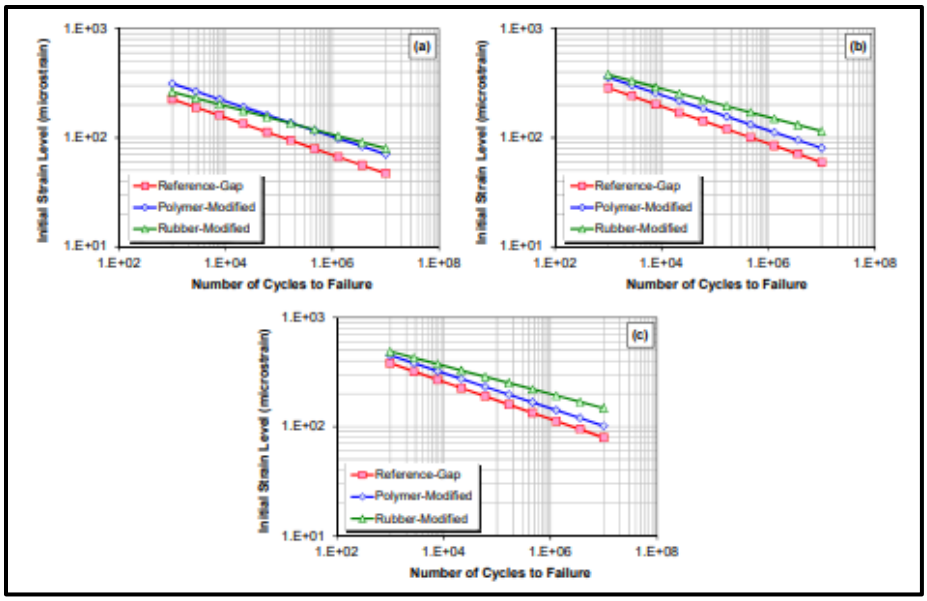

Figure 2.3.3: Fatigue Life Predictions (Zeida et al., 2014)

Noorvand et al. (2018) investigated the fatigue performance of two different aramid-modified asphalt mixtures versus an unmodified control mixture via direct tension cyclic fatigue testing. The mixtures each followed an identical dense-graded 12.5mm Marshall mixture design with asphalt binder content of 5.2%. The same PG 70-10 asphalt binder was used for each mixture. Both mixtures containing aramid fibers were modified via the dry-process, with a dosage rate of 65.5 g per ton of mixture. One mixture contained "good" fiber distribution (FA), whilst the other contained "poor" fiber distribution (FB). *Figure 2.3.4* displays the damage characteristic curves for the control mixture, as well as the FA and FB fiber-modified mixtures. It was concluded that the fiber-modified mixtures had damage characteristic curves with minimal differences to the unmodified control mixture, though the material integrity (C) at the same level of damage (S) was slightly lower than that of the control mixture. A strain-based fatigue life simulation was also conducted. *Figure 2.3.5* displays the results of this simulation, with both fiber-modified mixtures displaying an increase in fatigue lifer versus the unmodified control mixture.

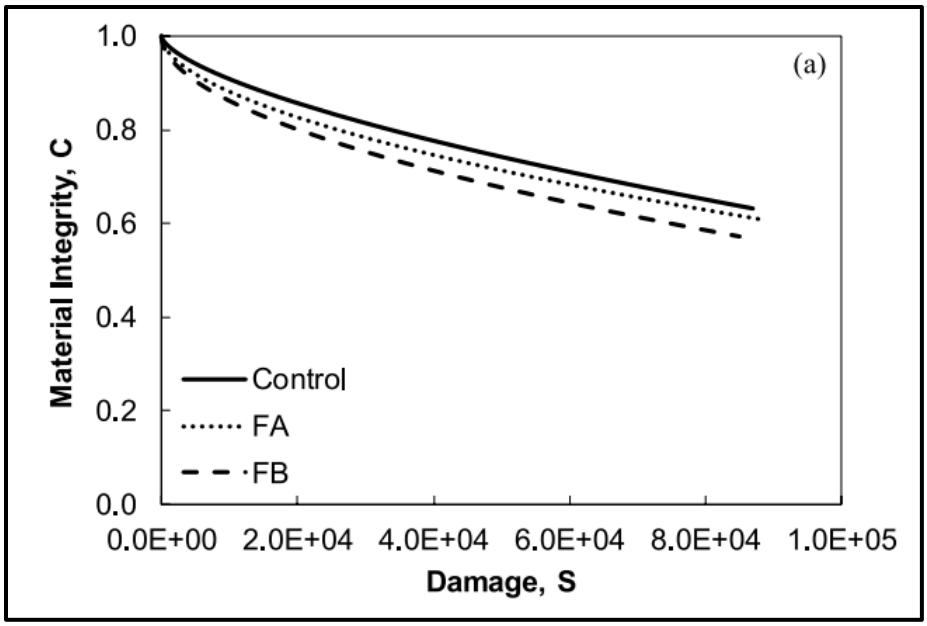

Figure 2.3.4: Damage Characteristic Curves (Noorvand et al., 2018)

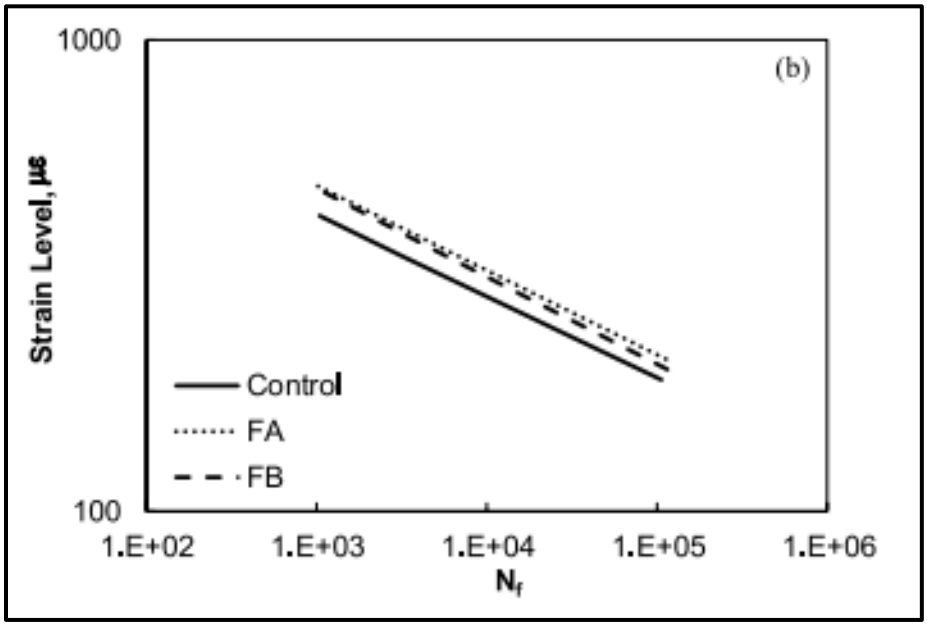

Figure 2.3.5: Fatigue Life Simulations (Noorvand et al. 2018)

Queiroz et al. (2023) investigated the fatigue performance of two different polymer-modified asphalt mixtures versus an unmodified control mixture using direct tension cyclic fatigue testing. The first mixture was modified with SBS (referred to as 55/75-E), while the second was modified with a combination of Ethylene Methyl Acrylate and Glycidyl Methacrylate (EMA-GMA), High Density Polyethylene (HDPE), and Polyphosphoric Acid (PPA116%) (referred to as "modified

binder"). Both mixtures containing polymers were modified via the wet process. The 55/75-E asphalt binder was purchased directly from the supplier with the SBS polymer already incorporated. The wet-process "modified binder" was prepared in the laboratory with the same 50-70 penetration grade base binder used for the control mixture. The final polymer dosage rates used were 1.26% EMA-GMA, 0.21% HDPE, and 0.15% PPA116% by weight of asphalt binder. *Figure 2.3.6* displays the damage characteristic curves that were constructed for the polymer-modified mixtures and the unmodified control mixture. The "modified mixture", consisting of a composite of three types of polymers, displayed the highest pseudo stiffness, or material integrity, for any given level of damage. However, the "modified mixture" failed at the highest level of material integrity, suggesting that it had less damage accumulation tolerance than both the unmodified control and the SBS-modified mixture. *Figure 2.3.7* displays the plots of D^R for each mixture. The modified mixture displayed the highest value for D^R, followed by the SBS-modified mixture, and the unmodified control mixture. The S_{app} parameter was computed for each mixture. Both polymer-modified mixtures had a S_{app} parameter of 6, while the unmodified control mixture had a 4. This result indicates that both polymer-modified mixtures had similar fatigue performance that was improved over the unmodified control mixture.

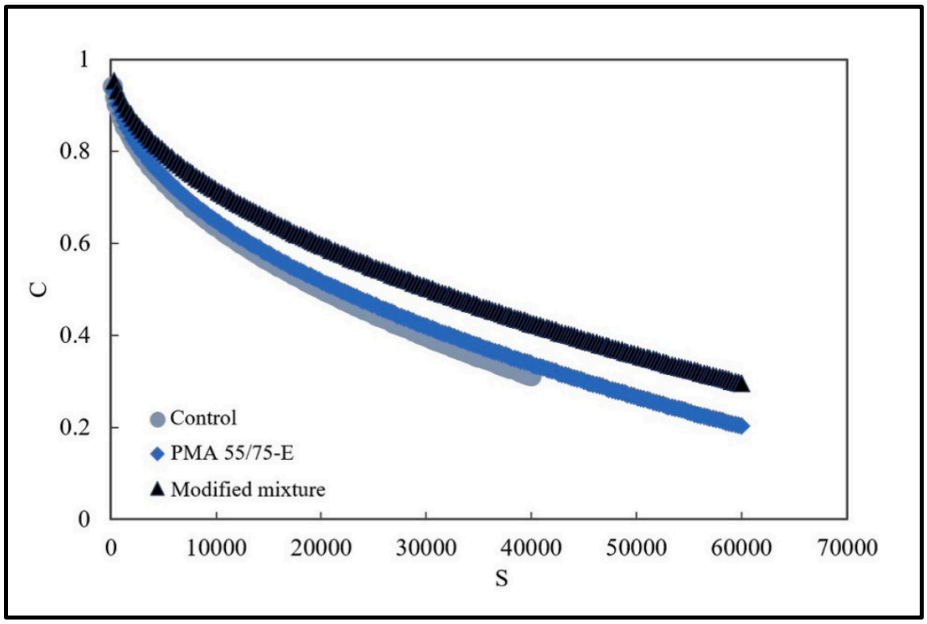

Figure 2.3.6: Damage Characteristic Curves (Queiroz et al., 2023)

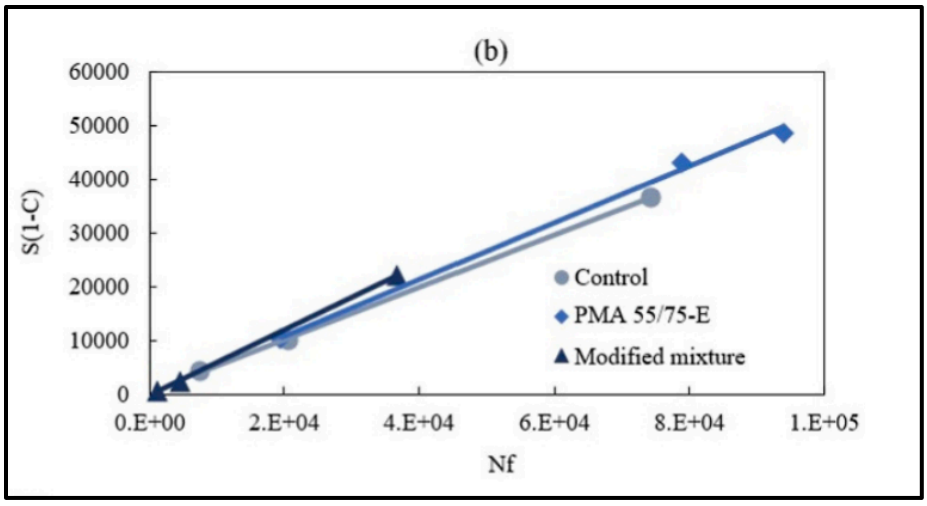

Figure 2.3.7: D^R Failure Criterion (Queiroz et al., 2023)

Spadoni et al. (2022) evaluated the fatigue performance of asphalt mixtures modified with plastic via the dry process using direct tension cyclic fatigue testing. One dry-process modified mixture contained recycled plastic and graphene, and the other contained plastomeric polymers (referred to as mixtures GC and PC, respectively). Another mixture containing an SBS-polymer modified asphalt binder was used for comparison (referred to two as mixture H). Direct tension cyclic fatigue and E* testing were conducted in accordance with AASHTO TP 133 and AASHTO TP 132, respectively. For the cyclic fatigue testing, a loading frequency of 10 Hz and a testing temperature of 21ºC. An initial strain magnitude between 190 and 290 με was used to achieve a number of cycles to failure within the range of 2,000 to 80,000 as required by AASHTO TP 133. For each test mixture, damage characteristic curves were constructed, the pseudo energy-based fatigue failure criterion (D^R) was determined, and the cyclic fatigue index parameter (S_{app}) was calculated. *Figure 2.3.8* displays the fitted damage characteristic curves for the dry-process plastic modified mixtures (GC and PC) with respect to the wet-process SBS-polymer modified mixture (H). The damage characteristic curves for all mixtures were relatively similar, however, the mixture PC and H reached a lower pseudo-stiffness value, potentially indicating that those mixtures had more capacity to withstand fatigue damage. *Figure 2.3.9* displays the D^R failure criterion for the three mixtures of interest. Mixture H (SBS-polymer modified reference) displayed the highest D^R value. This finding indicated that the reference mixture had increased capacity to absorb and store energy before fatigue failure (increased toughness) in comparison to both dry-process plastic modified mixtures. Finally, the S_{app} parameter was calculated for each mixture. This value indicates the relative fatigue resistance of each mixture, factoring in a mixture's stiffness, damage tolerance, and toughness. *Figure 2.3.10* displays the S_{app} parameter for each mixture. The reference mixture (H) displayed the greatest fatigue resistance.

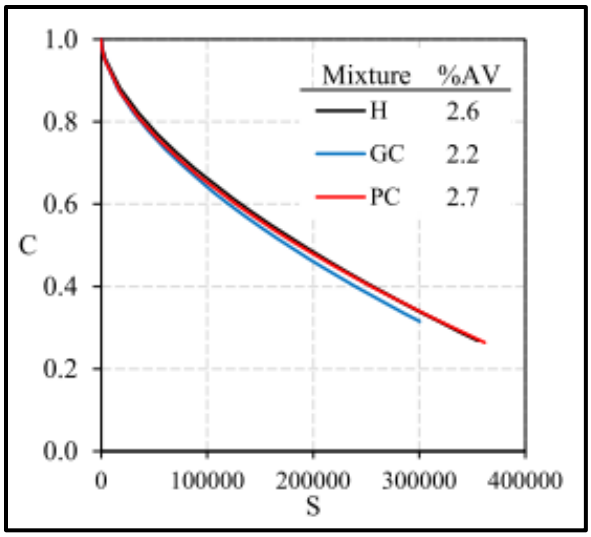

Figure 2.3.8: Fit of Damage Characteristic Curves (Spadoni et al., 2022)

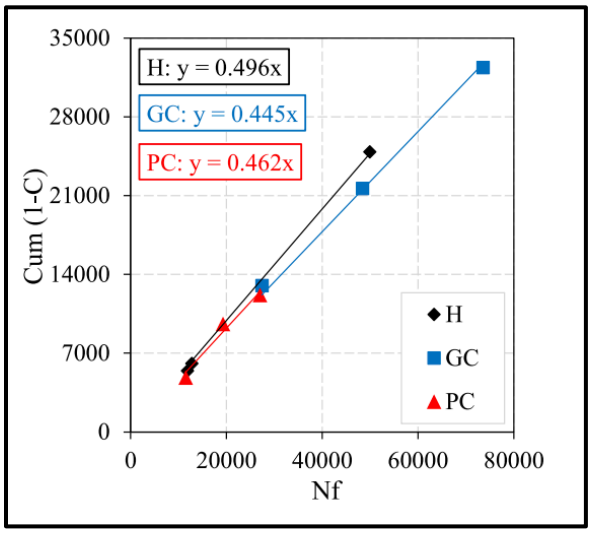

Figure 2.3.9: D^R Failure Criterions (Spadoni et al., 2022)

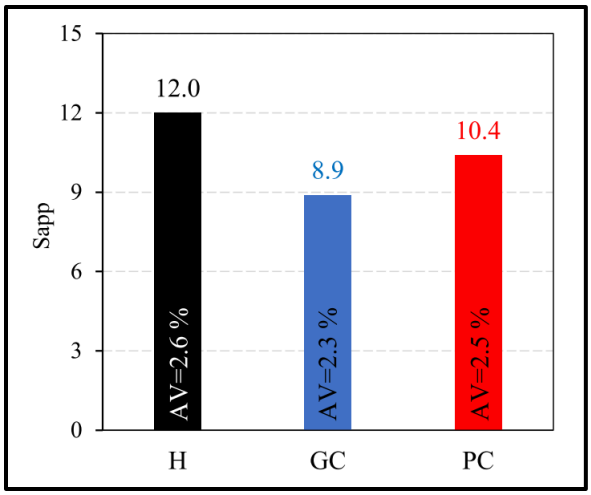

Figure 2.3.10: S_{app} Parameters (Spadoni et al., 2022)

The previous research studies detailed in this section indicated that damage characteristic curves, D^R failure criterion, and S_{app} parameters are all subject to influences with the introduction of additives. Wet-process rubber modification was found to decrease pseudo stiffness at any given state of internal damage but yielded a more favorable curve termination point. This ultimately led to an increase in simulated mixture fatigue life relative to an unmodified control mixture and a wet-process polymer-modified mixture (Zeida et al., 2014). Noorvand et al. (2018) investigated the fatigue performance of two different aramid-modified asphalt mixtures ("good" and "poor" fiber distribution) versus an unmodified control mixture. It was concluded that the damage characteristic curves of the fiber-modified mixtures were slightly lower than, though minimally different to, the unmodified control mixture. However, both fiber-modified mixtures displayed an increase in simulated fatigue life. A wet-process mixture, modified with a combination of EMA-GMA, HDPE, and Polyphosphoric Acid was found to provide an increase in pseudo stiffness at any given state of internal damage relative to an unmodified control and an SBS polymer-modified mixture. The "modified mixture" also displayed the highest D^R, followed by the SBS polymer-modified mixture. Both the "modified mixture and the SBS polymer-modified mixture displayed an identical S_{app} parameter of 6. This indicated that both modified mixtures had an improvement in fatigue performance over the unmodified control mixture (S_{app} parameter of 4) (Queiroz et al., 2023). Spadoni et al., 2022 evaluated the fatigue performance of two asphalt mixtures modified with plastics via the dry process. One modified mixture contained recycled plastic and graphene, and the other contained plastomeric polymers (referred to as mixtures GC and PC, respectively). Additionally, an SBS polymer-modified mixture (H) was included as a reference. The damage characteristic curves of the PC and H mixtures were nearly identical, with both showing an improvement over the GC mixture. The D^R and S_{app} parameter of the SBS polymer-modified mixture was the highest, followed by the PC and GC mixtures. This finding indicated that the wet-process SBS polymer-modified mixture provided greater fatigue resistance than either of the dry-process plastic modified mixtures.

2.4: Bending Beam Fatigue Test

The bending beam fatigue test (BBFT) evaluates the fatigue life of asphalt mixtures by subjecting beam samples to repeated flexural loadings in sinusoidal application pattern. The BBFT is performed in accordance with AASHTO T321-22 (Standard Method of Test for Determining the Fatigue Life of Compacted Asphalt Mixtures Subjected to Repeated Flexural Bending). During the test, on- specimen strain is measured using an LVDT block and is referenced from the neutral axis of the specimen. *Figure 2.4.1* displays a schematic of the four-point bending (4PB) beam fatigue setup. Though a controlled stress mode beam fatigue test is possible, AASHTO T 321-22 evaluates the fatigue life of beam samples in a controlled strain mode. For a given asphalt mixture, the number of cycles to failure is recorded at multiple strain levels (typically low, medium, high levels with at least three test replicates performed at each). Transfer functions can be created to numerically describe the relationship between strain level and the number of cycles to failure. *Equation 3.8.4* in the following chapter details the form of these functions. BBFT transfer functions themselves can be compared to evaluate the stain tolerance of asphalt mixtures or used for fatigue simulations within mechanistic-empirical design software. Additionally, the initial flexural stiffness of each beam sample is measured at the 50th loading cycle.

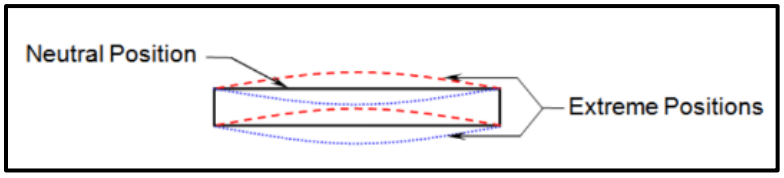

Figure 2.4.1: Neutral & Extreme Beam Position for Sinusoidal Loading (Mamlouk et al., 2012)

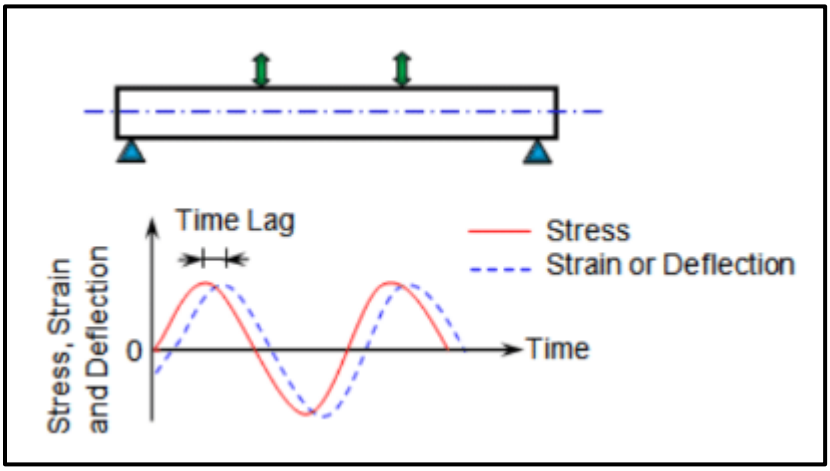

Figure 2.4.2: Beam Stress, Strain, & Deflection versus Time (Mamlouk et al., 2012)

Feiteira Dias et al. (2014) evaluated the fatigue life performance of crumb rubber-modified, gap-graded asphalt mixtures produced via the wet and dry-process relative to each other and a non-modified control mixture. Bending Beam Fatigue Testing (BBFT) samples were saw cut from slabs taken from the pavement test sections. The BBFT was performed at temperatures of 20 and 30°C. The tests were strain controlled (300, 500, and 700 με), with the failure criteria set at 50% of the initial flexural stiffness. *Figure 2.4.3* displays the fatigue transfer functions derived via a regression analysis of the BBFT results for each of the three asphalt mixtures. TB0 corresponds to the unmodified control mixture, TB3 to the dry-process rubber-modified mixture, and TA to the wet-process rubber-modified mixture. Both rubber-modified mixtures displayed improved fatigue life relative to the non-modified control mixture. The asphalt mixture modified via the wet-process was found to have better fatigue life in comparison to the modified via the dry-process.

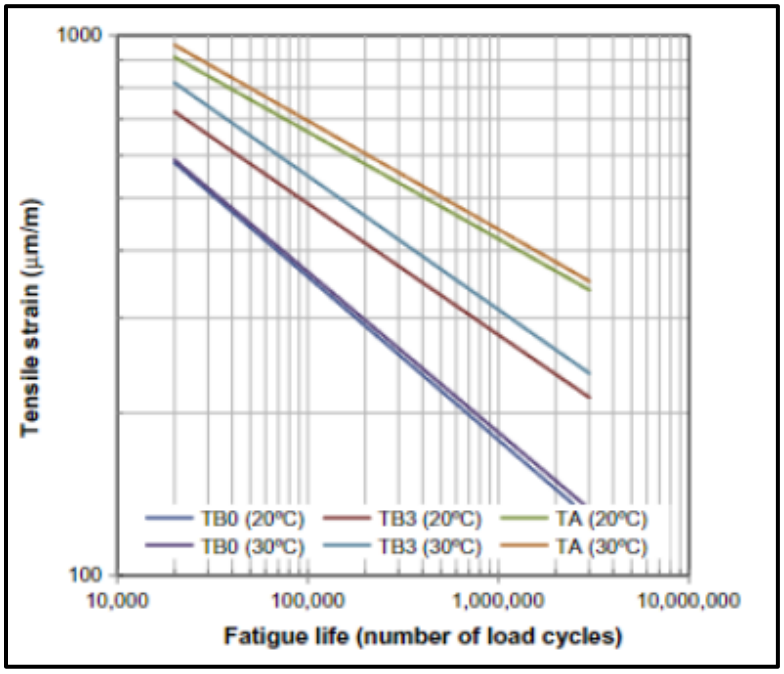

Figure 2.4.3: Fatigue Transfer Functions (Feiteira Dias et al., 2014)

Dantas et al. (2005) investigated the effects of crumb rubber modifier (CRM) on the mechanical properties of asphalt mixtures, including fatigue life. Four dense-graded mixtures using a 50-70 penetration graded asphalt binder were studied. These included an unmodified control, two dry-process produced CRM modified mixtures (with CRM dosage rates of 2% and 3.6%), and one mixture produced with wet-process CRM modified asphalt binder (21% by weight of asphalt binder). The fatigue life of the mixtures was evaluated via the bending beam fatigue test (BBFT) in accordance with the AASHTO TP8/96 recommendations. The specimens were long-term aged prior to testing, and a testing temperature of 20 ºC and loading frequency of 10 Hz was used. *Figure 2.4.4* shows the fatigue life relationships for each of the four mixtures tested. The dry-process mixture modified with 2.2% crumb rubber exhibited the best overall fatigue life, followed by the

dry-process mixture modified with 3.6% crumb rubber. Regardless of the method used to produce the mixtures (wet or dry), all CRM mixtures displayed increased strain tolerance relative to the unmodified control mixture.

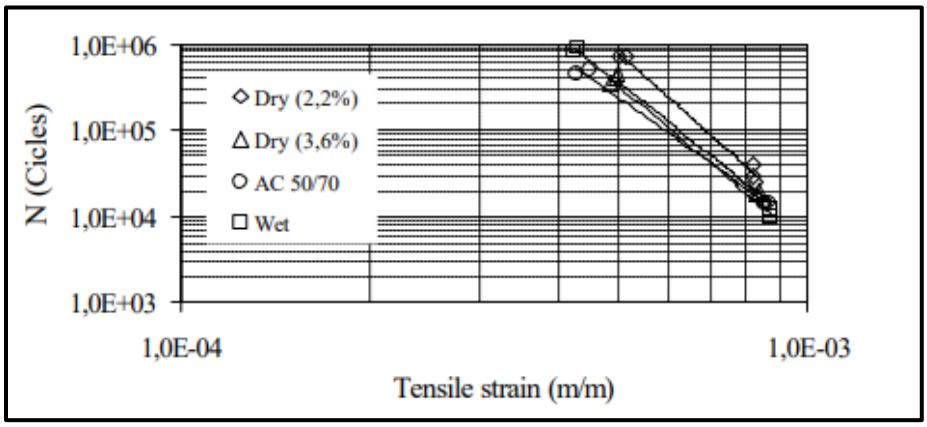

Figure 2.4.4: Fatigue Transfer Functions (Dantas et al., 2005)

Raad et al. (1993) investigated the fatigue life of a gap-graded asphalt-rubber hot mix (AHRM-GG) relative to a dense-graded conventional asphalt concrete (CAC-DG). The AHRM-GG was produced via the wet-process, with a CRM dosage rate of approximately 20% (by weight of asphalt binder). The fatigue life of both mixtures was evaluated using the bending beam fatigue test (BBFT). A testing temperature of approximately 70 ºF and loading frequency of 1 Hz were used, and the fatigue failure criteria was defined as being 50% of the initial flexural stiffness. *Figure 2.4.5* displays the fatigue transfer functions for both the AHRM-GG and the control CAC-DG. The AHRM-GG exhibited increased fatigue life across all strain levels relative to CAC-DG. However, it is important to note that these effects could have been due in part to a difference in gradation type between the control mixture and rubber-modified mixture (dense-graded vs gap-graded). *Figure 2.4.6* shows the tensile, compressive, and flexural stiffness versus applied loading repetitions. The AHRM-GG displayed a lower overall stiffness in comparison with the CAC-DG mixture. However, the reduction in stiffness (initial to final state) was higher for the CAC-DG mixture, indicating that the CAC-DG mixture experienced more fatigue damage in comparison to the AHRM-GG.

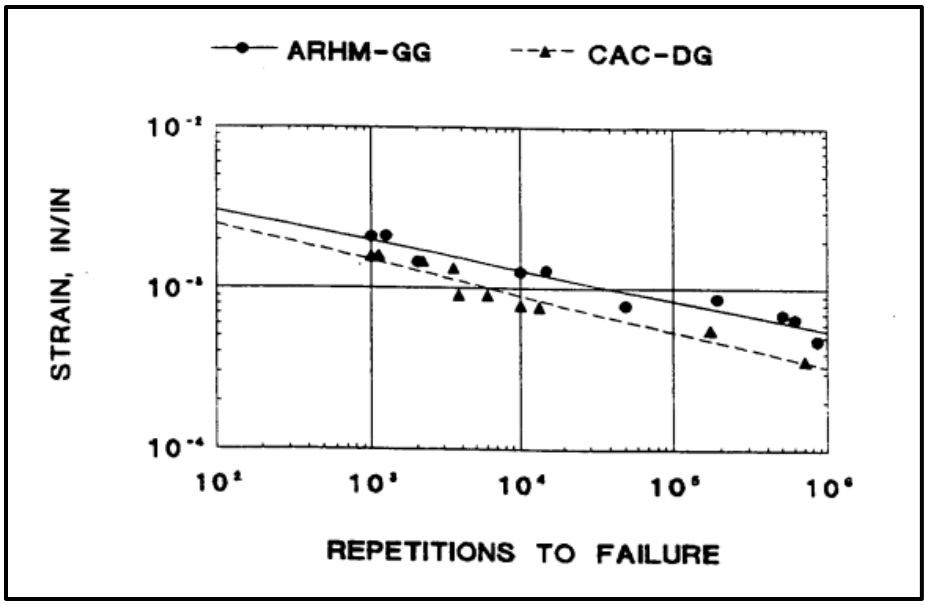

Figure 2.4.5: Fatigue Transfer Functions (Raad et al., 1993)

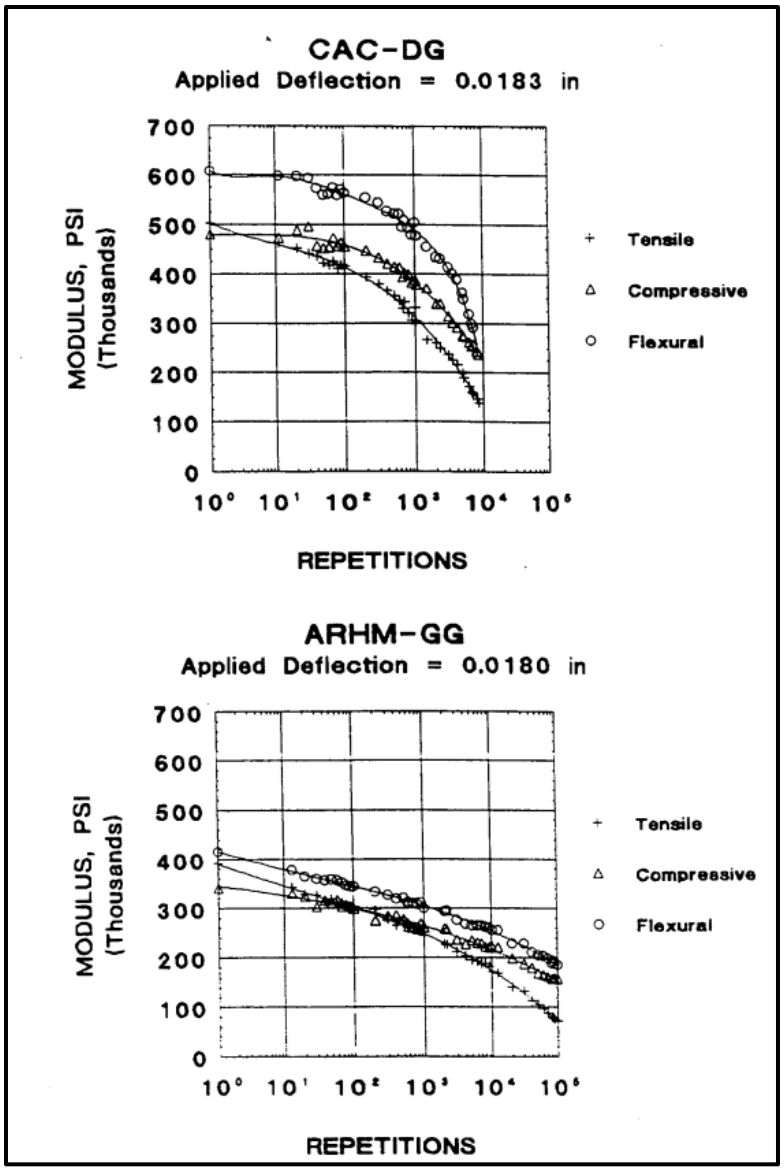

Figure 2.4.6: Stiffness Versus Loading Repetitions (Raad et al., 1993)

Kaloush et al. (2010) evaluated the fatigue cracking performance of the fiber-modified mixture using a three-point bending beam fatigue test (BBFT). Each test was strain controlled, with a single replicate performed at each strain and temperature combination (40, 70, 100ºF). The failure criteria was defined as 50% of the initial flexural stiffness (measured at the 50th loading cycle). *Figure 2.4.7* displays the controlled strain level versus the number of cycles to failure transfer functions for the unmodified control and fiber-modified mixtures at a testing temperature of 70ºF. The unmodified control mixture exhibited greater fatigue life at high strain values whilst the fiber-modified mixture exhibited greater fatigue life at low strain values.

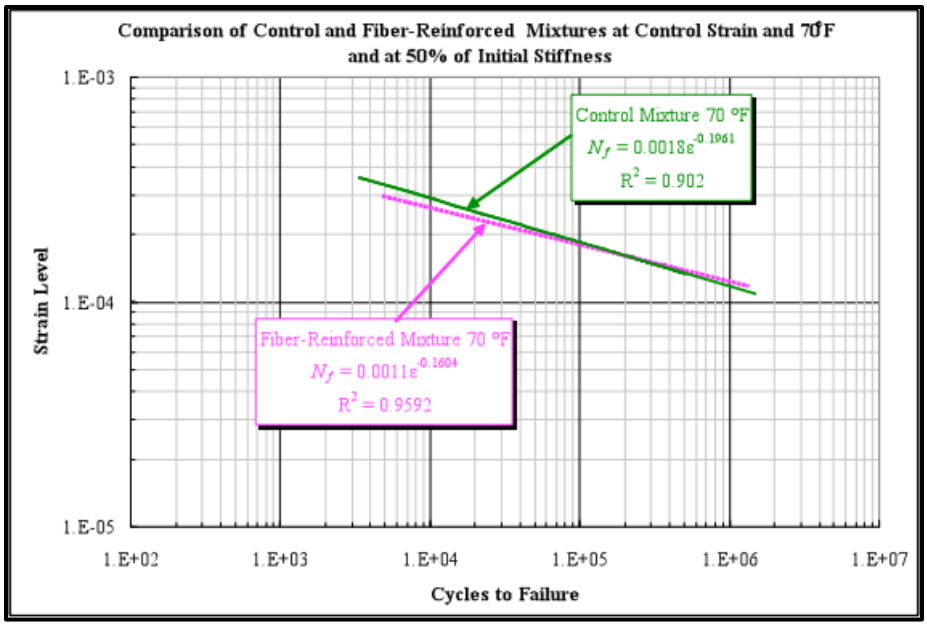

Figure 2.4.7: Fatigue Transfer Functions (Kaloush et al., 2010)

Mateos and Harvey (2019) evaluated the flexural fatigue resistance of the modified mixture through the use of a four-point bending beam fatigue test per the ASTM D8237-18 and AASHTO T 321-14 standards. Fatigue testing was conducted at a temperature of 20°C and 10 Hz. The asphalt beam samples were saw-cut from a roller-compacted slab. Initially, strain levels of 300 and 400 με were tested, however it was found that the addition of ACE XP™ fibers had little to no effect on the fatigue life at these lower strain values (*Figure 2.4.8*). When higher strain levels of 600 and 900 με were tested, the fiber-modified mixture showed an increase in its fatigue life of 90% and 200%, respectively.

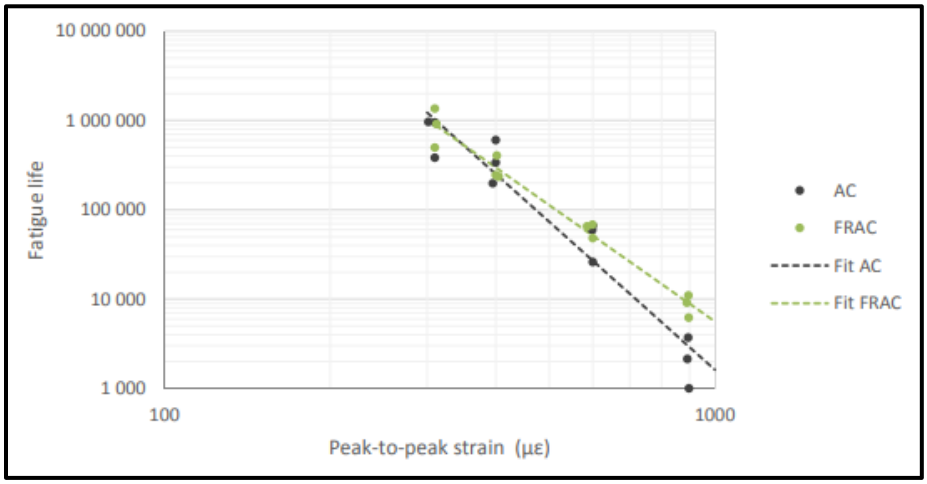

Figure 2.4.8: Fatigue Transfer Functions (Mateos and Harvey, 2019)

Zhang et al. (2020) evaluated the fatigue resistance of asphalt mixtures containing recycled polyethylene (PE) and recycled crumb rubber in the laboratory via the Bending Beam Fatigue Test (BBFT). The recycled polyethylene product was introduced via the dry-process in pellet form. The recycled crumb-rubber was added to the asphalt binder via the wet-process. Recycled PE dosage rates of 0.2% and 0.3% (by weight of asphalt mixture) were used. Recycled crumb rubber dosage rates of 12%, 18%, and 21% (by weight of asphalt binder) were used. For each mixture, a base asphalt binder with a penetration grade of 70 was used. An AC-20 dense graded asphalt mixture design was followed. The beam fatigue tests were strain-controlled (200 με), with the failure criteria set at 50% of the initial flexural stiffness, a loading frequency of 10 Hz, and a testing temperature of 20ºC. Four mixtures were selected for BBFT testing: an unmodified control (Base), a mixture modified with 0.3% recycled PE (PE0.3), a mixture modified with 21% recycled crumb rubber and 0.2% recycled PE (CR21PE0.2), and a mixture modified with 21% recycled crumb rubber and 0.3% recycled PE (CR21PE0.3). *Figure 2.4.9* shows the fatigue life of each mixture tested. The addition of recycled PE significantly reduced the fatigue life of the asphalt mixture. While the crumb rubber modification returned some of the fatigue performance, the unmodified control still retained the highest fatigue life.

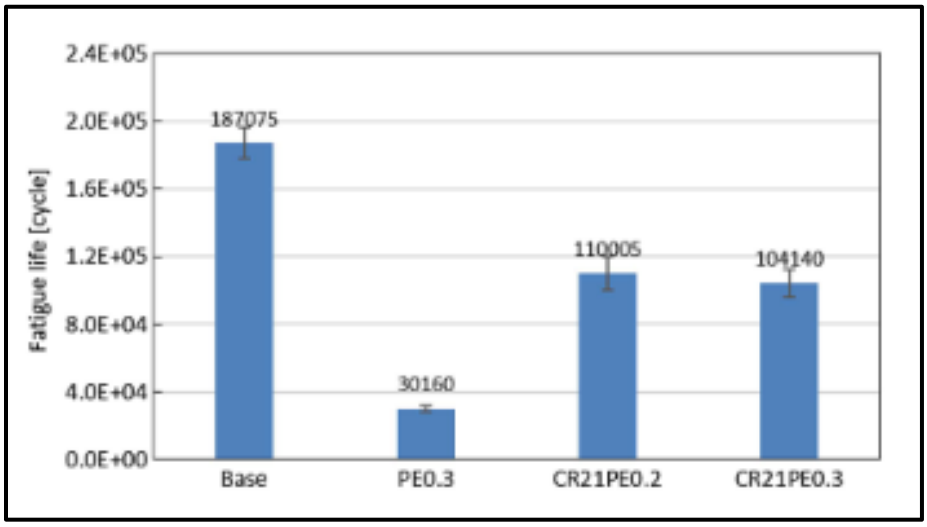

Figure 2.4.9: Fatigue Life of Asphalt Mixtures (Zhang et al., 2020)

Ibrahim et al. (2022) evaluated the fatigue life of the wet-process and dry-process recycled polyethylene (PE) modified asphalt mixtures and the unmodified control mixture via the Bending Beam Fatigue Test. This test was performed at three temperatures, with each temperature having a range of strain levels (ten in total). At 10 ºC: 300, 400, 500, and 700 με, at 20 ºC: 500, 700, and 900 με, and at 30 ºC: 900, 1100, and 1300 με. Testing was performed at a loading frequency of 10 Hz. *Figure 2.4.10* displays the fatigue life for each mixture at each testing condition. In general, for the tests conducted above 10 ºC, the mixtures modified with recycled PE had decreased fatigue life relative to the unmodified control mixture. Of the two mixtures containing recycled PE, the dry-process modified mixture displayed lower fatigue life.

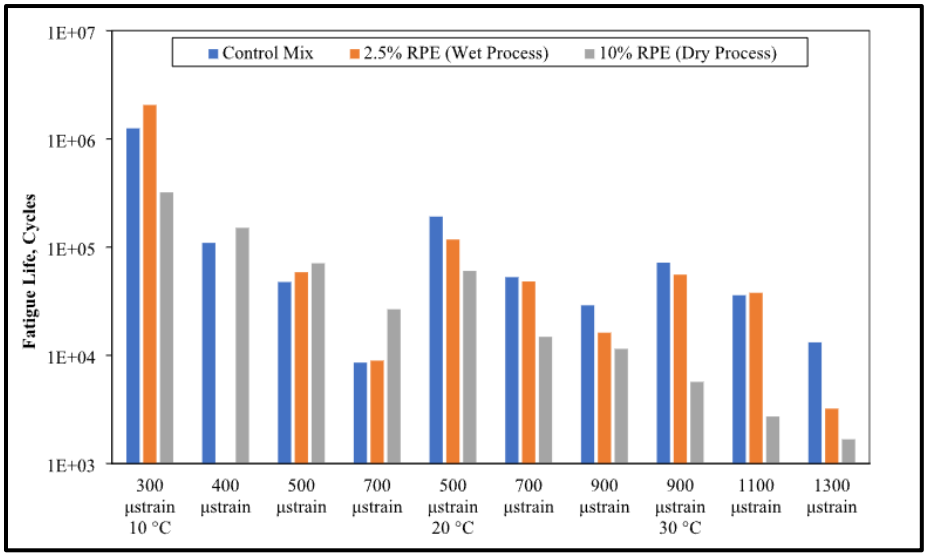

Figure 2.4.10: Fatigue Life of Asphalt Mixtures (Ibrahim et al., 2022)

The fatigue life of beam fatigue samples has been found to be heavily subject to influence by additives. Feiteira Dias et al. (2014) found that both wet-process and dry-process gap-graded CRM modified asphalt mixtures offered improved fatigue life over an unmodified gap-graded mixture, with the wet-process modified mixture offering more fatigue life than the dry-process. Similarly, Dantas et al. (2005) found that both wet-process and dry-process dense-graded CRM modified mixture offered improved fatigue life over an unmodified dense-graded mixture. However, it was found that the dry-process modified mixture greater more fatigue life than the wet-process. The differing conclusions as to which GTR additive technology offered the best fatigue life were likely due to a combination of gradation type and GTR dosage rates. Kaloush et al. (2010) evaluated the effect of a dry-process fiber additive technology on the fatigue of a dense-graded asphalt mixture. It was found that the unmodified control mixture exhibited greater fatigue life at high strain values whilst the fiber-modified mixture exhibited greater fatigue life at low strain values. Mateos and Harvey (2019) also evaluated the fatigue life of a dense-graded asphalt mixture modified with ACE XP^{TM} fibers. It was found that at higher strain levels the fiber-modified mixture showed an increase in its fatigue life. These findings were contradictory and display the different and potentially uncertain outcomes that fiber additive technologies may produce. The fatigue life of a dry-process recycled polyethylene (PE) modified mixture was evaluated versus an unmodified control mixture. The dry-process recycled PE mixture displayed significantly reduced fatigue life in comparison with the unmodified control mixture (Zhang et al., 2020). Ibrahim et al. (2022) evaluated the fatigue life of the wet-process and dry-process recycled polyethylene (PE) modified asphalt mixtures and the unmodified control mixture. It was found that the mixtures modified with recycled PE had decreased fatigue life relative to the unmodified control mixture. And that of the two mixtures containing recycled PE, the dry-process modified mixture displayed lower fatigue

life. The next chapter will provide insight into the composition of each AG, test specimen manufacturing, and laboratory testing procedures and conditions.

2.5: Conclusion

This chapter presented a brief overview of the five technologies included in the AG study, as well as how each has impacted the results of dynamic modulus (E*), direct tension cyclic fatigue, and bending beam fatigue laboratory test results in previous literature. The next two chapters will provide details regarding the asphalt mixture designs, additive types and dosage rates, mixture sampling and test specimen production, laboratory testing procedures and conditions, and a comprehensive analysis of the laboratory results, including how the results compare to previous literature detailed within this chapter.

CHAPTER 3

Laboratory Testing – Materials and Methods

3.1: Introduction

Three laboratory tests were performed as a part of the comprehensive laboratory characterization for each AG mixture. The dynamic modulus (E*) test which was performed in accordance with AASHTO TP 132-19 (Standard Method of Test for Determining the Dynamic Modulus for Asphalt Mixtures Using Small Specimens in the Asphalt Mixture Performance Tester (AMPT)). This test characterized mixture modulus and phase angle at three testing temperatures and three testing frequencies. Additionally, E* and phase angle master curves were established using Master Solver for Excel© Version 2.3 in accordance with AASHTO R 84-17 (Standard Practice for Developing Dynamic Modulus Master Curves for Asphalt Mixtures Using the Asphalt Mixture Performance Tester (AMPT)).

Laboratory fatigue performance was evaluated via the direct tension cyclic fatigue test. This test was performed in accordance with AASHTO TP 133-22 (Standard Method of Test for Determining the Damage Characteristic Curve and Failure Criterion Using Small Specimens in the Asphalt Mixture Performance Tester (AMPT) Cyclic Fatigue Test). Damage characteristic curves were developed for each AG mixture and the D^R failure criterion and S_{app} parameters were computed in order to rank their relative laboratory fatigue performance.

The fatigue lives of the AG mixtures were evaluated via the bending beam fatigue test. This test was performed in accordance with AASHTO T 321-22 (Standard Method of Test for Determining the Fatigue Life of Compacted Asphalt Mixtures Subjected to Repeated Flexural Bending). Transfer functions plotting the relationship between applied flexural strain and number of cycles to failure (N_f) were developed for each mixture. Additionally, the initial flexural stiffness of each mixture was recorded.

The sections within this chapter will provide the specifics regarding the mixture design and additive components, the necessary steps taken to sample each mixture and produce the small cylindrical performance test specimens and beam fatigue samples, the conditions under which each laboratory test was conducted, and any pertinent software tools used, or calculations made for laboratory data processing and/or analysis.

3.2: AG Asphalt Mixture Characterization

Six test sections were constructed at the NCAT Test Track as a part of the Additive Group (AG) experiment. Of these, five evaluated an additive technology, while one acted as the control, though still included SBS polymer modification. *Table 3.2.1* displays the specific additive formulations and/or product names, wet and/or dry-process dosage rates, and the final binder performance grade (PG) for each AG mixture. Each of the AG mixtures used the same base asphalt binder. This binder was a PG 67-22 prior to any wet-process modifications. Notably, N5 (Aramid) and S5 (DryPlastic) each received a wet-process SBS modification (identical to the control mixture) in addition to their respective dry-process modifications, bumping their high temperature PG up to a 76-22. N1

(GTRDry) was the only mixture to not receive some form of wet-process modification, reflected by its unchanged binder PG of 67-22.

Table 3.2.1: AG Mixture Additives

Mixture ID	Wet Modifier	Wet Modifier Dosage Rate	Virgin Binder PG	Modified Binder PG	Dry Modifier	Dry Modifier Dosage Rate
N1 (GTRDry)	None	N/A	67-22	67-22	SmartMIX™ (Liberty Tire Recycling)	12%
N2 (GTRWet)	Terminal Blended (TB) Rubber Binder (Entech, Inc.)	10%	67-22	76-22	None	N/A
N5 (Aramid)	SBS	3%	67-22	76-22	ACE XP™ (Surface Tech™)	2.1 oz/ton
N7 (Ctrl)	SBS	3%	67-22	76-22	None	N/A
S5 (DryPlastic)	SBS	3%	67-22	76-22	LLDPE	0.5% (by weight of aggregate)
S6 (Wet Plastic)	LLDPE + ELVALOY™ RET (Dow®) + PPA	1% LLDPE + 1.5% ELVALOY™ RET (Dow®) + 0.32% PPA	67-22	76-22	None	N/A

An identical 12.5 mm nominal maximum aggregate size (NMAS) dense-graded mixture design was used for each of the AG test sections. Each mixture design incorporated 20% reclaimed asphalt pavement (RAP) and 1.0% baghouse fines, with a design asphalt binder content of 5.6%. The gradation and volumetric targets along with their quality control (QC) values are shown in *Table 3.2.2* for each of the AG mixtures.

Table 3.2.2: AG Asphalt Mixture Gradations and Volumetric Properties

	N1 (GTRDry)		**N2 (GTRWet)**		**N5 (Aramid)**		**N7 (Ctrl)**		**S5 (DryPlastic)**		**S6 (WetPlastic)**	
	Target	QC	Target	QC	Target	QC	Target	QC	Target	QC	Target	QC
25 mm (1")	100	100	100	100	100	100	100	100	100	100	100	100
19 mm (3/4")	100	100	100	100	100	100	100	100	100	100	100	100
12.5 mm (1/2")	98	97	98	97	98	98	98	97	98	97	98	97
9.5 mm (3/8")	89	87	89	86	89	84	89	84	89	87	89	86
4.75 mm (#4)	55	59	55	57	55	54	55	54	55	56	55	56
2.36 mm (#8)	41	44	41	42	41	40	41	41	41	43	41	42
1.18 mm (#16)	33	34	33	32	33	31	33	32	33	33	33	32
0.60 mm (#30)	22	20	22	19	22	18	22	20	22	20	22	20
0.30 mm (#50)	12	10	12	10	12	9	12	10	12	9	12	10
0.15 mm (#100)	7	7	7	6	7	6	7	6	7	6	7	6
0.075 mm (#200)	4.5	4.3	4.5	4.1	4.5	3.8	4.5	4	4.5	3.8	4.5	4.0
Binder Content (Pb):	5.6	5.6	5.6	5.8	5.6	5.5	5.6	5.7	5.6	5.8	5.6	5.7
Eff. Binder Content (Pbe):	5.0	5.0	4.9	5.2	5.0	4.9	5.0	5.0	5.0	5.1	5.0	5.0
Dust-to-Eff. Binder Ratio:	0.9	0.9	0.9	0.8	0.9	0.8	0.9	0.8	0.9	0.7	0.9	0.8
RAP Binder Replacement (%):	21	20	21	19	21	20	21	20	21	19	21	20
Total Binder Replacement (%):	21	20	21	19	21	20	21	20	21	19	21	20
Rice Gravity (Gmm):	2.453	2.449	2.457	2.453	2.453	2.465	2.453	2.455	2.453	2.439	2.453	2.463
Bulk Gravity (Gmb):	2.344	2.328	2.314	2.351	2.344	2.350	2.344	2.369	2.344	2.359	2.344	2.333
Air Voids (Va):	4.4	4.9	5.8	4.2	4.4	4.7	4.4	3.5	4.4	3.3	4.4	5.3
Aggregate Gravity (Gsb):	2.627	2.622	2.627	2.636	2.627	2.639	2.627	2.632	2.627	2.616	2.627	2.641
VMA (via Gsb):	15.8	16.2	16.8	16	15.8	15.8	15.8	15.1	15.8	15.0	15.8	16.7
VFA:	72	69	65	74	72	71	72	77	72	78	72	68

3.3: Material Sampling and Preparation

Each AG asphalt mixture was sampled during construction of its section at the NCAT Test Track in accordance with AASHTO R97-19 (Standard Practice for Sampling Asphalt Mixtures). In short, during the construction of the test sections, mix was sampled from one of the trucks and placed on the side of the work zone in a cone-shaped pile using a skid loader. The sampled mix was then shoveled into 5-gallon metal buckets and taken to the NCAT laboratory for storage (*Figure 3.3.1*). The laboratory tests were performed using plant-mixed, laboratory-compacted (PMLC) samples.

Figure 3.3.1: Example of Sampled AG Mixture

At the NCAT laboratory, the sampled mixtures were prepared for compaction in accordance with AASHTO R47-22 (Standard Practice for Reducing Samples of Asphalt Mixtures to Testing Size). Buckets containing the sampled mix were heated in the oven for approximately 3 hours at 300°F, until the mix was capable of passing through the Type A mechanical splitter (*Figure 3.3.2*). Each mixture was quartered and reduced into 4000-g (approximately) bagged samples. This process facilitated the manufacturing of small cylindrical performance test specimens and beam fatigue specimens and also mitigated any risk of mixture segregation.

Figure 3.3.2: Sample Splitting with Type A Mechanical Splitter

Figure 3.3.3: Specimen Quartering and Reduction

3.4: Dynamic Modulus (E) and Direct Tension Cyclic Fatigue Test Specimen Production*

Small cylindrical performance test specimens were prepared for the dynamic modulus (E*) and direct tension cyclic fatigue tests in accordance with AASHTO T 312 (Standard Method of Test for Preparing and Determining the Density of Asphalt Mixture Specimens by Means of the Superpave Gyratory Compactor) and AASHTO PP 99-19 (Standard Practice for Preparation of Small Cylindrical Performance Test Specimens Using the Superpave Gyratory Compactor (SGC) or Field Cores). The asphalt mixtures were reheated in the oven at a temperature of 310°F for approximately 2 ½ hours, or until the samples reached the compaction temperature of 300°F. A Superpave gyratory compactor (SGC), shown in *Figure 3.4.1*, was used to compact SGC "pills" to 180 mm in height and 150 mm in diameter. The air void content of the SGC specimens was computed in accordance with AASHTO T 166 (Standard Method of Test for Bulk Specific Gravity of Compacted Asphalt Mixtures Using Saturated Surface-Dry Specimens). Though this step was not strictly necessary, as only the percent air voids of the final cored and cut test specimens was required for acceptance, it was useful for establishing the precise mass of asphalt mixture that should be added to the mold. Four test specimens were extracted from the center 100 mm diameter of the SGC "pill" (*Figure 3.4.2*) using the core drill shown in *Figure 3.4.3*. Each cored test specimen had a diameter of approximately 38 mm. Both ends of each cored test specimen removed via a wet saw (*Figure 3.4.4*), such that the final height of the test specimen was 110 +/- 2.5 mm. Test specimen dimensions, including average diameter, standard deviation of diameter, height, end flatness, and end perpendicularity were measured, recorded, and compared against the acceptance criteria detailed by AASHTO PP 99-19. The percent air voids of each small cylindrical performance test specimen were computed in accordance with AASHTO T 166 and compared against the acceptance criterion of 7.0 +/- 0.5%. *Figure 3.4.5* shows an example of a small cylindrical performance specimen that met the acceptance criterion.

Figure 3.4.1: Superpave Gyratory Compactor

Figure 3.4.2: SGC Specimen with Coring Guide Markings

Figure 3.4.3: Small Specimen Core Drill

Figure 3.4.4: Small Specimen Wet Saw

Figure 3.4.5: Example of Final Small Cylindrical Performance Test Specimen

3.5: Dynamic Modulus (E) Testing*

Small cylindrical performance test specimens that met volumetric and dimensional criteria were selected for dynamic modulus (E*) testing in accordance with AASHTO TP 132-19. *Figure 3.5.1* displays the IPC Global© Asphalt Mixture Performance Tester (AMPT) that was used to conduct the tests. Three E* test replicates were performed for every AG asphalt mixture. Each E* test replicate utilized a unique test specimen. Three testing temperatures of 4, 20, and 40°C, and three loading frequencies of 0.1, 1, and 10 Hz were used. *Figure 3.5.2* displays an example of an E* small cylindrical performance test specimen with its LVDT gauge points attached. The IPC Global© software was used to record the E* and phase angle of each AG test specimen and to check the data quality indicators against the criteria outlined within AASHTO TP 132-19.

Figure 3.5.1: IPC Global© AMPT Used for E Testing*

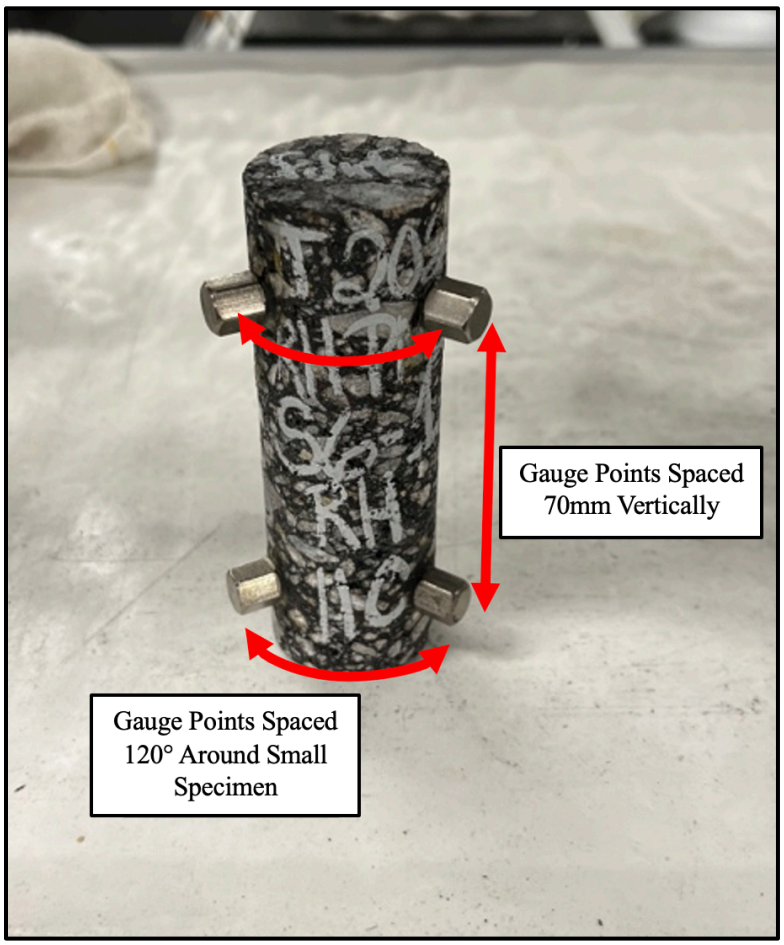

Figure 3.5.2: E Test Sample with Gauge Points*

The IPC Global© software recorded raw E* and phase angle measurements (and associated data quality indicators) were recorded at each testing temperature and frequency combination. *Figure 3.5.3* displays a screen capture of the raw E* and phase angle output for a single test replicate, at a temperature of 20°C and frequencies of 0.1, 1, and 10 Hz within the IPC Global© software.

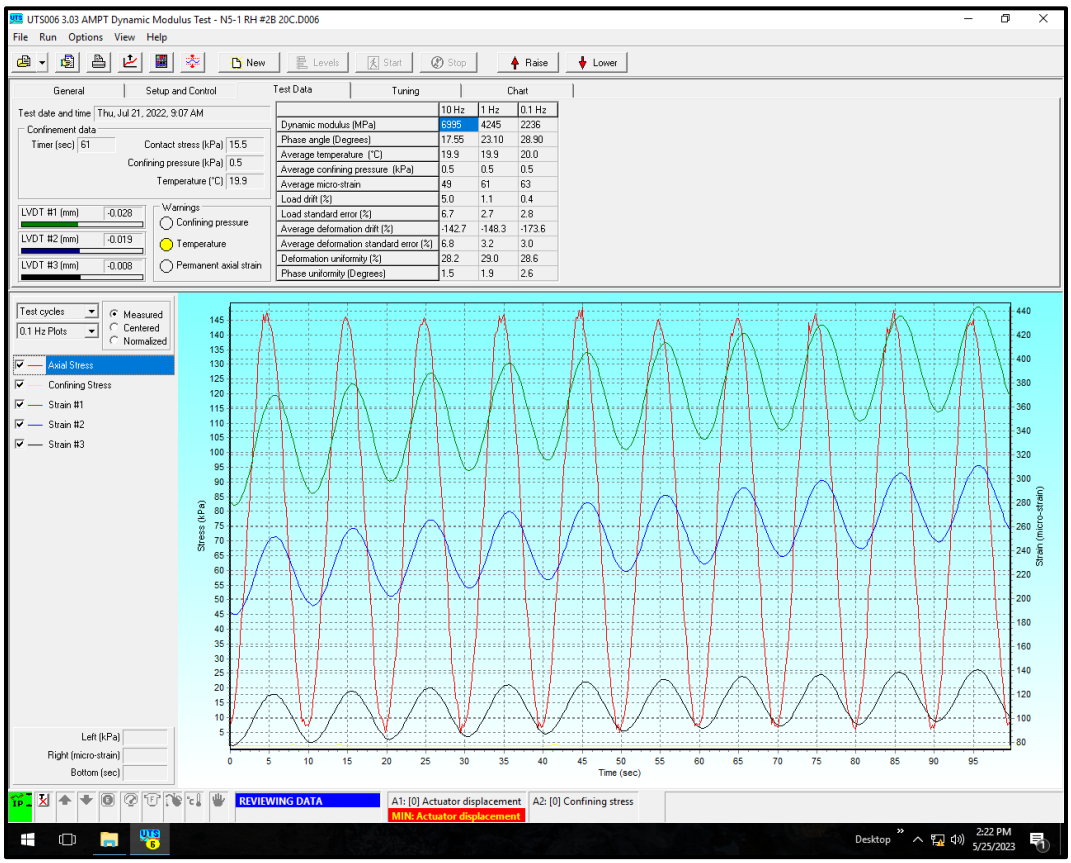

Figure 3.5.3: Example E Testing Output*

Master Solver for Excel© Version 2.3 was used to produce E* and phase angle master curves for each AG asphalt mixture in accordance with AASHTO R 84-17. The spreadsheet utilizes raw E* test data (dynamic modulus and phase angle values at their respective testing temperatures and loading frequencies), mixture voids in the mineral aggregate (VMA) and voids filled with asphalt (VFA), and the reference temperature as inputs. The spreadsheet also provides initial guesses for the minimum limiting modulus, as well as the β, γ, and activation energy (E_a) fitting parameters. The Excel© solver tool is used to optimize each fitting parameter in order to reduce the sum of square error between the log average measured and log average fitted E* and phase angle values. The optimized values for the fitting parameters are substituted into *Equation 3.5.3* to produce a final E* master curve equation for a given asphalt mixture. *Figure 3.5.4* displays an example E* master curve for the N7 (Ctrl) mixture. Also shown are the E* values at their actual testing temperatures before the application of any shift factors.

The following equations were utilized by Master Solver for Excel© Version 2.3 to produce the E* master curve equations for each mixture. *Equation 3.5.1* displays the general form of the E* master curve equation as provided by AASHTO R 84-17. This equation is a modified form of the one provided by the Mechanistic Empirical Design Guide (MEPDG) software. The reduced frequency is given *by Equation 3.5.2*. Substituting *Equation 3.5.2* into *Equation 3.5.1* yields *Equation 3.4.3*.

$$\log|E^*| = \log(Min) + \frac{((\log(Max)-\log(Min))}{1+e^{\beta+\gamma\log\omega_r}} \qquad \textit{Equation 3.5.1}$$

Where:

E* = dynamic modulus, ksi
ω_r = reduced frequency, Hz
Max = limiting maximum modulus, ksi
Min = limiting minimum modulus, ksi
β = fitting parameter
γ = fitting parameter

$$\log(\omega_r) = \log(\omega) + \frac{\Delta E_a}{19.14714}\left(\frac{1}{T} - \frac{1}{T_r}\right) \qquad \textit{Equation 3.5.2}$$

Where:

ω_r = reduced frequency @ the reference temperature, Hz
ω = reduced frequency @ the test temperature, Hz
T_r = reference temperature, °K
T = test temperature, °K
ΔE_a = activation energy (fitting parameter)

$$\log|E^*| = \log(Min) + \frac{((\log(Max)-\log(Min))}{1+e^{\beta+\gamma\left(\log(\omega)+\frac{\Delta E_a}{19.14714}\left(\frac{1}{T}-\frac{1}{T_r}\right)\right)}} \qquad \textit{Equation 3.5.3}$$

Equation 3.5.4 computes the shift factors for each testing temperature.

$$\log(a(T)) = \frac{\Delta E_a}{19.14714}\left(\frac{1}{T} - \frac{1}{T_r}\right) \qquad \textit{Equation 3.5.4}$$

Where:

a(T) = shift factor at the testing temperature
T_r = reference temperature, °K
T = test temperature, °K
ΔE_a = activation energy (fitting parameter)

Equation 3.5.5 estimates the maximum limiting modulus via the Hirsch model. The Hirsch model uses the volumetric properties of the asphalt mixture (voids filled with asphalt (VFA) and voids in the mineral aggregate (VMA)) and a limiting asphalt binder modulus of 145,000 psi to make this estimate. The maximum limiting modulus functions as an asymptote (i.e., an upper limit) that the fitted master curve cannot exceed.

$$|E^*|_{max} = P_c\left[4{,}200{,}000\left(1-\frac{VMA}{100}\right) + 435{,}000\left(1-\frac{VFA*VMA}{100}\right)\right] + \frac{1-P_c}{\left[\frac{\left(1-\frac{VMA}{100}\right)}{4{,}200{,}000}+\frac{VMA}{435{,}000*VFA}\right]} \qquad \textit{Equation 3.5.5}$$

Where:

$$P_c = \frac{\left(20+\frac{435{,}000*VFA}{VMA}\right)^{0.58}}{650+\left(\frac{435{,}000*VFA}{VMA}\right)^{0.58}} \qquad \textit{Equation 3.5.6}$$

Where:

E^*_{max} = maximum limiting modulus, ksi
VMA = voids in the mineral aggregate, %
VFA = voids filled with asphalt, %

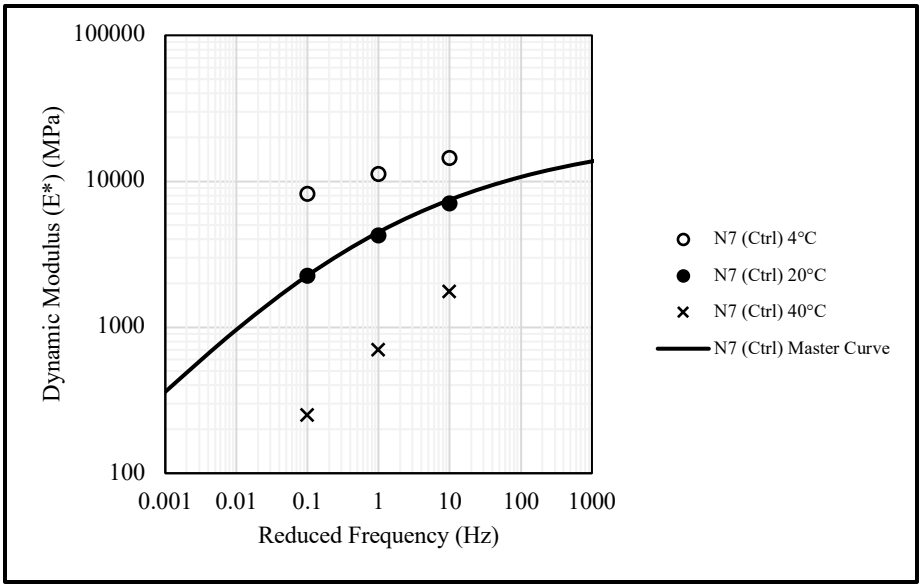

Figure 3.5.4: Example E Master Curve for N7 (Ctrl)*

The Glover-Rowe parameter (G-R_m) was calculated for each AG mixture. *Equation 3.5.7* provides the calculation for determining the G-R_m. This parameter evaluates mixture ductility via the dynamic modulus and phase angle at a temperature of 20°C and a loading frequency of 5 Hz. The G-R_m is used to evaluate the relative block cracking potential of asphalt mixtures (i.e., mixtures with a higher G-R_m are more susceptible to this form of cracking). Because E* testing was not conducted at a loading frequency of 5 Hz (only 0.1, 1, and 10 Hz tests were conducted), the phase angle at this frequency was linearly interpolated. Additionally, the E* master curve equations were used to estimate the E* magnitude at 5 Hz.

$$G - R_m = \frac{|E^*|*[\cos\delta]^2}{\sin\delta} \qquad \textit{Equation 3.5.7}$$

Where:

E* = dynamic modulus @ 20°C and 5 Hz, ksi
δ = phase angle @ 20°C and 5 Hz, °

3.6: Direct Tension Cyclic Fatigue Testing

Small cylindrical performance test specimens that met volumetric and dimensional criteria were selected for cyclic fatigue testing. Testing was performed in accordance with AASHTO TP 133-22. An IPC Global© Asphalt Mixture Performance Tester (AMPT) Pro (*Figure 3.6.1*) was used to perform AASHTO TP 133-22. Three direct tension cyclic fatigue test replicates were performed for every AG asphalt mixture. Each test replicate utilized a unique test specimen. *Figure 3.6.2* displays an example cyclic fatigue small cylindrical performance test specimen with the LVDT gauge points (spaced 120° apart) and platens attached.

Figure 3.6.1: IPC Global© AMPT Pro Used for Cyclic Fatigue Testing

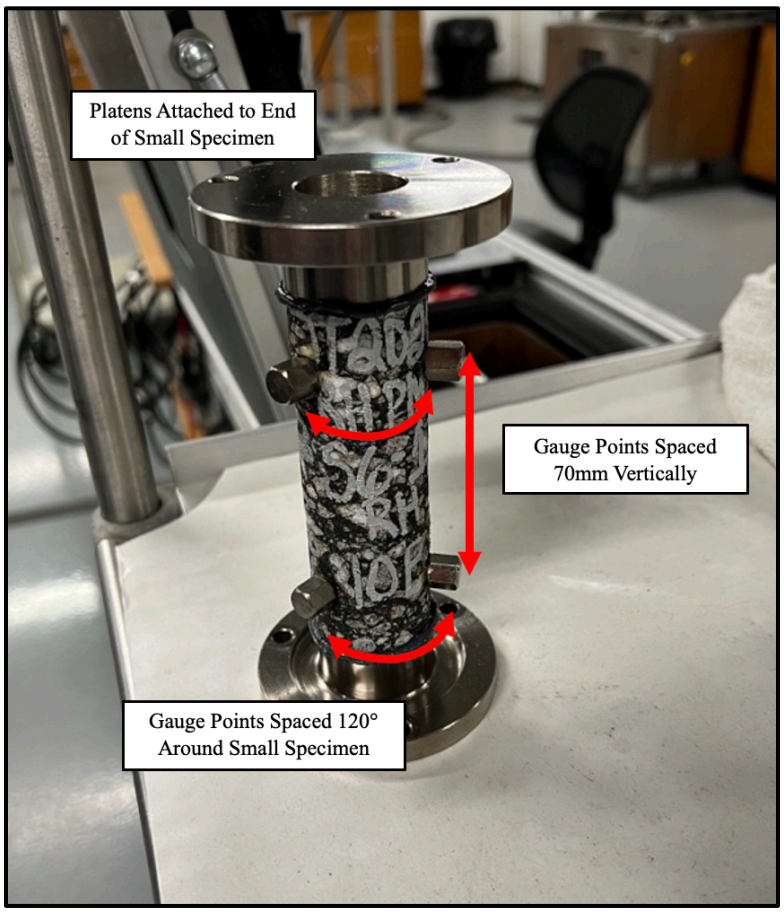

Figure 3.6.2: Cyclic Fatigue Test Specimen with Gauge Points and Platens

Direct tension cyclic fatigue testing was performed at a temperature of 21°C. Initial strain values varied between 450 and 550 με, depending on the relative stiffness of the AG mixtures. Stiffness was evaluated via the specimen's fingerprint dynamic modulus ($E^*_{fingerprint}$). This was determined at the testing temperature (21°C), a loading frequency of 10 Hz, and a loading level that induced strain level between 50 and 75 με. Using the $E^*_{fingerprint}$ results, the initial strain level for each AG mixture was selected using the chart provided by Appendix X.1.1 of AASHTO TP 133-2. The dynamic modulus ratio (DMR) of each test specimen was determined by taking the ratio of the $E^*_{fingerprint}$ and the E^*_{LVE} resulting from AASHTO TP 132-19 (at the pertinent testing temperature (21°C) and frequency (10 Hz)). In order for cyclic fatigue data to be considered valid it had to have a DMR value between 0.85 and 1.15. Additionally, a middle failure type had to occur within a range of 2,000 to 80,000 cycles. The number of cycles to failure (N_f) was defined as the cycle at which the peak-to-peak stress x cycles curve reached a maximum value. These acceptance criteria were provided by AASHTO TP 133-22.

FlexMAT™ Cracking v2.1.1 was used to perform the cyclic fatigue data analysis and calculations per AASHTO TP 133-22. For each AG mixture, a pseudo stiffness (C) versus damage (S) or "damage characteristic curve" was fitted to the plot of C versus S data from all

successful test replicates performed for that mixture. *Figure 3.6.3* displays an example of a fitted damage characteristic curve for the AG control mixture (N7). Additionally, fitted D^R failure criterion and S_{app} parameters were computed for each AG mixture. Climactic data for Auburn, AL (Lee County) was utilized for the computation of the fitted S_{app} parameters.

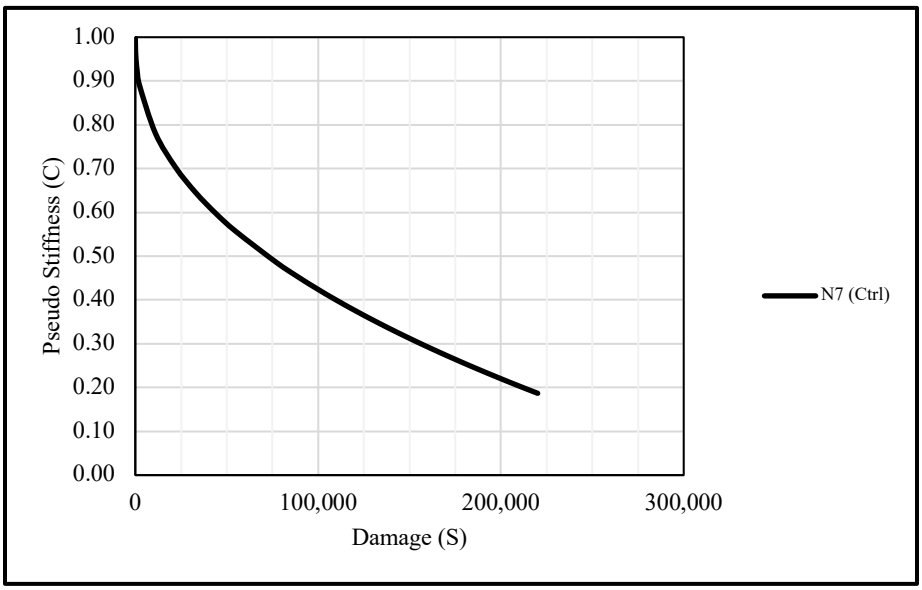

Figure 3.6.3: Example Damage Characteristic Curve for N7 (Ctrl)

3.7: Bending Beam Fatigue Test Specimen Production

Beam fatigue test specimens were prepared for the bending beam fatigue test (AASHTO T 321-22). Like the small cylindrical performance test specimens, the beam fatigue test specimens were plant-mixed and laboratory-compacted (PMLC), utilizing the same asphalt mixtures sampled during the AG section construction at the NCAT Test Track. Beam fatigue specimens were roller-compacted per the acceptable methods outlined by AASHTO T 321-22. A custom manufactured beam compactor that was readily available at the NCAT laboratory was used (*Figure 3.7.1*). In preparation for compaction, each asphalt mixture was reheated in the oven at a temperature of 310°F for approximately 2 ½ hours, or until the samples reached the compaction temperature of 300°F. Wax paper was placed in the bottom of the compaction mold, then the asphalt mixture was deposited within the mold, and another wax paper was placed on top of the asphalt mixture. The compaction mold was transferred to the beam compactor and secured inside. Metal plates were inserted one at a time until the mold opening was filled. A vertical hydraulic cylinder lowered the roller wheel until it pressed the plates flush with the edges of the mold. A horizontal hydraulic cylinder jogged the mold back and forth underneath the roller wheel, pressing all plates flush with the edges of the mold. Once 8 passes had been completed, and all plates were flush with the edges of the mold, the sample had been fully compacted. The plates were then removed via a magnet, and the mold was removed from the compactor and allowed to cool overnight. The compacted

specimen was extracted from the mold the following day. *Figure 3.7.2* displays an example of a compacted beam fatigue specimen prior to being saw-cut. The air void content of the compacted beam specimens was computed in accordance with AASHTO T 166. Though this step was not strictly necessary, as only the percent air voids of the final saw-cut beam fatigue test specimens was required for acceptance, it was useful for establishing the precise mass of asphalt mixture that should be added to the mold. Per AASHTO T 321-22, the compacted beam specimens were saw-cut to height of 50 +/- 6 mm, a width of 63 +/- 6 mm, and a length of 380 +/- 6 mm using the wet saw shown by *Figure 3.6.3*. Beam fatigue test specimen height, width, and length were each measured in three separate locations. The average of each dimension was computed and compared against the acceptance criteria detailed above. The percent air voids of each beam fatigue test specimen was computed in accordance with AASHTO T 166, with an acceptance criterion of 7.0 +/- 1.0%. *Figure 3.7.4* shows an example of a beam fatigue specimen that met the acceptance criteria.

Figure 3.7.1: Beam Fatigue Specimen Compactor

Figure 3.7.2: Compacted Beam Fatigue Specimen

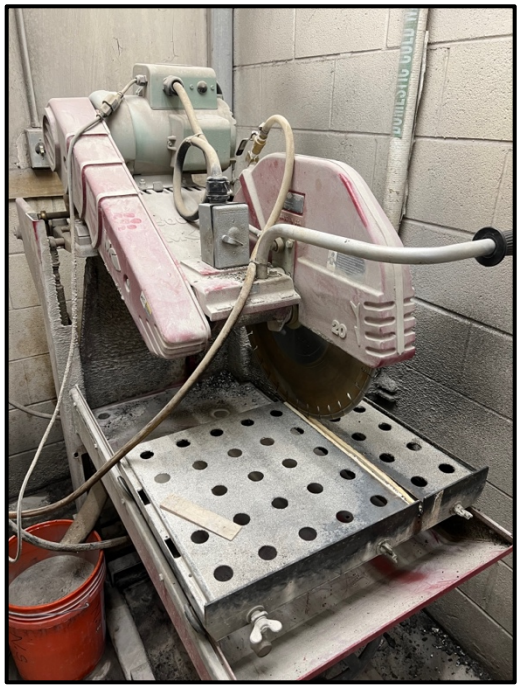

Figure 3.7.3: Beam Fatigue Specimen Wet Saw

Figure 3.7.4: Example of Final Beam Fatigue Test Specimen

3.8: Bending Beam Fatigue Testing

The bending beam fatigue test was performed in accordance with AASHTO T321-22. *Figure 3.8.1* displays an example of a beam fatigue specimen within the IPC Global© machine used for the testing. Tests were conducted in a controlled strain mode, at a temperature of 68°F, using a loading frequency of 10 Hz. For each AG mixture, three flexural strain levels were tested. Three replicates (each utilizing a unique test specimen) were performed at each flexural strain level. AASHTO T321-22 defines the minimum acceptable number of cycles to failure (N_f) for defining the fatigue life of a test specimen as 10,000. The standard also provides a practical upper limit for N_f of 1,000,000. For most of the AG mixtures tested, the low flexural strain level was 400 με, the medium was 600 με, and the high was 800 με. However, N2 (GTRWet) displayed a much greater fatigue life at 400 με in comparison to the other AG mixtures, exceeding the practical upper N_f limit provided by AASHTO T 321-22. Therefore N2 (GTRWet) was tested at 600 με, 800 με, and 1000 με. The IPC Global© monitoring and recording software produced a raw Excel© output spreadsheet that included the loading cycle, maximum peak-to-peak tensile stress, maximum peak-to-peak tensile strain, flexural stiffness, and flexural stiffness x cycles. This Excel© output was used to determine the fatigue life of each test specimen.

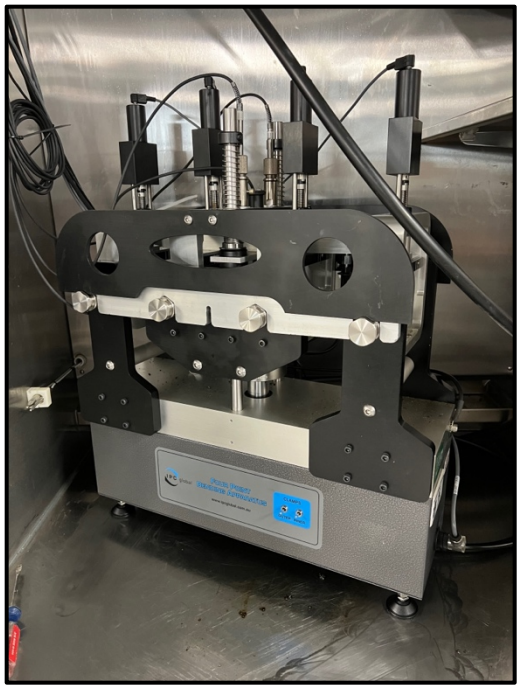

Figure 3.8.1: IPC Global© Beam Fatigue Test Machine

The maximum peak-to-peak tensile stress and peak-to-peak tensile strain are given by *Equation 3.8.1* and *Equation 3.8.2*, respectively. The calculation for determining the flexural stiffness of a beam fatigue sample is shown by *Equation 3.8.3*.

$$\sigma_t = \frac{0.357P}{bh^2} \qquad \textit{Equation 3.8.1}$$

Where:

P = peak to peak applied load, N
b = beam specimen width, m
h = beam specimen height, m

$$\epsilon_t = \frac{12\delta h}{3L^2 - 4a^2} \qquad \textit{Equation 3.8.2}$$

Where:

δ = maximum peak-to-peak deflection measured at the center of the beam specimen, m
a = space between the inside machine clamps, 0.357/3 m
L = length of beam specimen outside of the machine clamps, 0.357 m

$$S = \frac{\sigma_t}{\epsilon_t} \qquad \textit{Equation 3.8.3}$$

AASHTO T321-22 defines the flexural fatigue failure point as being the loading cycle at which the flexural stiffness x cycles curve reaches a maximum value and then begins to decline. *Figure*

3.8.2 displays an example of a flexural stiffness x cycles curve (red line) with a defined failure point (green circle) for a beam fatigue specimen tested at 600 με. Additionally, *Figure 3.8.2* plots the stiffness versus cycles curve (black line) for the same test specimen to illustrate the effects of damage accumulation. N_f for this test specimen was determined to be 277,500. The initial flexural stiffness of each fatigue sample was evaluated at the 50th loading cycle (blue circle) per AASHTO T321-22. The beam fatigue specimen discussed above was found to have an initial flexural stiffness of approximately 4,700 MPa.

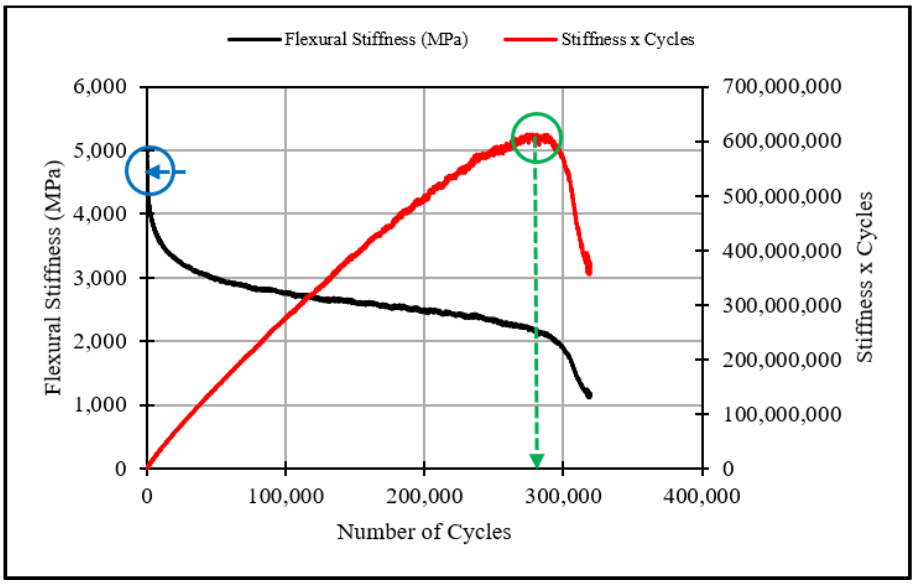

Figure 3.8.2: Example Beam Fatigue Data Output

For each AG mixture, the N_f and flexural strain level were plotted against each other. In this way, the strain tolerance of each AG mixture was defined via a fatigue life transfer function. *Equation 3.8.4* describes the general form of these fatigue life transfer functions. *Figure 3.8.3* displays the fatigue transfer function for the N7 (Ctrl) mixture. N_f is plotted versus applied flexural strain level on a log-log scale. A power regression function was fitted to numerically describe the fatigue life relationship, in the form of *Equation 3.8.4*.

$$N_f = k_1 \frac{1}{\epsilon}^{k_2} \qquad \textit{Equation 3.8.4}$$

Where:

N_f = number of cycles to failure
ε = initial strain level
k_1 = fitting coefficient
k_2 = fitting coefficient

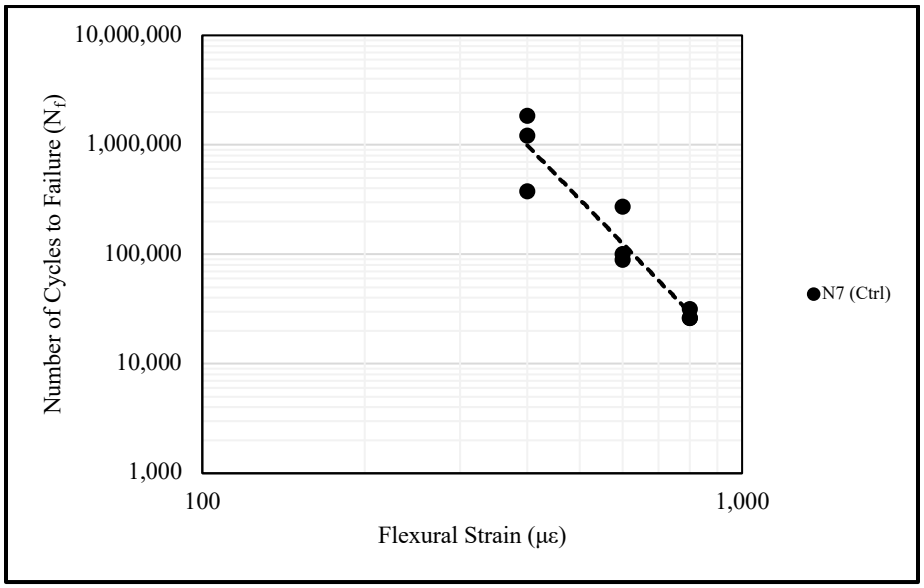

Figure 3.8.3: Example Fatigue Life Transfer Function for N7 (Ctrl)

3.8: Summary

This chapter provided a detailed overview of each mixture design, as well as the necessary steps taken to sample each mixture and produce the test specimens for AASHTO TP 132-19, AASHTO TP 133-22, and AASHTO T 321-22. Also defined were the conditions and setup of each laboratory test, and any software tools that were used or calculations that were performed as a part of data processing and/or analysis. The next chapter will present and discuss the results of each laboratory test, as well as how those results relate to the findings of the studies outlined within the previous chapter.

CHAPTER 4

Laboratory Testing – Results & Discussion

4.1: Introduction

The dynamic modulus (E*), direct tension cyclic fatigue, and bending beam fatigue tests were performed in accordance with AASHTO TP 132-19, AASHTO TP 133-22, and AASHTO TP 321-22, respectively. From AASHTO TP 132-19, E* and phase angle were measured at three loading frequencies and three testing temperatures. Two master curves were constructed for each AG mixture. These master curves plotted E* and phase angle versus the reduced frequency. From AASHTO TP 133-22, damage characteristic curves that described the pseudo stiffness (C) versus damage (S) relationship were constructed. Mixture toughness was evaluated via the D^R failure criterion, and the S_{app} parameters were computed in order to rank the laboratory fatigue performance of the AG mixtures. Finally, from AASHTO T 321-22, the initial flexural stiffness and the fatigue life of each AG mixture was evaluated. Power regression "transfer" functions that described the relationship between number of cycles to failure (N_f) and applied flexural strain level were developed to characterize mixture fatigue life. The following sections detail the results, subsequent statistical analysis (if applicable) of each of the laboratory tests.

4.2: Dynamic Modulus (E) Test Results*

The dynamic modulus (E*) test was performed in accordance with AASHTO TP 132-19. E* values were recorded for each AG mixture at three testing temperatures (4, 20, and 40ºC) and three loading frequencies (0.1, 0, and 10Hz). The E* data presented in the following figures represents the average of three test replicates (each utilizing a unique small cylindrical performance test specimen). *Figure 4.2.1*, *Figure 4.2.2*, and *Figure 4.2.3* display the E* values for the AG mixtures at the three testing temperatures for each loading frequency (for 0.1, 1, and 10 Hz, respectively). For each testing temperature and frequency combination, an ANOVA was performed, using a level of significance (α) of 0.05, to determine if the average E* values for the AG mixtures were significantly different from one another (see *Table A.1.1* for the E* ANOVA computations). Following the ANOVA, a Tukey-Kramer analysis was performed, also using an α of 0.05, to determine which of the mixtures had statistically similar average E* values (see *Table A.1.2* for the E* Tukey-Kramer computations). A letter-based nomenclature was utilized to denote which mixtures had statistically similar average E* values. Mixtures that share common letters have a statistically similar average E*.

E* master curves were developed for each AG mixture at a reference temperature of 20ºC using Master Solver for Excel© Version 2.3 in accordance with AASHTO R 84-17. *Figure 4.2.4*, *Figure 4.2.5*, and *Figure 4.2.6* display the E* master curves for the rubber-modified, fiber-modified, and plastic-modified mixtures, respectively. The E* master curve of the control mixture was included on each plot for comparison.

The E*'s of N1 (GTRDry) and N2 (GTRWet) were found to be numerically lower at most of the testing frequencies and temperatures in comparison to N7 (Ctrl). At 4ºC, the E*'s of N1 (GTRDry)

and N2 (GTRWet) were found to be statistically lower than the E* of N7 (Ctrl) and the other AG mixtures. These trends are clearly displayed by the E* master curves of N1 (GTRDry) and N2 (GTRWet), which are positioned below N7 (Ctrl) across most of the reduced frequency range. *Table 3.2.1* characterizes the additive technologies and dosage rates, as well as the final asphalt binder PGs, for each AG mixture. N1 (GTRDry) utilized a PG 67-22 asphalt binder with a dry-process GTR additive added at the mixing plant. N2 (GTRWet) utilized a terminally blended PG 76-22 asphalt binder, modified with wet-process GTR additive. Within this paper, the rubber-modified mixtures are consistently compared to the control mixture, which utilized a PG 76-22 asphalt binder, modified with SBS via the wet-process. Previous studies have demonstrated that dry-process and wet-process rubber-modification both increase the E* of asphalt mixtures (Jin et al., 2023) and (Xie and Shen, 2016). SBS-modification also has been demonstrated to increase E* to an even greater degree than GTR-modification (Xie and Shen, 2016). Therefore, the lower values of E* observed for N1 (GTRDry) and N2 (GTRWet) relative to N7 (Ctrl) is consistent with what is generally understood about respective the E* effects brought about by the addition of these three technologies to asphalt mixtures.

The fiber-modified mixture, N5 (Aramid), and the wet-process plastic-modified mixture, S6 (WetPlastic), both displayed no statistical difference in their average E* relative to N7 (Ctrl) at any testing temperature or frequency. This was reflected by the E* master curves of these mixtures, which appear to be nearly identical. One previous research study found that dry-process fiber modification significantly increased E* across the entire reduced frequency range (Kaloush et al. 2010), while another observed no significant increases in E*, except at the highest testing temperature, where a slight increase was observed (Mateos and Harvey, 2019). The lack of any significant difference between the measured E* values of N5 (Aramid) and N7 (Ctrl) makes sense given that they utilized the same PG 76-22 SBS-modified asphalt binder, and previous research provides conflicting results as to whether fiber-modification noticeably impacts the E* of asphalt mixtures.

The E*'s of the wet-process and dry-process plastic-modified mixtures were found to be significantly different from one another. The E* of S5 (DryPlastic) was statistically greater than N7 (Ctrl) at most testing temperatures and frequencies. This finding is clearly displayed by E* master curves of the two mixtures relative to one another. The increased E* of S5 (DryPlastic) was likely due to its dry-process rPE modification, which has been shown to increase the E* of mixtures (Abdalfattah et al., 2022), combined with the utilization of the 76-22 SBS-modified asphalt binder. This was the same asphalt binder used for other AG mixtures, including N7 (Ctrl). The E* S6 (WetPlastic) was found to be statistically identical to that of N7 (Ctrl) at every testing temperature and frequency. This is reflected by their two E* master curves, which are overlayed on top of one another. Wet-process polymer-modification has been shown to increase E* (Abdalfattah et al., 2022). Given this information, and the fact that S6 (WetPlastic) and N7 (Ctrl) each utilized a separate form of wet-process polymer modification that resulted in asphalt binders with identical PGs, these E* findings make sense.

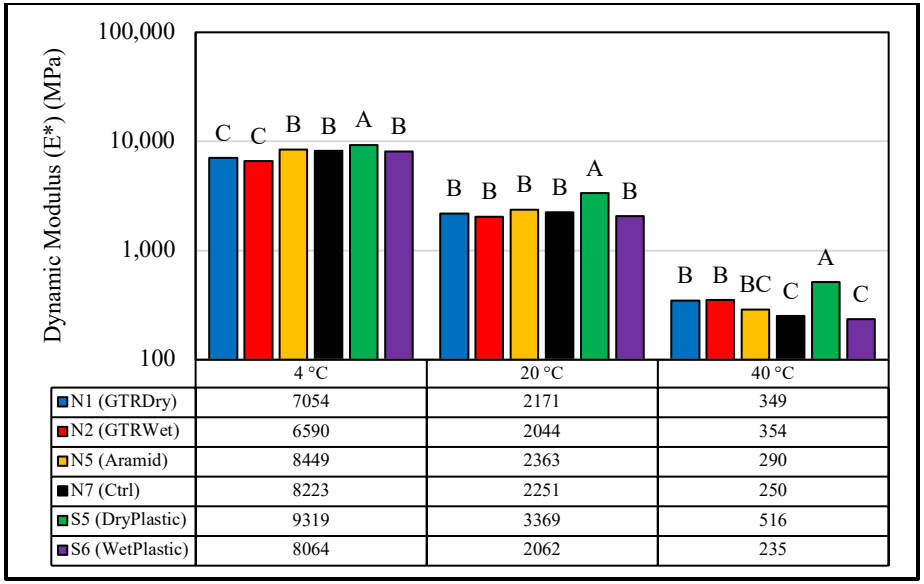

	4 °C	20 °C	40 °C
N1 (GTRDry)	7054	2171	349
N2 (GTRWet)	6590	2044	354
N5 (Aramid)	8449	2363	290
N7 (Ctrl)	8223	2251	250
S5 (DryPlastic)	9319	3369	516
S6 (WetPlastic)	8064	2062	235

Figure 4.2.1: Average E at Each Temperature (0.1 Hz)*

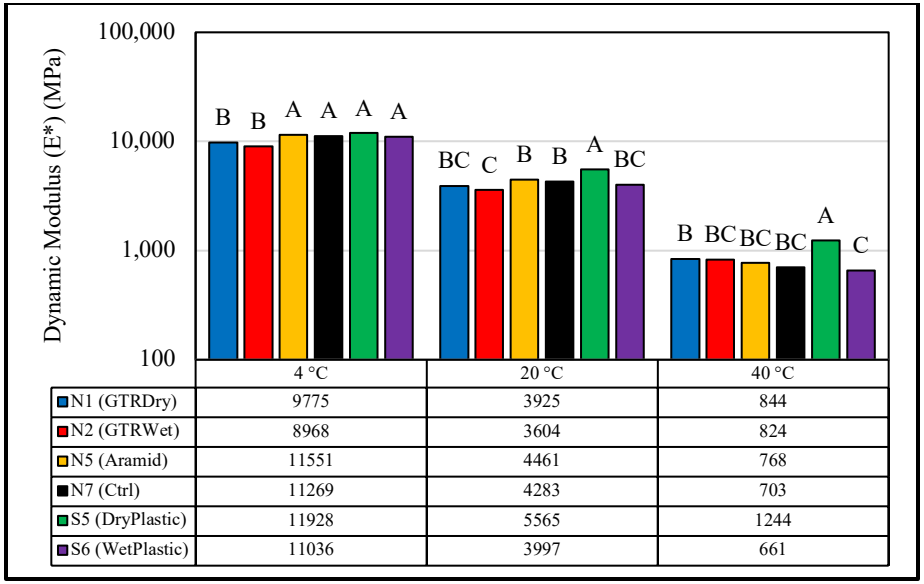

	4 °C	20 °C	40 °C
N1 (GTRDry)	9775	3925	844
N2 (GTRWet)	8968	3604	824
N5 (Aramid)	11551	4461	768
N7 (Ctrl)	11269	4283	703
S5 (DryPlastic)	11928	5565	1244
S6 (WetPlastic)	11036	3997	661

Figure 4.2.2: Average E at Each Temperature (1 Hz)*

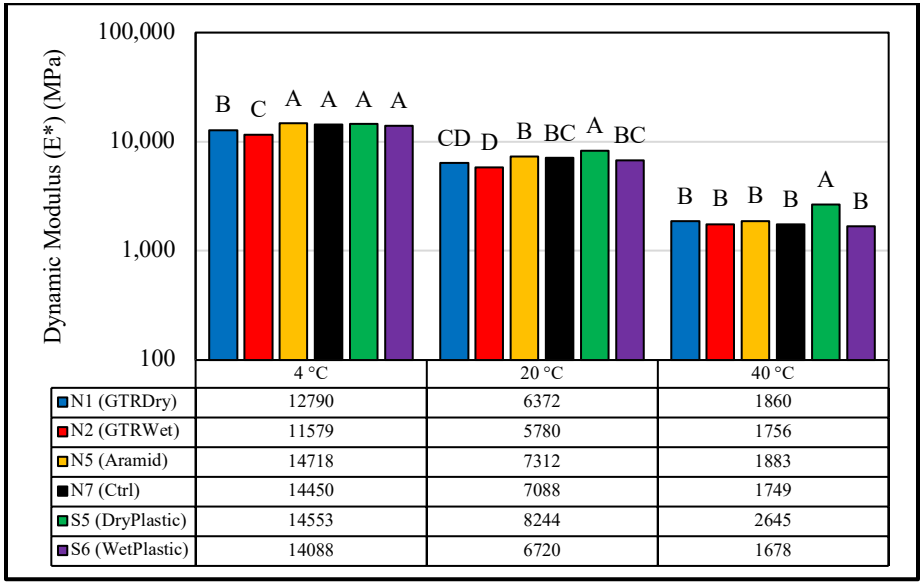

	4 °C	20 °C	40 °C
N1 (GTRDry)	12790	6372	1860
N2 (GTRWet)	11579	5780	1756
N5 (Aramid)	14718	7312	1883
N7 (Ctrl)	14450	7088	1749
S5 (DryPlastic)	14553	8244	2645
S6 (WetPlastic)	14088	6720	1678

Figure 4.2.3: Average E at Each Temperature (10 Hz)*

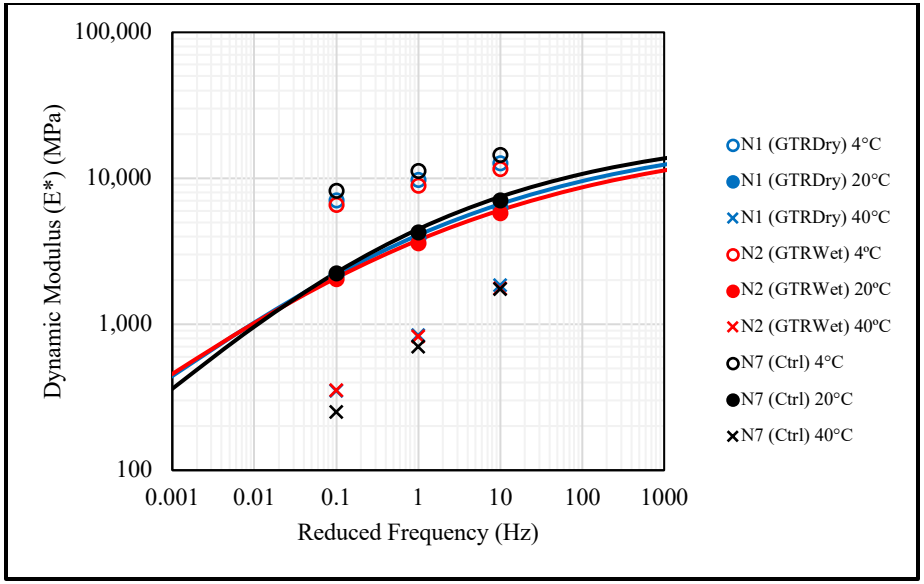

Figure 4.2.4: E Master Curves (Rubber-Modified Mixtures)*

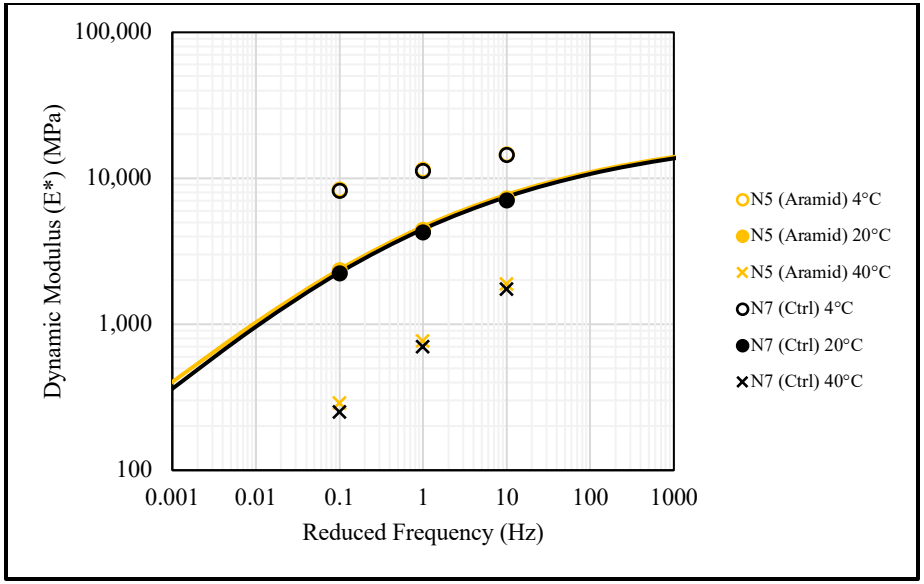

Figure 4.2.5: E Master Curves (Fiber-Modified Mixture)*

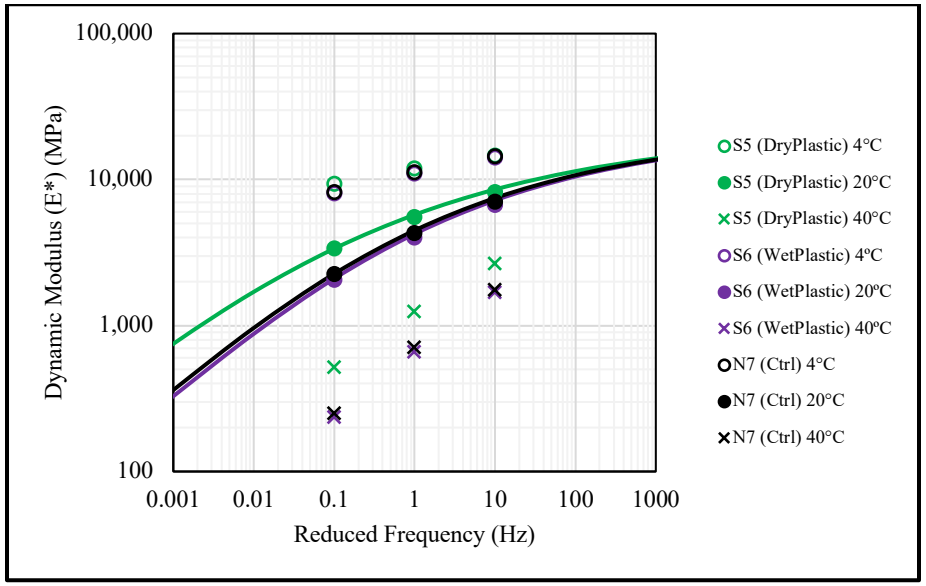

Figure 4.2.6: E Master Curves (Plastic-Modified Mixtures*

As a part of AASHTO TP 132-19, the mixture phase angle was measured at three testing temperatures (4, 20, and 40ºC) and three loading frequencies (0.1, 0, and 10Hz). The average phase angle (of three test replicates) for the AG mixtures at each testing temperature and loading frequency is shown by *Figure 4.2.7*, *Figure 4.2.8*, *Figure 4.2.9* (for 0.1, 1, and 10 Hz respectively). An ANOVA and subsequent Tukey-Kramer analysis were performed for each testing condition to identify mixtures with statistically similar average phase angles (see *Table A.2.1* and *Table A.2.2* for the phase angle ANOVA and Tukey-Kramer computations, respectively). Both statistical analyses were performed using an α of 0.05.

Phase angle master curves were developed for each AG mixture at a reference temperature of 20ºC using Master Solver for Excel© Version 2.3 in accordance with AASHTO R 84-17. *Figure 4.2.10*, *Figure 4.2.11*, and *Figure 4.2.12* display the phase angle master curves for the rubber-modified, fiber-modified, and plastic-modified mixtures, respectively. The phase angle master curve of the control mixture was included on each plot for comparison.

The rubber-modified mixtures displayed numerically lower phase angles (synonymous with increased mixture elasticity) relative to the control mixture across all loading frequencies at 20ºC and 40ºC. This is reflected by their phase angle master curves, where the average phase angle values of N1 (GTRDry) and N2 (GTRWet) are positioned lower than those of N7 (Ctrl) on the left-hand side of the chart. N2 (GTRWet) was found to have statistically lower average phase angles values relative to N7 (Ctrl) at these testing temperatures and frequencies. It should be noted that despite presenting numerically lower phase angle values, N1 (GTRDry) was still found to be statistically similar to N7 (Ctrl) at most frequencies at 20ºC and 40ºC. This could have been due to the limited number of test replicates that were able to be performed (three per mixture), which decreased the sensitivity of the ANOVA and Tukey-Kramer analysis to differences in average measured phase angle between the mixtures. Had a greater number of test replicates been able to be performed, the average measured phase angles of N1 (GTRDry) and N7 (Ctrl) at the intermediate and high testing temperatures may have been found statistically different. If it were to be assumed that N1 (GTRDry) did in fact display lower average phase angle values at 20ºC and 40ºC, then it could be concluded that both rubber-modified mixtures displayed an increased elastic response that coincided with an increase in average E* (relative to the control mixture) at approximately the same reduced frequency range (see *Figure 4.2.4* and *Figure 4.2.10*). This would be consistent with what is understood about these two material properties, which are closely linked with one another.

The fiber-modified mixture, N5 (Aramid), and the wet-process plastic-modified mixture, S6 (WetPlastic), displayed no significant difference in their average phase angles relative to the N7 (Ctrl) at any testing temperature or frequency. This is reflected by their phase angle master curves, which are both overlayed on top of the control mixture's. In general, phase angle differences are far less pronounced between asphalt mixtures (assuming they are similar in their gradations) in comparison to their individual binder components. This is because dense-graded asphalt mixtures are usually comprised of only 4-6% asphalt binder (5.6% for the AG mixtures) and differences in binder properties (such as phase angle) becomes less apparent when evaluating mixtures as a whole. Additionally, N5 (Aramid), S6 (WetPlastic), and N7 (Ctrl) all utilized the same PG 76-22

SBS-modified asphalt binder. For these reasons, the lack of any significant differences in the average phase angles of these mixtures can be explained.

In comparison to N7 (Ctrl), the average phase angles values of S5 (DryPlastic) were found to be numerically lower at all testing temperatures and frequencies, and statistically lower across all frequencies at 20ºC and 4ºC. This is reflected by the phase angle master curve of S5 (DryPlastic), which is positioned below the control mixture. Given that S5 (DryPlastic) was found to have statistically higher average E* values relative to the control mixture, it is unsurprising that it also displays a corresponding relative increase in its elastic response.

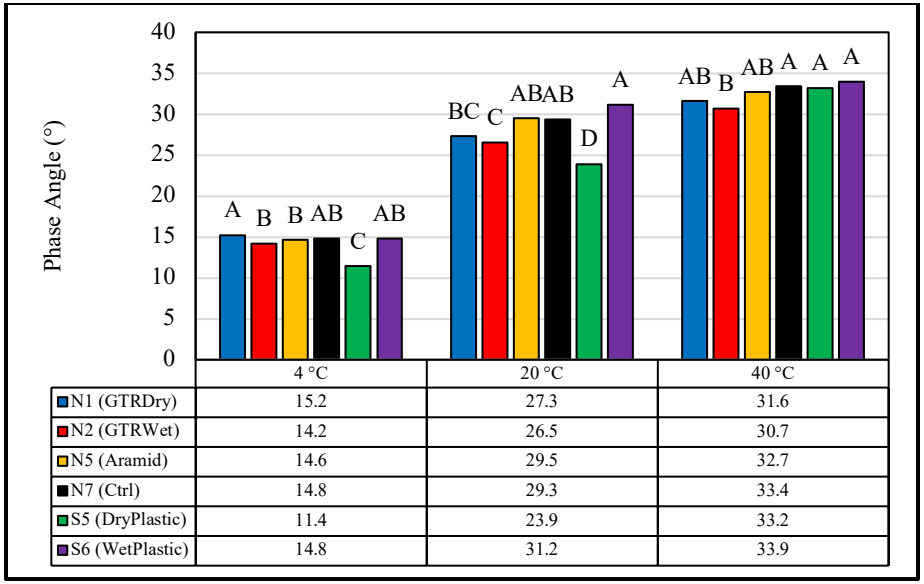

	4 °C	20 °C	40 °C
N1 (GTRDry)	15.2	27.3	31.6
N2 (GTRWet)	14.2	26.5	30.7
N5 (Aramid)	14.6	29.5	32.7
N7 (Ctrl)	14.8	29.3	33.4
S5 (DryPlastic)	11.4	23.9	33.2
S6 (WetPlastic)	14.8	31.2	33.9

Figure 4.2.7: Average Phase Angle at Each Temperature (0.1 Hz)

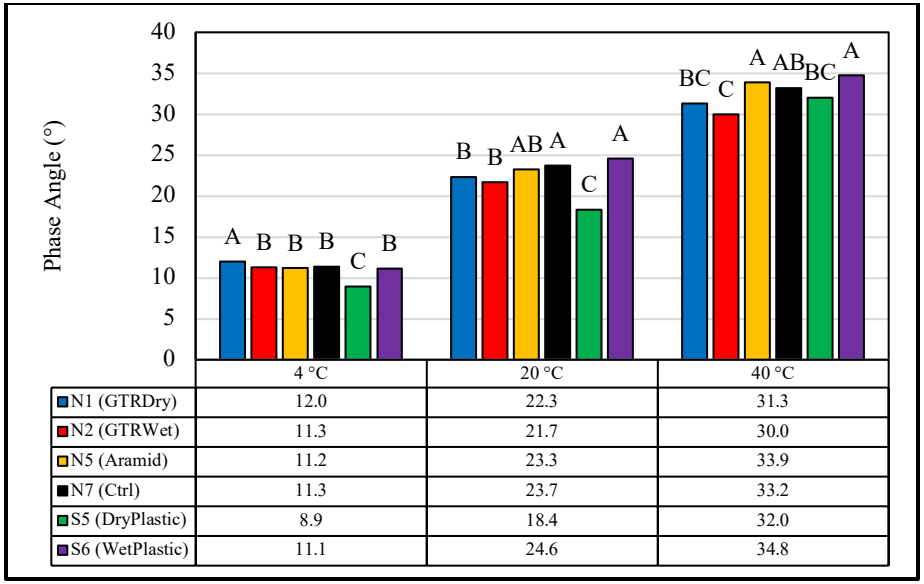

	4 °C	20 °C	40 °C
N1 (GTRDry)	12.0	22.3	31.3
N2 (GTRWet)	11.3	21.7	30.0
N5 (Aramid)	11.2	23.3	33.9
N7 (Ctrl)	11.3	23.7	33.2
S5 (DryPlastic)	8.9	18.4	32.0
S6 (WetPlastic)	11.1	24.6	34.8

Figure 4.2.8: Average Phase Angle at Each Temperature (1 Hz)

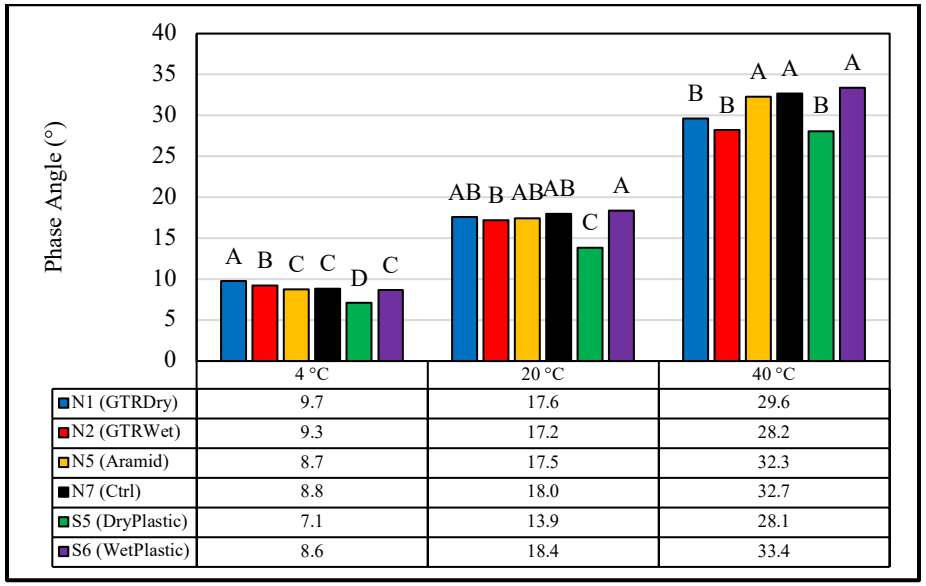

	4 °C	20 °C	40 °C
N1 (GTRDry)	9.7	17.6	29.6
N2 (GTRWet)	9.3	17.2	28.2
N5 (Aramid)	8.7	17.5	32.3
N7 (Ctrl)	8.8	18.0	32.7
S5 (DryPlastic)	7.1	13.9	28.1
S6 (WetPlastic)	8.6	18.4	33.4

Figure 4.2.9: Average Phase Angle at Each Temperature (10 Hz)

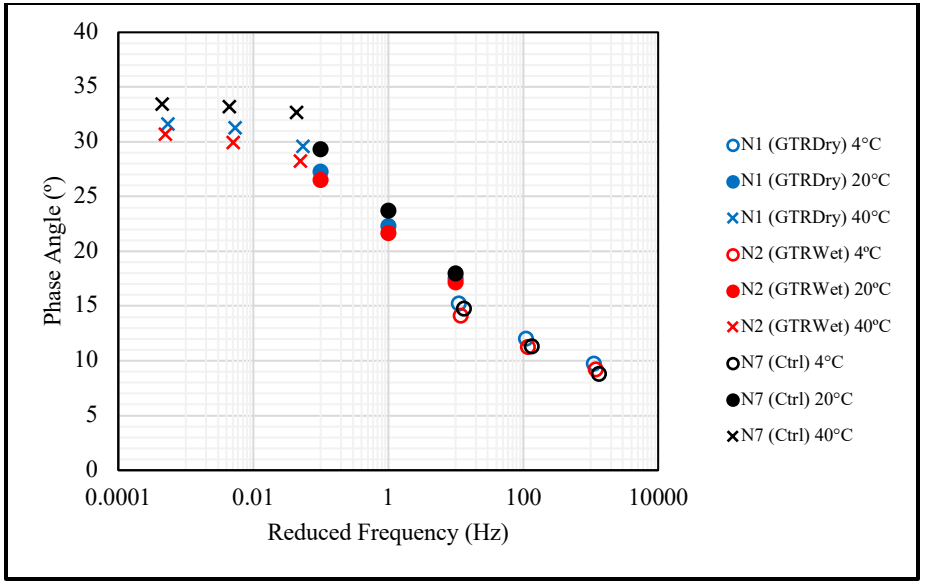

Figure 4.2.10: Phase Angle Master Curves (Rubber-Modified Mixtures)

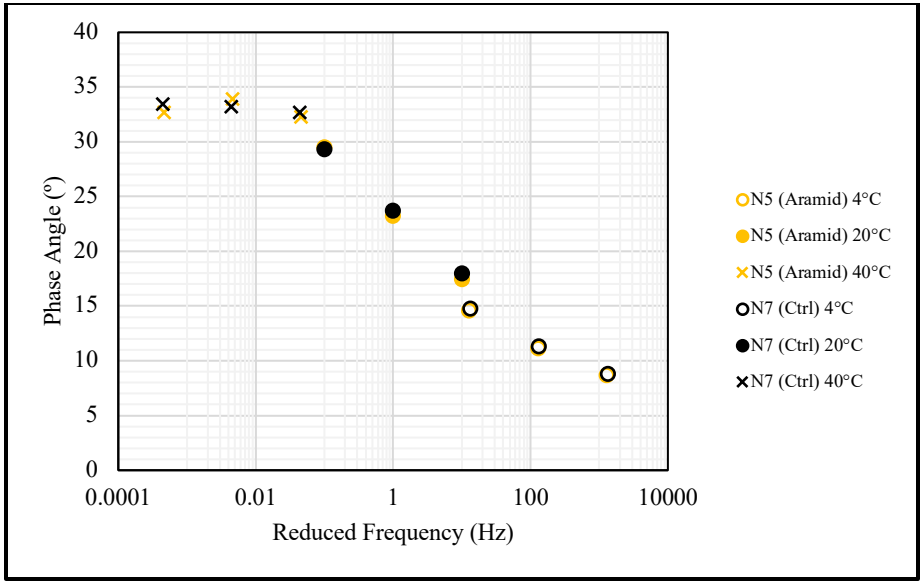

Figure 4.2.11: Phase Angle Master Curves (Fiber-Modified Mixture)

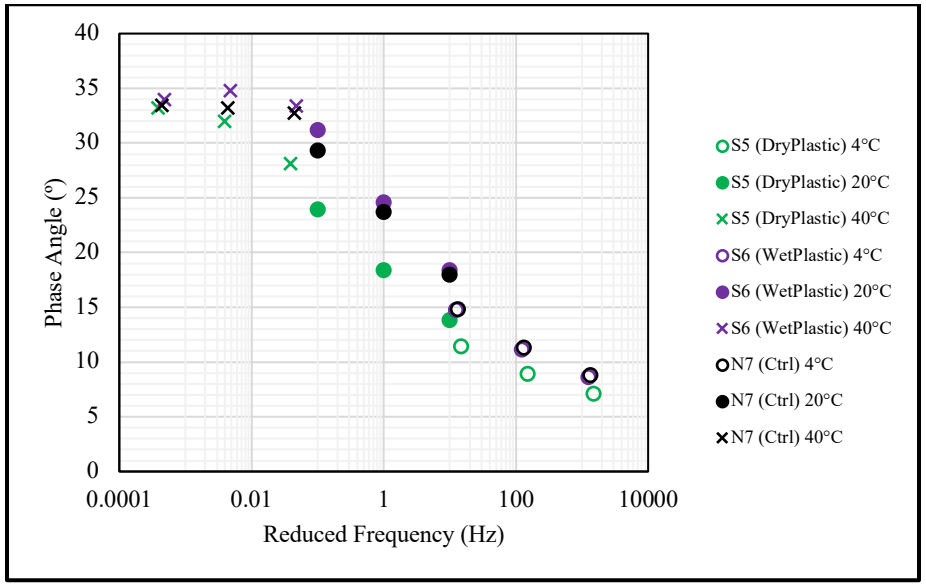

Figure 4.2.12: Phase Angle Master Curves (Plastic-Modified Mixtures

Black Space diagrams comparing the relationship between dynamic modulus (E*) and phase angle were constructed for each AG mixture. *Figure 4.2.14*, *Figure 4.2.15*, and *Figure 4.2.16* display the Black Space diagrams for the rubber-modified, fiber-modified, and plastic-modified mixtures, respectively. N7 (Ctrl) was included on each plot for comparison. Black Space diagrams offer an alternative method of analyzing the rheological properties of asphalt mixtures. In this case, the relationship between mixture stiffness (E*) and elasticity (phase angle) at an intermediate temperature (20°C) was evaluated.

The rubber-modified mixtures presented similar trends. N1 (GTRDry) and N2 (GTRWet) displayed reduced phase angles (increased elastic behavior) relative to N7 (Ctrl) at similar magnitudes of E*. This was displayed by their shift towards the lefthand side of the plot (*Figure 4.2.14*). N2 (GTRWet) displayed this behavior to a greater degree than N1 (GTRDry). N5 (Aramid) and S6 (WetPlastic) displayed very little departure from the N7 (Ctrl). Though, this result was expected as these mixtures were found to have statistically similar average E* and phase angle values at every testing temperature and loading frequency. S5 (DryPlastic) was found to have an increased E* relative to the N7 (Ctrl) at the highest phase angle values, but otherwise presented a reduced phase angle at equivalent E* magnitudes (*Figure 4.2.16*).

The Glover-Rowe parameter (G-R_m) was calculated for each AG mixture at a temperature of 20°C and a loading frequency of 5 Hz and was used to evaluate the block cracking susceptibility of each mixture (*Figure 4.2.13*). N2 (GTRWet) was found to have the highest ductility and lowest potential for block cracking, while S5 (DryPlastic) had the least amount of ductility and the highest potential for block cracking by a fairly wide margin. These results highlight the stark difference between S5 (DryPlastic) and N7 (Ctrl) (as well as the other AG mixtures) in terms of their resistance to cracking. This idea will be further explored in the following sections.

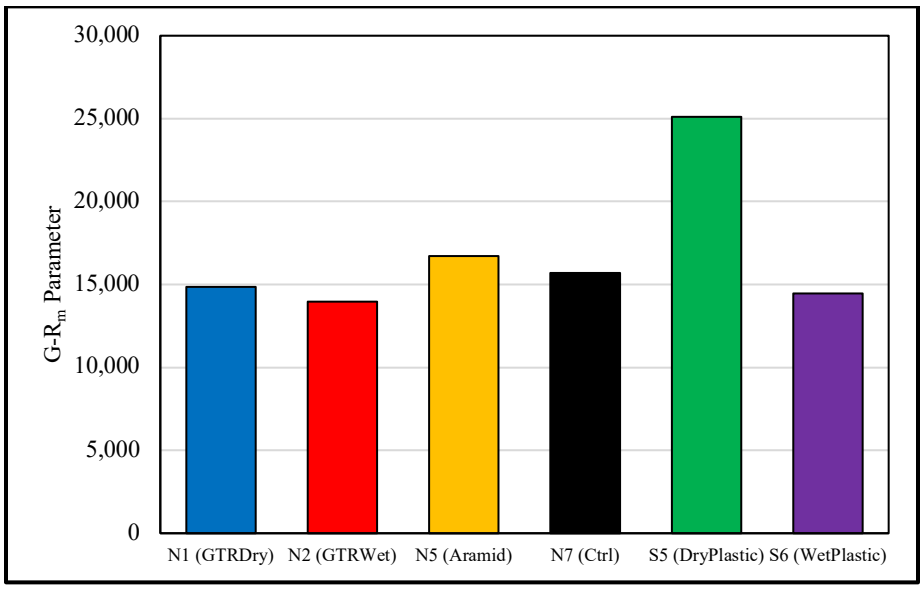

Figure 4.2.13: Glover-Rowe Parameters

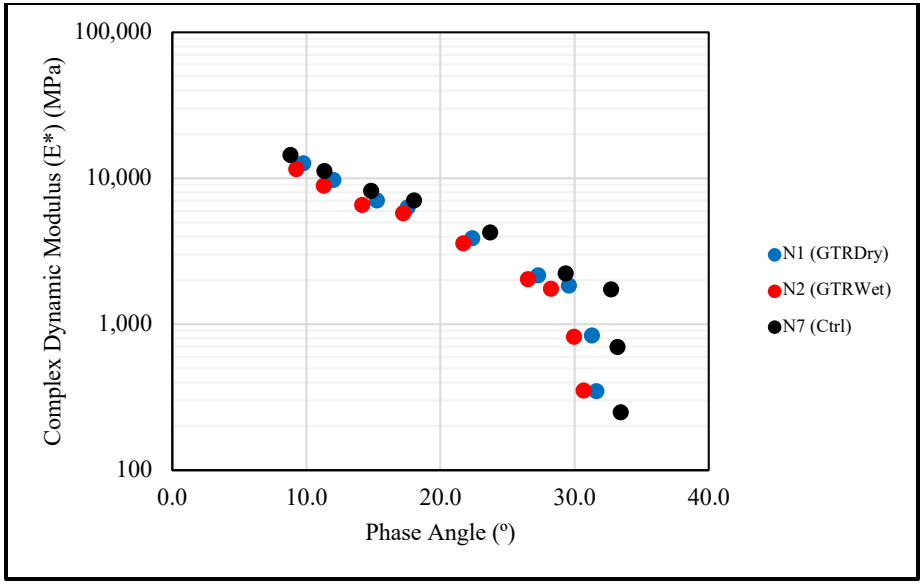

Figure 4.2.14: Black Space Diagram (Rubber-Modified Mixtures)

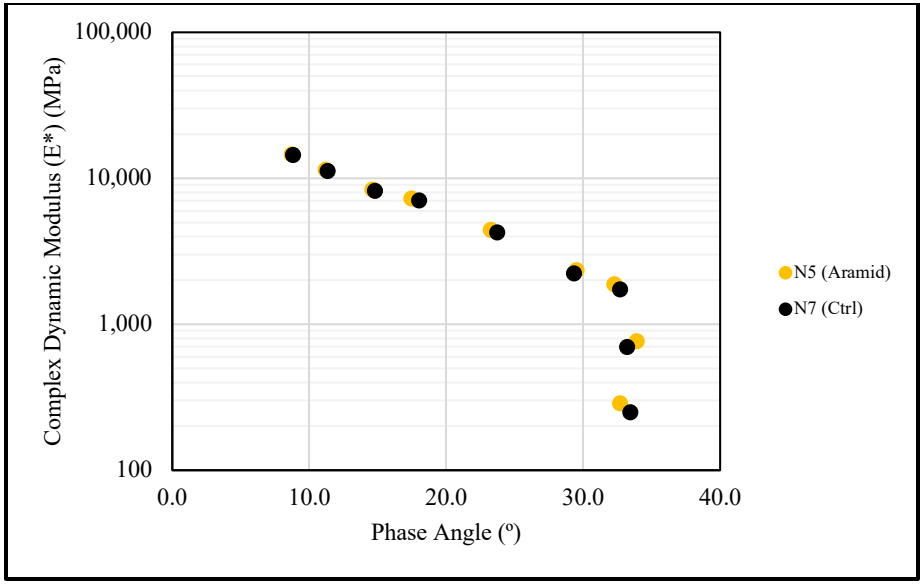

Figure 4.2.15: Black Space Diagram (Fiber-Modified Mixture)

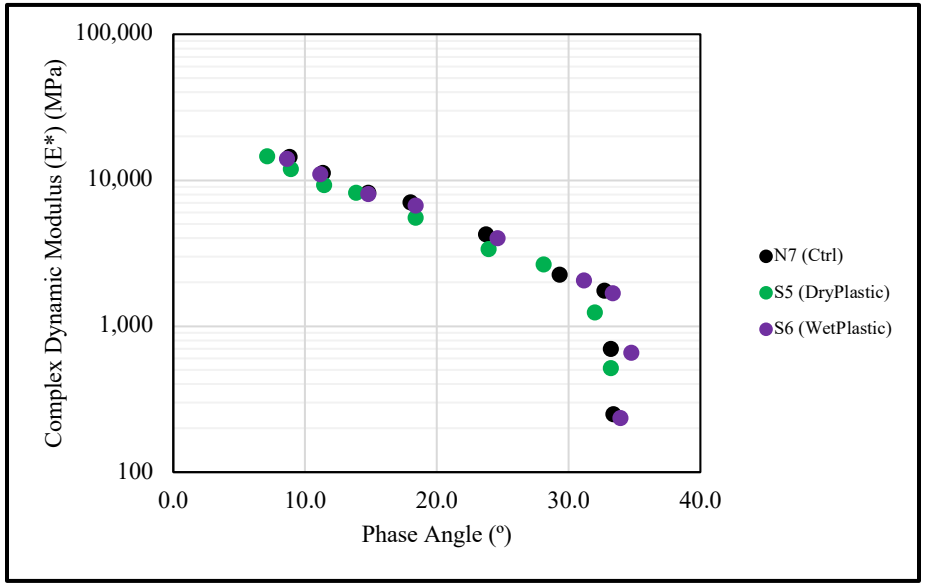

Figure 4.2.16: Black Space Diagram (Plastic-Modified Mixtures)

4.3: Direct Tension Cyclic Fatigue Test Results

The direct tension cyclic fatigue test was conducted in accordance with AASHTO TP 133-22. FlexMAT^{TM} Cracking v2.1.1 was used to perform the data processing and analysis, including the determination of damage characteristic curves and the calculation of the D^R failure criterion and S_{app} parameters for each AG mixture.

Figure 4.3.1, *Figure 4.3.2*, and *Figure 4.3.3* display the damage characteristic curves for the rubber-modified, fiber-modified, and plastic-modified mixtures, respectively. The N7 (Ctrl) damage characteristic curve was included on each plot for comparison. While the damage characteristic curves indicated potential fatigue life improvements for some of the AG mixtures (namely N1 (GTRDry) and N2 (GTRWet)), the laboratory fatigue performance evaluation was based solely upon the rankings of the computed S_{app} parameters.

When examining the damage characteristic curves of the rubber-modified mixtures, it was observed that both N1 (GTRDry) and N2 (GTRWet) displayed a greater loss of material integrity (lower value of pseudo stiffness) in comparison to the control mixture at the same level of damage. The degree of this behavior was much greater for N2 (GTRWet) in comparison to N1 (GTRDry). This behavior can be attributed to the lower E* values observed for these mixtures in comparison to N7 (Ctrl) and was consistent with the findings of previous research (Zeida et al., 2014). The same study found that the damage characteristic curves of the wet-process GTR-modified mixture and the control mixture terminated at similar values of pseudo stiffness (Zeida et al., 2014). This is in contrast to what was observed for the N1 (GTRDry) and N2 (GTRWet), where the curves of both rubber-modified mixtures terminated at a lower pseudo stiffness compared to the control mixture (a result that indicated a potential improvement in laboratory fatigue performance). The difference in these findings could have been due to any number of factors, including the differences in gradation type (gap-graded versus dense-graded), AC content, the specific crumb-rubber used, and the crumb-rubber dosage rate.

The damage characteristic curves of N5 (Aramid) and N7 (Ctrl) were very similar, though N5 (Aramid) displayed a slightly higher amount of material integrity for any given state of internal damage in comparison to N7 (Ctrl) (i.e., its damage characteristic curve was positioned more favorably). Though, such slight differences in relative curve positioning could be attributed to test variability. This result was mostly consistent with the findings of another study that investigated the fatigue performance of two aramid-modified mixtures with “good” and “poor” fiber distribution versus an unmodified control mixture (Noorvand et al., 2018). In this study, it was concluded that the resulting damage characteristic curves were similar. Though, the curves of both fiber-modified mixtures provided in the report appeared to be positioned slightly lower than the unmodified control mixture (Noorvand et al., 2018). The damage characteristic curve of N5 (Aramid) terminated at greater value of pseudo stiffness in comparison to the N7 (Ctrl), indicating the potential for a reduction in fatigue performance. This finding was in contrast to what was observed on the damage characteristic curves provided in the study mentioned previously (Noorvand et al., 2018), where the fiber-modified mixtures displayed termination points at lower values of pseudo stiffness in comparison to their unmodified control mixture. This discrepancy

could have been due to any number of factors including mixture design, fiber dosage rates, fiber dispersion, and the specific fiber technology used.

The plastic-modified mixtures, S5 (DryPlastic) and S6 (WetPlastic) displayed markedly different damage characteristic curves. S5 (DryPlastic) had higher values of pseudo stiffness at any and given value of damage with respect to N7 (Ctrl), while the opposite was observed for S6 (WetPlastic). Previous research has shown the polymer-modification, including SBS-modification, results in a vertical shift of damage characteristic curves due to an increase in mixture stiffness (Queiroz et al., 2023 and Spadoni et al., 2022). The degree of this effect is largely due to the specific polymer formulation utilized, the modification technique/process, and the dosage rate. Additionally, the increased E* of S5 (DryPlastic) indicated a significant stiffening effect due to the mixture receiving both wet-process and dry-process polymer modification. Knowing all of this, the positioning of the of the S5 (DryPlastic) damage characteristic curve relative to S6 (WetPlastic) and N7 (Ctrl) can be justified.

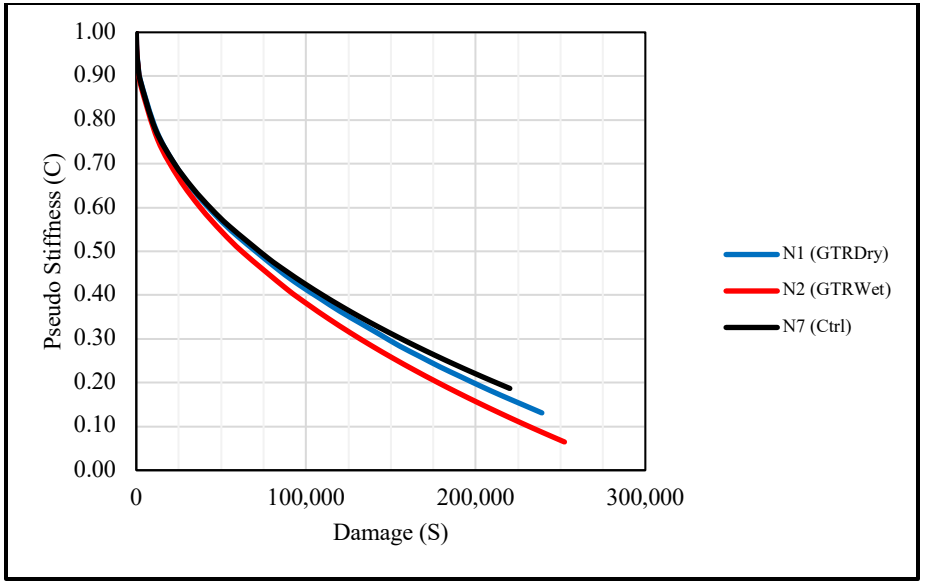

Figure 4.3.1: Damage Characteristic Curves (Rubber-Modified Mixtures)

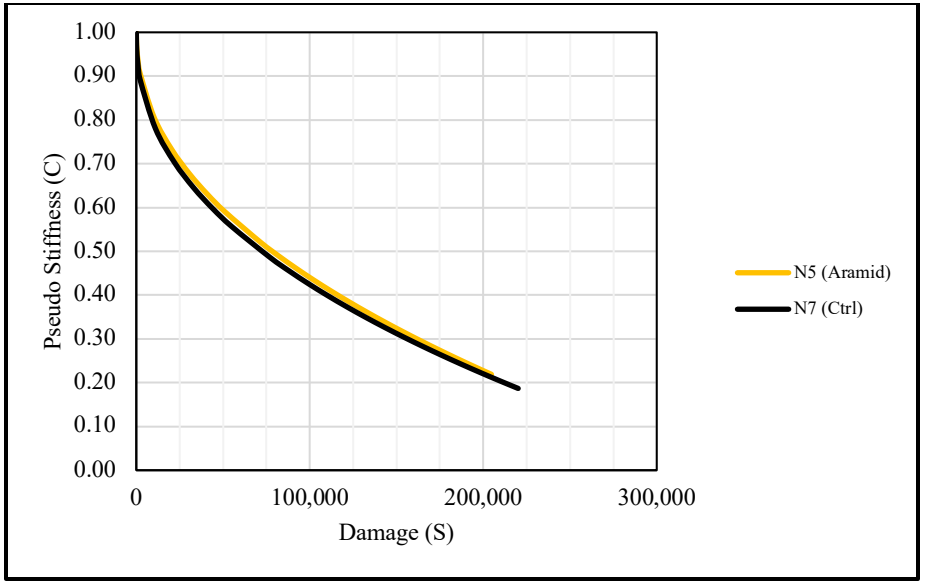

Figure 4.3.2: Damage Characteristic Curves (Fiber-Modified Mixture)

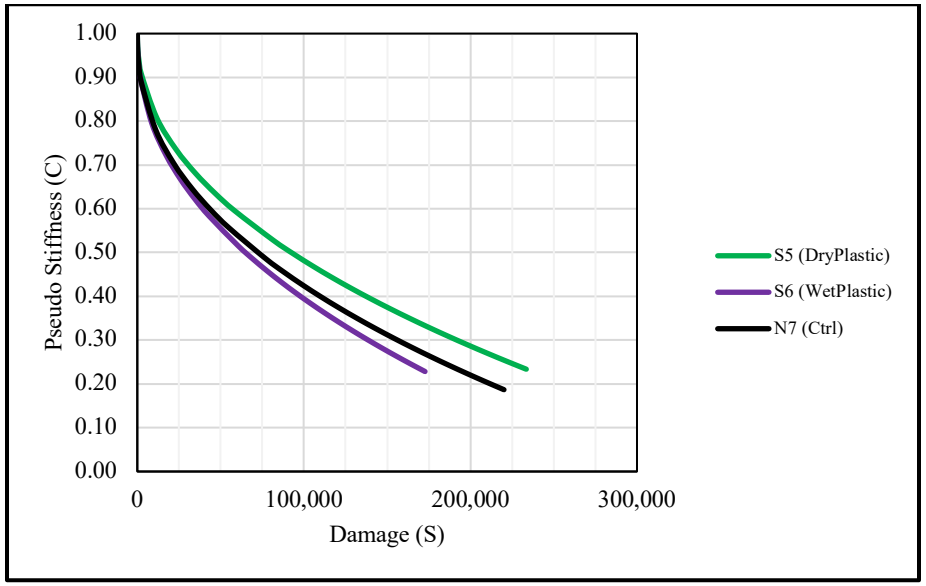

Figure 4.3.3: Damage Characteristic Curves (Plastic-Modified Mixtures)

Figure 4.3.4, *Figure 4.3.5*, and *Figure 4.3.6* display the linear relationship between cumulative pseudo stiffness and number of cycles to failure (the slope of which corresponds to the D^R failure criterion) for the rubber-modified mixtures, aramid-modified mixture, and plastic-modified mixtures, respectively. *Figure 4.3.7* displays the D^R failure criterion and the computed S_{app} parameters values for each AG mixture relative to one another.

The AG mixtures were ranked according to their laboratory fatigue performance from greatest to least (*Figure 4.3.7*). Additionally, the fatigue life transfer functions of each mixture resulting from beam fatigue testing (*Figure 4.4.3*, *Figure 4.4.4*, and *Figure 4.4.5*) were compared to the rankings of S_{app}. N2 (GTRWet) displayed the highest D^R failure criterion (greatest amount of material toughness) and highest S_{app} parameter (greatest laboratory fatigue performance) amongst all of the AG mixtures, followed by N1 (GTRDry). N2 (GTRWet) was also found to have significantly higher strain tolerance in beam fatigue testing, confirming it had improved laboratory fatigue resistance over N7 (Ctrl) and the other AG mixtures. N7 (Ctrl) fell within the middle of the pack, both in terms of its D^R failure criterion as well as its S_{app} parameter, followed closely by N5 (Aramid) and S6 (WetPlastic). This result made sense given that these mixtures were found to have statistically similar average E* values, phase angles, and fatigue life transfer functions. S5 (DryPlastic) displayed the lowest D^R failure criterion and the lowest S_{app} parameter, indicating it had the least amount of material toughness and worst laboratory fatigue performance. Previous research findings have shown that SBS-modification results in higher D^R failure criterion and S_{app} parameters versus other polymer-modification technologies (Queiroz et al., 2023 and Spadoni et al., 2022). This is consistent with the S_{app} rankings of N7 (Ctrl), S5 (DryPlastic), and S6 (WetPlastic).

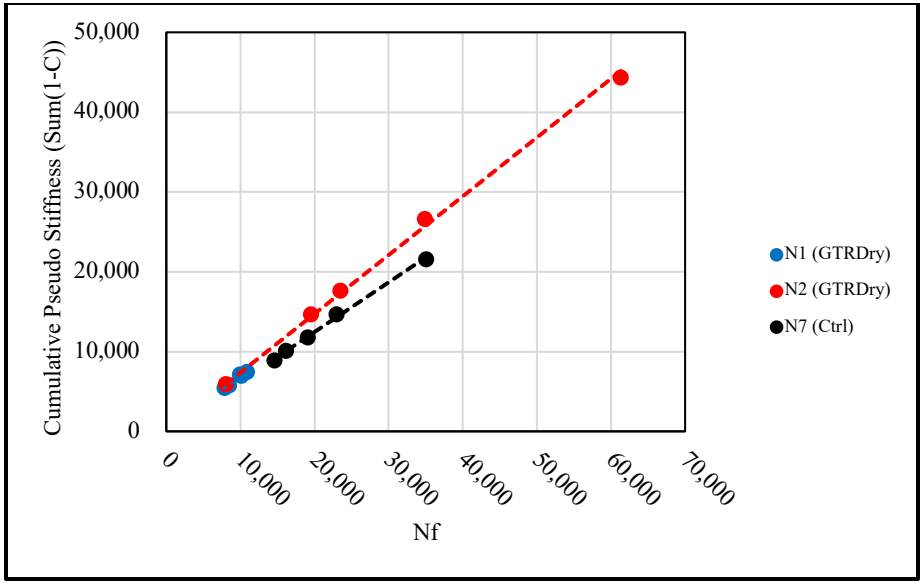

Figure 4.3.4: D^R Failure Criterion Plots (Rubber-Modified Mixtures)

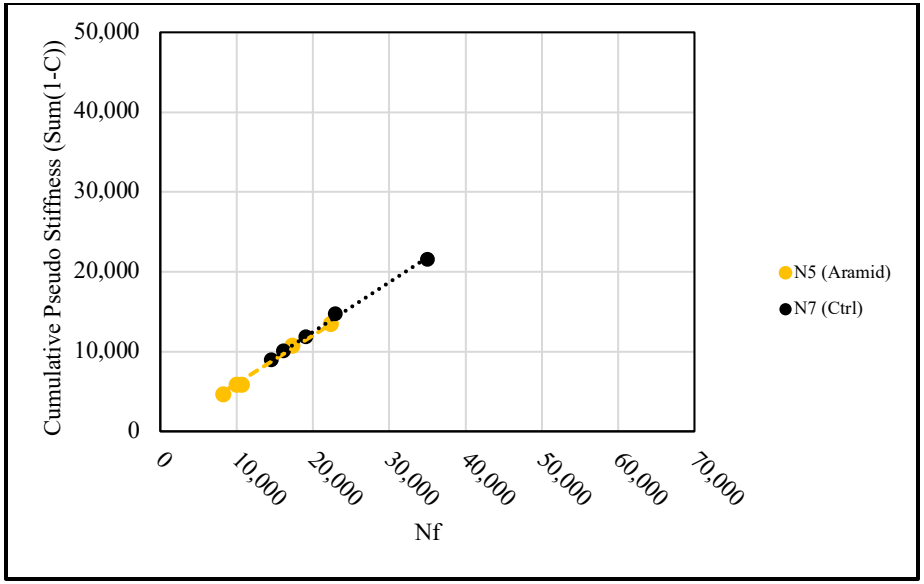

Figure 4.3.5: D^R Failure Criterion Plots (Fiber-Modified Mixture)

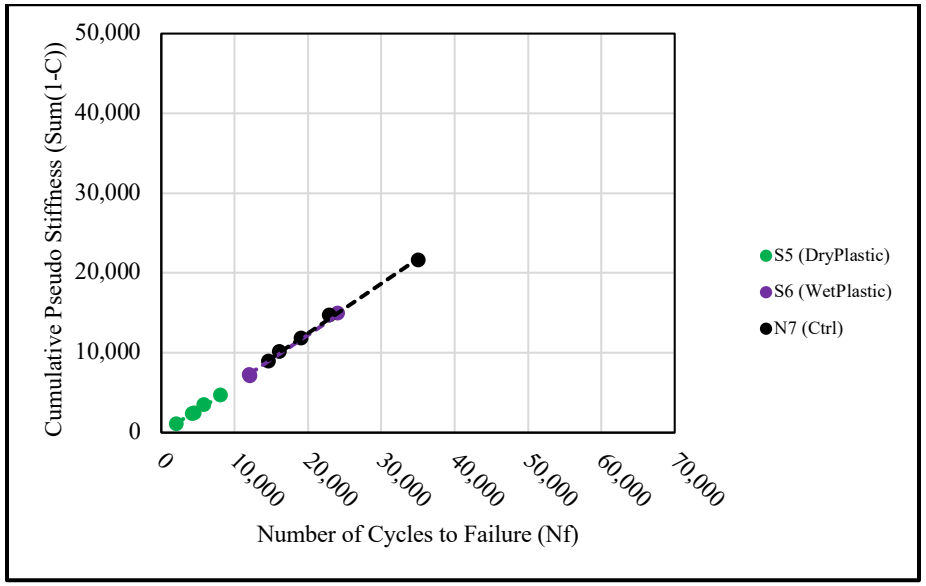

Figure 4.3.6: D^R Failure Criterion Plots (Plastic-Modified Mixtures

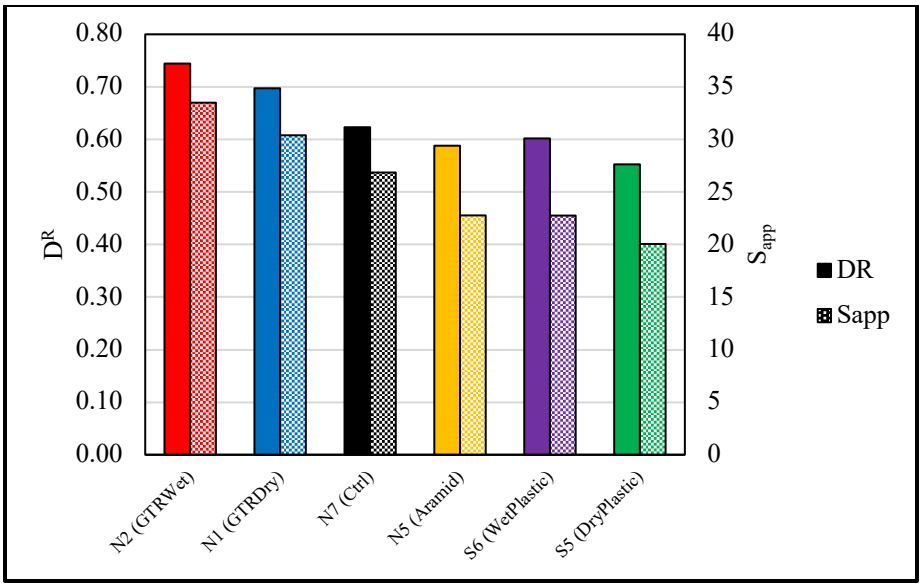

Figure 4.3.7: D^R Failure Criterion and S_{app} Parameters

4.4: Bending Beam Fatigue Test Results

Bending beam fatigue testing was conducted in accordance with AASHTO T321-22 to evaluate the initial flexural stiffness and fatigue life of each AG mixture in a cyclic, tensile loading mode. *Figure 4.4.1* displays the initial flexural stiffness results, evaluated at the 50th loading cycle, for each mixture. An ANOVA and subsequent Tukey-Kramer analysis were performed in order to identify which AG mixtures had statically similar average values of initial flexural stiffness (see *Table A.3.1* and *Table A.3.2* for initial flexural stiffness ANOVA and Tukey-Kramer computations, respectively). Both statistical analyses were performed using an α of 0.05. The rubber-modified mixtures displayed the lowest values of initial flexural stiffness, with N2 (GTRWet) displaying the lowest overall. As discussed previously, it would be incorrect to conclude that the rubber-modification produced a softening effect. Rather, the modification of the other AG mixtures increased their flexural stiffness by a greater amount. N7 (Ctrl), N5 (Aramid), and S6 (WetPlastic) all displayed statistically similar values of initial flexural stiffness. This result makes sense, especially for N7 (Ctrl) and N5 (Aramid) given that the only differentiation between those two mixtures is the fiber modification, a technology which previous research has identified as often not producing noticeable increases in stiffness within the laboratory setting. The similarity of S6 (WetPlastic) and N7 (Ctrl) may also be attributed to the fact that both utilize a PG 76-22 binder, modified with a wet-process polymer product. S5 (DryPlastic) was found to have the greatest initial flexural stiffness. This can be attributed to the fact that it utilized SBS-modified asphalt binder whilst also adding a dry-process rPE additive, which are known to increase mixture stiffness, as demonstrated by a previous study (Abdalfattah et al., 2022). *Figure 4.4.2* displays the average E* versus the average initial flexural stiffness, each evaluated at a 10 Hz loading frequency and 20ºC testing temperature. A strong linear correlation was found between the results of the two

laboratory tests despite the differences in strain modes (axial versus flexural). This observation also provided additional validity to the respective modulus/stiffness findings of the two tests.

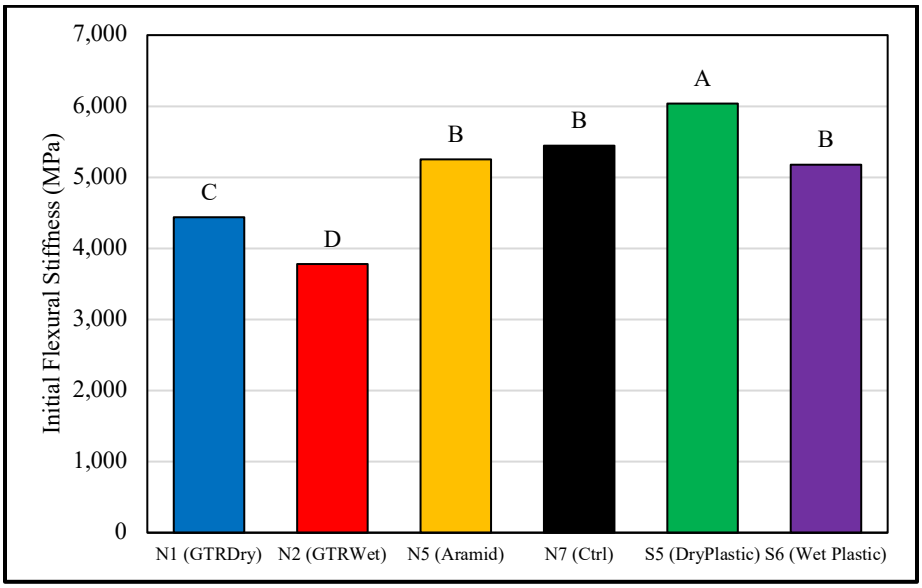

Figure 4.4.1: Average Initial Flexural Stiffness

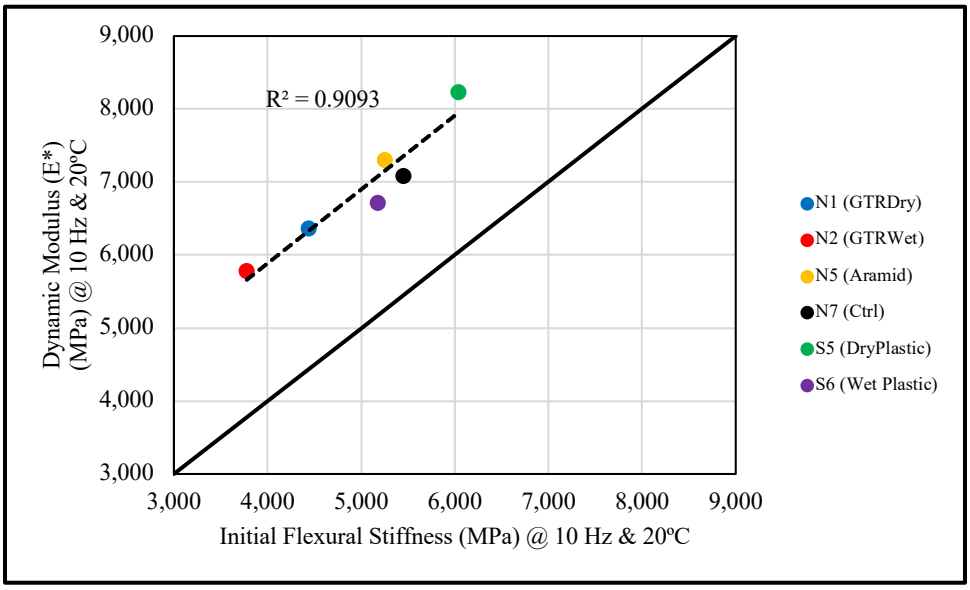

Figure 4.4.2: Average E versus Average Initial Flexural Stiffness @ 10 Hz and 20ºC*

The fatigue life of each AG mixture was evaluated via AASHTO T 321-22. Three test replicates were conducted at the low, intermediate, and high strain levels, with each replicate utilizing a unique test specimen. Transfer functions describing the relationship between applied strain and

number of cycles to failure (N_f) were developed for each mixture. *Figure 4.4.2*, *Figure 4.4.3*, and *Figure 4.4.5* display N_f versus strain data for the rubber-modified mixtures, aramid-modified mixture, and plastic-modified mixtures, respectively. Also shown are the fitted power regression functions for each mixture (the coefficients of which are given by *Table 4.4.1*, each in the form of *Equation 3.8.4*). *Figure 4.4.6* presents the average N_f at each strain level for all AG mixtures. An ANOVA and subsequent Tukey-Kramer analysis were performed (using an α of 0.05) in order to identify which mixtures had statistically similar average N_f values at each strain level (see *Table A.4.1* and *Table A.4.2* for average N_f ANOVA and Tukey-Kramer computations, respectively). It should be noted that N2 (GTRWet) was not tested at 400 με because the number of cycles far exceeded the practical limit for testing defined by AASHTO T 321-22.

N2 (GTRWet) was the only mixture to display statistically different average N_f values relative to N7 (Ctrl). *Figure 4.4.6* shows that at 600 με and 800 με, N_f values of N2 (GTRWet) were nearly a full magnitude higher than N7 (Ctrl), or any other AG mixture. This is clearly demonstrated by the transfer function of N2 (GTRWet), that displays its significantly increased strain-tolerance. This result is consistent with previous research that demonstrated that wet-process GTR modification can lend significant amounts of strain tolerance to a mixture, increasing its fatigue life at any strain level (Feiteira Dias et al., 2014). Dry-process GTR modification was also demonstrated to significantly improve mixture fatigue life, though to a lesser degree (Feiteira Dias et al., 2014). However, this effect was not observed for N1 (GTRDry). N1 (GTRDry), N5 (Aramid), and S6 (WetPlastic) did not display any significant difference in their average N_f relative to N7 (Ctrl) at any strain level. This is reflected by the transfer functions of each mixture, which are overlayed on top of the control mixture. S5 (DryPlastic) was also found to have statistically similar average N_f values relative to the N7 (Ctrl) and the other AG mixtures (excluding N2 (GTRWet)). However, its fatigue life transfer function was numerically lower at the 600 με and 800 με levels. It is important to note that because of the high variability inherent to laboratory beam fatigue testing, and a practical limit of three test replicates at each strain level, the nuanced material differences brought about by the different additives in this experiment may not have been represented though a pure statistical analysis of averages. If it were to be assumed that the N_f values of S5 (DryPlastic) were in fact lower at 600 με and 800 με, this behavior would be consistent with what is commonly understood about the effects of dry-process plastic additives. This additive type is known to cause a stiffening of the asphalt mixture and often a subsequent decrease in fatigue life (Abdalfattah et al., 2022 and Zhang et al., 2020).

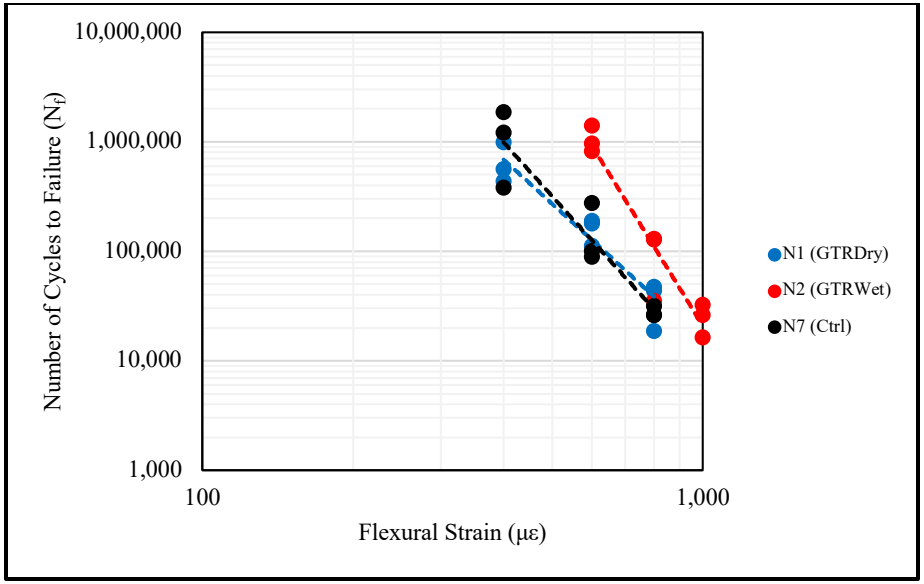

Figure 4.4.3: Transfer Functions (Rubber-Modified Mixtures)

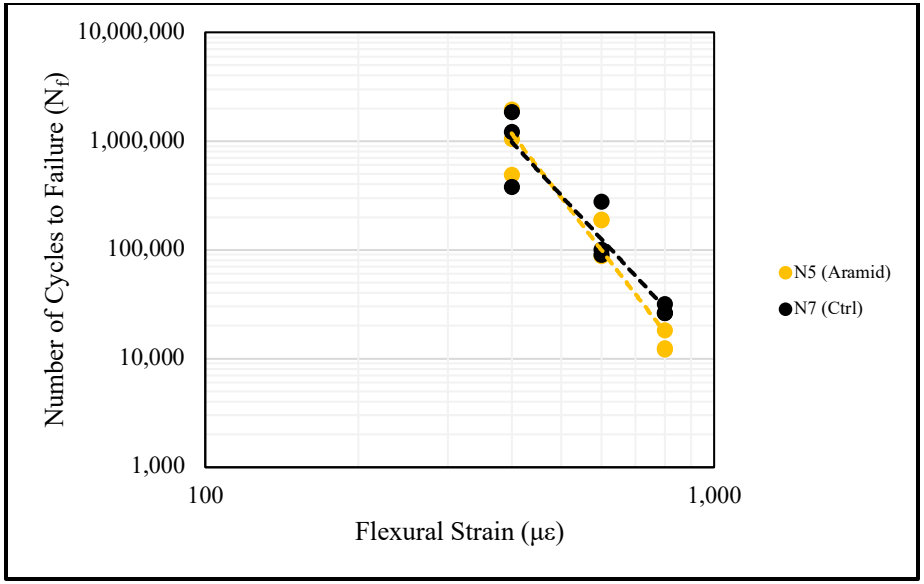

Figure 4.4.4: Transfer Functions (Fiber-Modified Mixture)

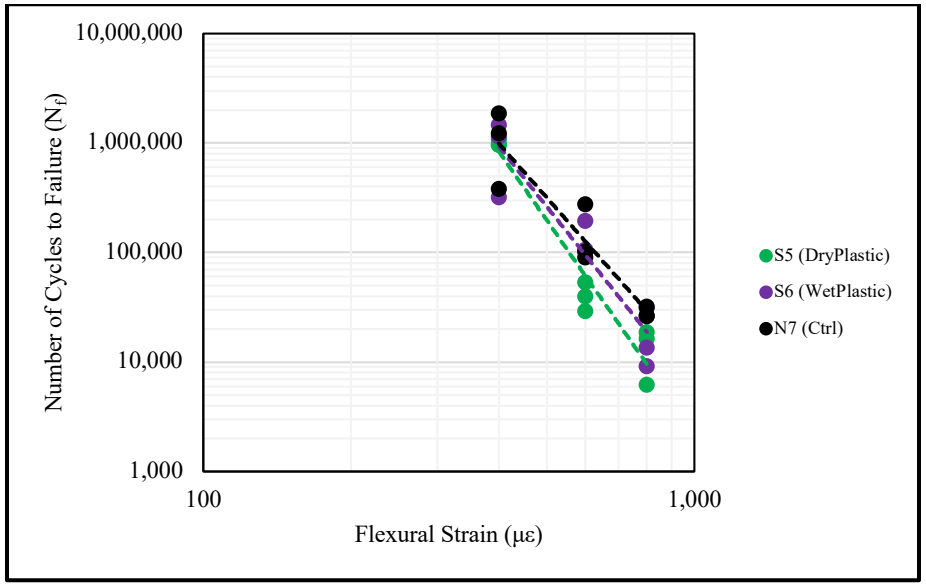

Figure 4.4.5: Transfer Functions (Plastic-Modified Mixtures)

Table 4.4.1: BBFT Transfer Function Coefficients

Mix ID	k_1	k_2	R^2
N1 (GTRDry)	4.51E+16	-4.16	0.79
N2 (GTRWet)	3.96E+26	-7.43	0.91
N5 (Aramid)	7.62E+21	-6.08	0.67
N7 (Ctrl)	1.54E+19	-5.07	0.67
S5 (DryPlastic)	4.90E+22	-6.44	0.99
S6 (Wet Plastic)	3.95E+20	-5.62	0.70

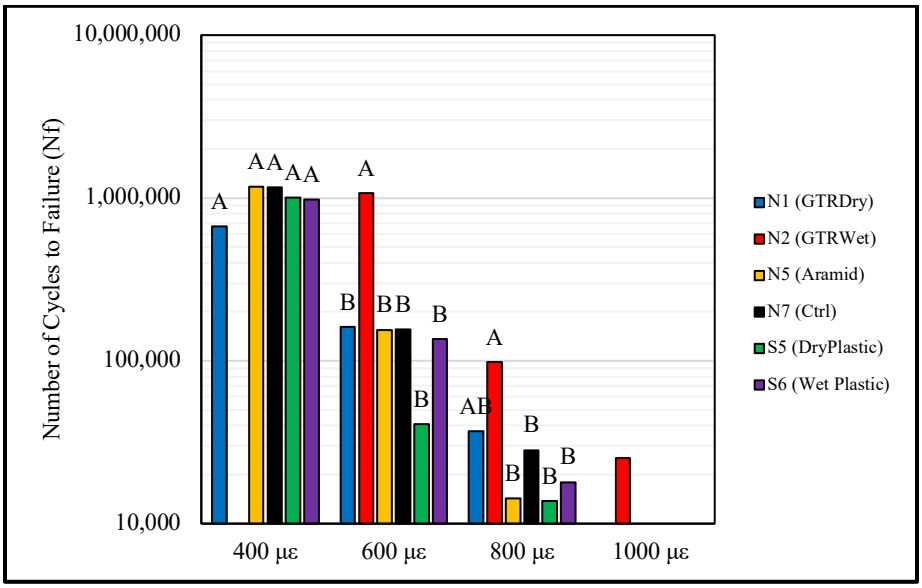

Figure 4.4.6: Average N_f versus Strain

4.5: Findings and Conclusions

This chapter presented the results of three tests that were conducted to comprehensively characterize the material properties and laboratory performance of the AG asphalt mixtures. These tests included the dynamic modulus (E*) test, the direct tension cyclic fatigue test, and the bending beam fatigue test. A multitude of conclusions were able to be drawn based upon the laboratory results presented in this chapter.

N1 (GTRDry) and N2 (GTRWet) were found to have decreased average E* values at low and intermediate temperatures relative to the control mixture (*Figure 4.2.1* and *Figure 4.2.4*). The wet-process mixture displayed this behavior to a greater degree than the dry-process mixture. S5 (DryPlastic) had significantly increased average E* values relative to N7 (Ctrl), especially at intermediate and high temperatures (*Figure 4.2.3* and *Figure 4.2.6*). The average E* values of all other AG mixtures were found to be significantly similar to the control mixture. Additionally, E* at 20°C and 10 Hz showed great agreement with the initial flexural stiffness (via beam fatigue testing) measured at the same temperature and frequency (*Figure 4.4.3*).

The damage characteristic curve of N2 (GTRWet) was positioned below that of N7 (Ctrl), likely due to its significantly lower E* and initial flexural stiffness (*Figure 4.3.1*). The opposite was observed for S5 (DryPlastic), as its damage characteristic curve was positioned above that of N7 (Ctrl) likely due to its significantly higher E* and initial flexural stiffness (*Figure 4.3.3*) The damage characteristic curves of the other AG mixtures were found to be much more in line with that of N7 (Ctrl). N2 (GTRWet) had the highest D^R failure criterion and S_{app} parameter, indicating that it had the highest amount of material toughness and the highest laboratory fatigue resistance, and was followed by N1 (GTRDry) (*Figure 4.3.7*). Conversely, S5 (DryPlastic) had the lowest D^R failure criterion and S_{app} parameter, indicating that it had the least amount of material toughness and the least amount of fatigue resistance. These findings showed good agreement with the results of beam fatigue testing, where N2 (GTRWet) displayed significantly higher fatigue life than any other AG mixture and S5 (DryPlastic) displayed the lowest overall fatigue life (*Figure 4.4.3* and *Figure 4.3.5*). N1 (GTRDry) had an increased S_{app} relative to the control mixture, however, their fatigue life transfer functions were found to be statistically similar. This indicated a slight level of disagreement between the cyclic fatigue and beam fatigue test results. All other AG mixtures fell in between N2 (GTRWet) and S5 (DryPlastic) in terms of their computed S_{app} parameters and fatigue life transfer functions, a finding that further confirmed good overall agreement between the results of the direct tension cyclic fatigue test and the bending beam fatigue test (excluding N1 (GTRDry)) regarding the laboratory fatigue performance of mixtures modified with different additives.

The next chapter will provide a detailed insight into the construction, instrumentation, data collection, and data processing of the AG sections at the NCAT Test Tack and will include as the as-built properties of each test section.

CHAPTER 5

Field Testing – Materials and Methods

5.1: Introduction

The full-scale field evaluation involved the construction of 200 ft test sections for each AG mixture at the NCAT Test Track. Heavy vehicle trafficking provided accelerated damage to the AG test sections at rate of approximately 5 million ESALs per year. Performance data was recorded for each test section, including cracking percentage, rutting depth, and ride quality (measured as IRI (International Roughness Index)) on a weekly basis. Falling weight deflectometer (FWD) testing was performed several times per month to monitor the in-situ moduli of the subgrade, subbase, and AC layers. Finally, gauges were installed at the bottom of the AC layer to measure tensile strain under loading. All forms of field performance monitoring were performed throughout the entire trafficking period.

5.2: Thick-lift Paving

Thick-lift paving was utilized for the AG sections to mitigate the risks of debonding failure between pavement lifts. This paving method also promoted the desired failure mode of bottom-up fatigue cracking. However, the thick-lift paving introduced ride quality issues for the newly paved test sections. To solve this, the surface of each test section was precision ground to establish an acceptable initial ride quality. *Figure 5.2.1* provides an example of the surface of one of the AG test sections after precision grinding (Foshee, 2022). *Table 5.2.1* provides the pre- and post-precision grinding IRI for each section. Though not all sections were able to achieve the same post-grind initial ride quality, significant improvements were made for each.

Figure 5.2.1: Example AG Test Section After Precision Grinding (Foshee, 2022)

Table 5.2.1: Average IRI Before and After Precision Grinding (Foshee, 2022)

Test Section ID	IRI (in/mi)	
	Pre-Grind	Post-Grind
N1 (GTRDry)	175.96	72.96
N2 (GTRWet)	179.72	82.83
N5 (Aramid)	214.42	155.80
N7 (Ctrl)	238.18	125.00
S5 (DryPlastic)	178.88	96.74
S6 (WetPlastic)	152.03	79.61

5.3: As-Built Test-Section Properties

While the construction targets for AC layer thickness and in-place density were identical for all AG sections, variability between the sections was expected due to the inherent engineering control limitations associated with paving full-scale test sections. *Figure 5.3.1* provides a schematic comparing the average as-built layer thicknesses for each AG test section after surface grinding was completed. The target AC layer thickness for the AG test sections was 5.50 in. *Table 5.3.1* provides the average in-place density measurements for each AG test section (Foshee, 2022). Notably, section N7 (Ctrl) had a higher average in-place density relative to the other test sections. The effect this may have had on the performance monitoring results, as well as strain measurements, and backcalculated AC modulus will be discussed in the following chapter. Further details regarding the construction of the AG sections, and their as-built properties have been previously published (Foshee, 2022).

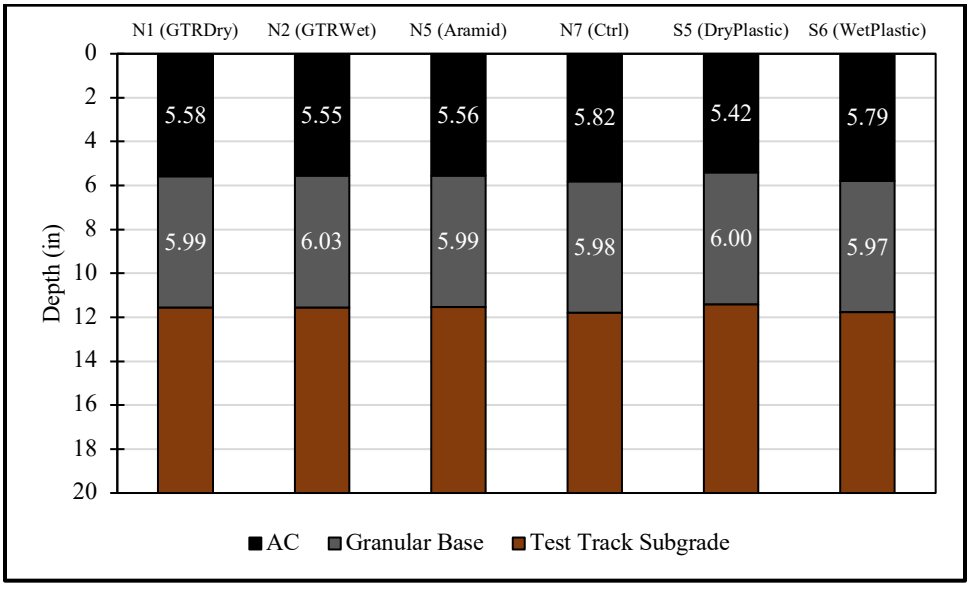

Figure 5.3.1: Average As-Built Test Section Layer Thicknesses

Table 5.3.1: Average In-Place Density

Test Section ID	Average In-Place Density (% of G_{mm})
N1 (GTRDry)	93.7%
N2 (GTRWet)	94.1%
N5 (Aramid)	94.2%
N7 (Ctrl)	95.9%
S5 (DryPlastic)	93.5%
S6 (WetPlastic)	93.9%

5.4: Trafficking

Heavy weight vehicles are used at the NCAT Test Tack to apply accelerated damage to the test sections. Triple tractor trailers travel around the Test Track at approximately 45 mph. Depending on the specific truck, the steer axle weighs between 9,900 and 13,500 lbs, the tandem axles weigh between 19,750 and 22,050 lbs, and the single axles (of which there are five per truck) weigh between 17,600 and 22,400 lbs each. The fleet of five heavy weight vehicles apply approximately 10 million ESALs within a two-year trafficking period. *Figure 5.4.1* shows one of the heavy weight vehicles used at the Test Track (Foshee, 2022).

Figure 5.4.1: NCAT Heavy Weight Vehicle (Foshee, 2022)

5.5: Performance Monitoring

Early signs of cracking within the AG test sections (not visible to automated crack detection systems) were monitored via manual inspections on a bi-weekly basis. Additionally, a Pathways data collection van recorded cracking percentage, rutting depth, and ride quality on a weekly basis. Falling weight deflectometer (FWD) testing was performed at 4 longitudinal stations within each AG test section. At each station, testing was done in the inside and outside wheelpaths, as well as between the wheelpaths. In total, 12 FWD locations were tested within each AG test section several times per month. From the FWD test data AC, granular base, and subgrade moduli were

backcalculated (E_{AC}, E_{GB}, $E_{Subgrade}$, respectively) using EVERCALC 5.0. Manual cracking inspections, digital measurements of cracking, rut depth and IRI measurements, and FWD testing will be continued throughout the entire trafficking period (approximately 10 million ESALs). Further details regarding the performance monitoring of the AG test sections, as well as the FWD backcalculation process, have been previously published (Foshee, 2022).

5.6 FWD Backcalculation and Moduli Temperature Normalization

The backcalculation of the in-situ AC, granular base, and subgrade moduli was performed using EVERCALC 5.0. This software utilizes a trial-and-error method to estimate the individual layer moduli within a layered elastic mechanistic framework. Using this method, the root mean square error (RMSE) between the predicted and measured deflection basins is minimized. Further details regarding the backcalculation methods used for the Additive Group, as well as other sections at the Test Track, have been published (Foshee, 2022).

Unlike the granular base modulus (E_{GB}) and subgrade modulus ($E_{Subgrade}$), AC modulus (E_{AC}) is prone to significant temperature effects. As pavement temperature increases, AC modulus decreases, while the opposite is true if pavement temperature decreases. Pavements are subject to daily (i.e., morning, noon, afternoon) and seasonal (i.e., Summer versus Winter) temperature variations. In order to accurately characterize AC modulus, independent of pavement temperature effects, temperature normalization must be performed. *Equation 5.6.1* displays the exponential relationship between AC modulus and mid-depth pavement temperature. *Equation 5.6.2* provides the temperature normalization relationship. The AC modulus was normalized to a temperature of 68°F (equivalent to the temperature used for dynamic modulus (E*), direct tension cyclic fatigue, and bending beam fatigue testing in the laboratory). The mid-depth pavement temperature was recorded via the thermocouple temperature probe installed in each AG test section. *Figure 5.6.1* displays backcalculated AC moduli for section N7 (Ctrl) versus mid-depth pavement temperature and illustrates the relationship provided by *Equation 5.6.1*. *Figure 5.6.2* and *Figure 5.6.3* provide the backcalculated AC moduli for section N7 (Ctrl) versus the date at which the data were collected (and the trafficking level in ESALs). The vertical E_{AC} and E_{68} variation on each chart was due to differences in the backcalculated moduli magnitude caused by testing in multiple locations within each test section, as well as the innate variation/error associated to backcalculation process. Additionally, *Figure 5.6.2* and *Figure 5.6.3* illustrate the effectiveness of the temperature normalization process. Further details regarding the FWD backcalculation process have been previously published (Foshee, 2022).

$$E_{AC} = k_1 e^{k_2 T} \qquad \textit{Equation 5.6.1}$$

Where:

E_{AC} = backcalculated AC modulus, ksi
k_1 = fitting coefficient

k_2 = fitting coefficient
T = mid-depth pavement temperature, °F

$$E_{68} = E_{AC} e^{k_2(68-T)} \qquad \textit{Equation 5.6.2}$$

Where:

E_{68} = temperature-normalized backcalculated AC modulus, ksi
E_{AC} = backcalculated AC modulus, ksi
k_2 = fitting coefficient
T = mid-depth pavement temperature, °F

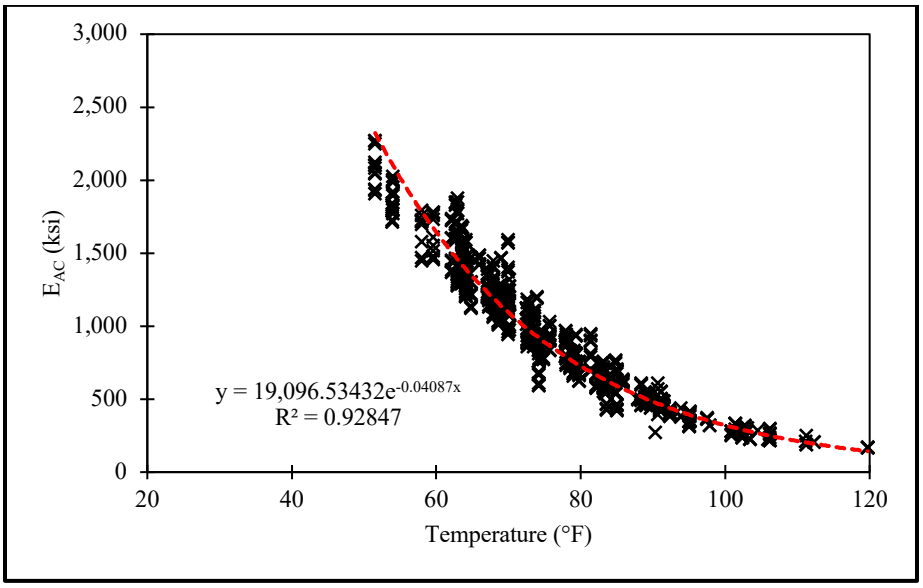

Figure 5.6.1: E_{AC} versus Mid-Depth Pavement Temperature for N7 (Ctrl)

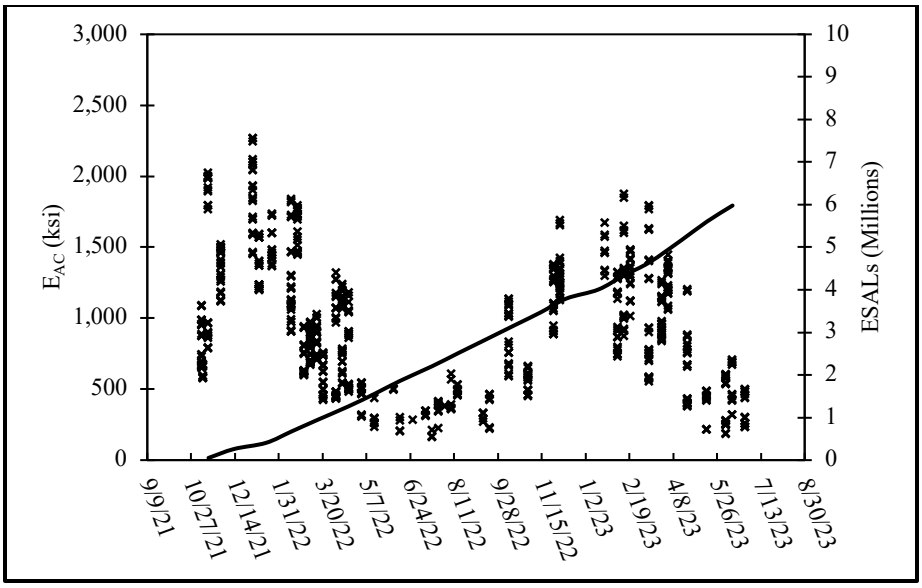

Figure 5.6.2: E_{AC} versus Time and Trafficking Level for N7 (Ctrl)

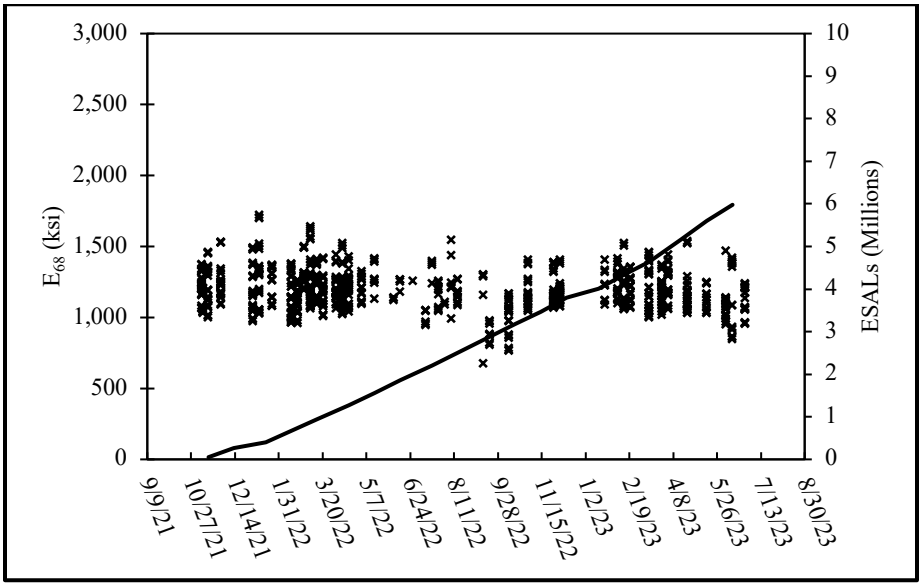

Figure 5.6.3: E_{68} versus Time and Trafficking Level for N7 (Ctrl)

5.7: Instrumentation

Each 200 ft AG section was instrumented with 12 asphalt strain gauges (ASGs), 2 earth pressure cells (EPCs), and 4 thermocouple temperature probes. For each test section, ASGs were installed in a 3x4 grid pattern centered in the outside wheelpath and consistent with previous instrumentation at the Test Track (Timm, 2009). *Figure 5.7.1* displays an example of this ASG grid, placed at the top of the granular base prior to paving, along with the leading EPC. These

gauges measure the longitudinal flexural tensile strain at the bottom of the AC layer. The grid pattern allows for a "best hit" to be captured as the heavy vehicles drive through the test sections. One EPC was placed at the top of the subgrade layer, while the other was placed at the top of the granular base layer. The EPCs measure vertical pressure, and also act as a trigger system to activate and deactivate the ASG array when a heavy vehicle passes through the section. The thermocouple temperature probes provide temperatures at the top, middle, and bottom of the AC in addition to 3 inches into the aggregate base layer. More details regarding the monitoring equipment and its installation have been published previously (Foshee, 2022).

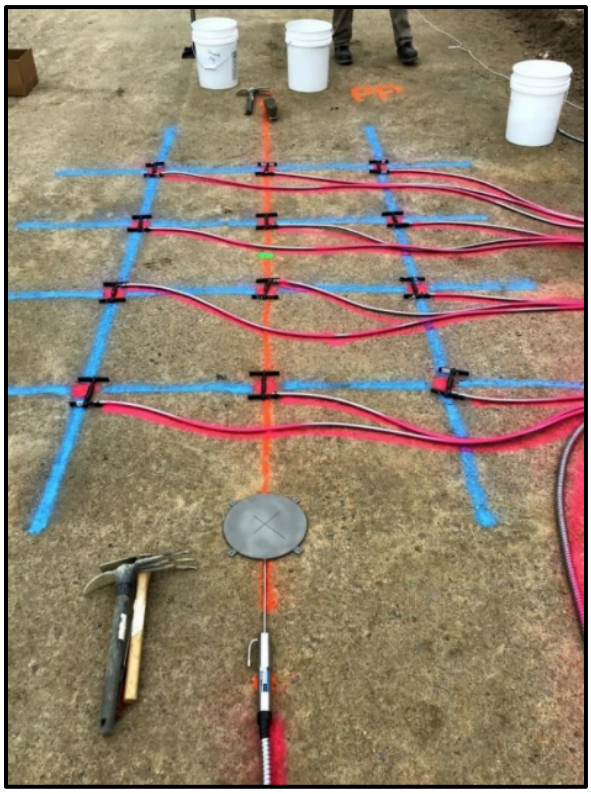

Figure 5.7.1: Example ASG Array and EPC (Foshee, 2022)

5.8: Strain Data Collection, Processing, and Analysis

Strain data were collected and processed on a weekly basis at the Test Track. The ASGs provide a raw voltage output when flexural strain is experienced. During a given data collection period, approximately 20 passes were captured for each section. A truck pass is defined as the period in which the truck (shown by *Figure 5.4.1*) passes through the 3x4 ASG array, resulting in 8 individual axle events. *Figure 5.8.1* displays an example of the raw voltage versus time output for a single ASG during a truck pass. The signal peaks correspond to the tensile strains induced by the steer axle, tandem axle, and 5 single axles passing over the ASG (Foshee, 2022). The raw voltage versus time data recorded by each functional ASG are post-processed to find the tensile strain

peaks and compressive inflection points. *Figure 5.8.2* provides an example of these peaks and inflection points identified within the DADiSP® 2002 software used for post-processing (Foshee, 2022).

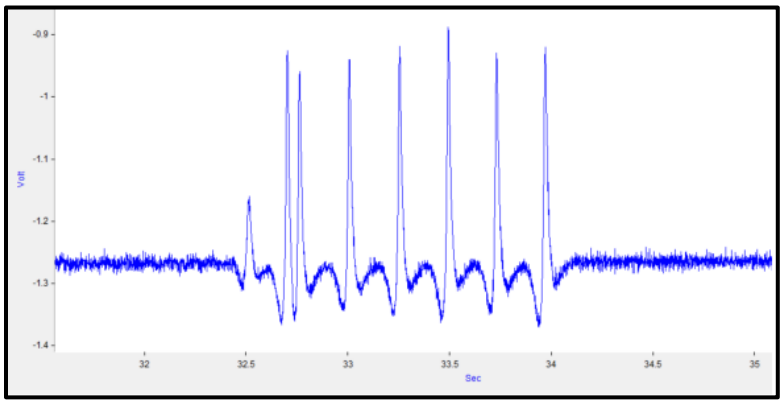

Figure 5.8.1: Example Raw ASG Output for a Single "Truck Event" (Foshee, 2022)

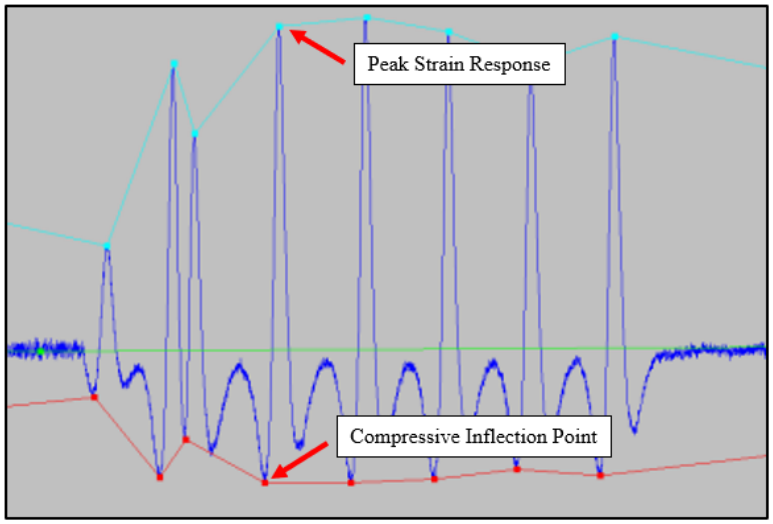

Figure 5.8.2: Peak Strain and Inflection Points Identified by DADiSP® 2002 (Foshee, 2022)

Strain responses were computed for each axle event, across every functional ASG within the array. The strain response is defined as the absolute magnitude of the difference between the compressive inflection point and the peak tensile strain within a single axle event. While all strain response data is collected, processed, and stored, only the strain responses induced by the 5 single axles of each heavy weight vehicle were considered for analysis for the AG test sections as they represent the majority of axle passes. The 95th percentile of these strain responses was considered to adequately represent the "best hit", where a truck passed directly over the gauge, inducing the maximum

possible strain response. Utilizing the 95th percentile strain response also filtered out any erroneously high strain response measurements (Foshee, 2022).

Similar to the backcalculated AC moduli, a pavement's strain response is highly susceptible to temperature effects. Increased pavement temperature leads to increased strain responses, while the opposite is true for decreased pavement temperature. An identical temperature normalization process was used for the 95th percentile strain response data. *Equation 5.8.1* defines the exponential relationship between the 95th percentile strain response and mid-depth pavement temperature, while *Equation 5.8.2* provides the temperature normalization relationship. The 95th percentile strain responses are normalized to a temperature of 68°F. *Figure 5.8.3* displays 95th percentile strain responses for section N7 (Ctrl) versus mid-depth pavement temperature and illustrates the relationship provided by *Equation 5.8.1*. *Figure 5.8.4* and *Figure 5.8.5* provide the 95th percentile strain responses for section N7 (Ctrl) versus the date at which they were collected (and the trafficking level in ESALs). Additionally, *Figure 5.8.4* and *Figure 5.8.5* illustrate the effectiveness of the temperature normalization process.

$$\mu\varepsilon_{AC} = k_1 e^{k_2 T} \qquad \textit{Equation 5.8.1}$$

Where:

$\mu\varepsilon_{AC}$ = 95th percentile microstrain response
k_1 = fitting coefficient
k_2 = fitting coefficient
T = mid-depth pavement temperature, °F

$$\mu\varepsilon_{68} = E_{AC} e^{k_2(68-T)} \qquad \textit{Equation 5.8.2}$$

Where:

$\mu\varepsilon_{68}$ = temperature-normalized 95th percentile microstrain response
$\mu\varepsilon_{AC}$ = 95th percentile strain response
k_2 = fitting coefficient
T = mid-depth pavement temperature, °F

AC layer thickness also affects the magnitude of the 95th percentile strain response. Tensile strain response at the bottom of the AC layer decreases as the pavement thickness increases. *Figure 5.3.1* displays the AC layer thicknesses for the AG test sections. The 95th percentile strain responses measured for each AG section were normalized to the thickness of N7 (Ctrl) using *Equation 5.8.3* and *Equation 5.8.4*. *Figure 5.8.5* displays the thickness corrected and temperature normalized 95th percentile strain responses for section N7 (Ctrl) versus the date at which they were collected (and the trafficking level in ESALs). Further details regarding strain data collection, processing, and analysis have been previously published (Foshee, 2022).

$$CF = \frac{H^2}{H_{ref}{}^2}$$ *Equation 5.8.3*

Where:

CF = thickness correction factor
H = AC layer thickness, in.
H_{ref} = reference AC layer thickness, in.

$$\mu\varepsilon_{cor} = CF * \mu\varepsilon_{68}$$ *Equation 5.8.4*

Where:

$\mu\varepsilon_{cor}$ = thickness corrected, and temperature normalized 95th percentile strain response
CF = thickness correction factor
$\mu\varepsilon_{68}$ = temperature normalized 95th percentile strain response

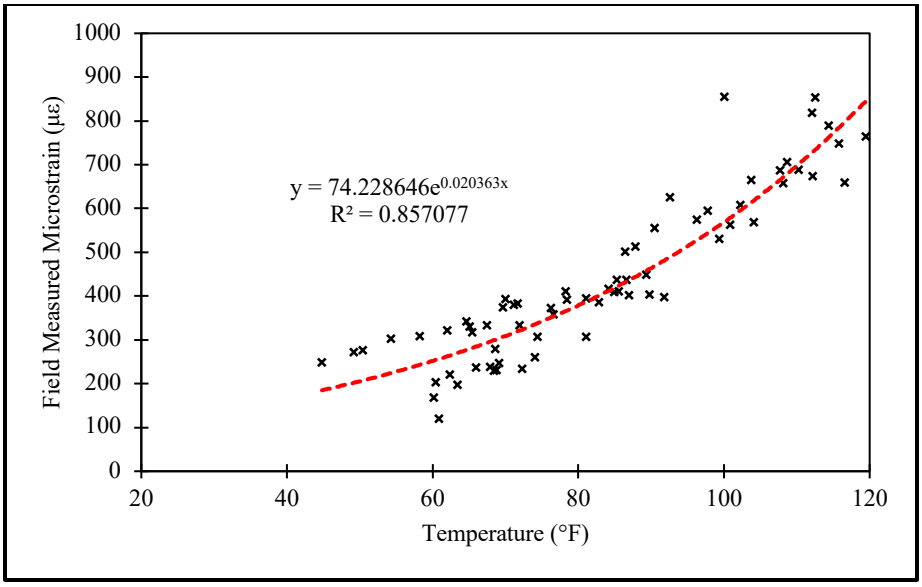

Figure 5.8.3: με versus Mid-Depth Pavement Temperature for N7 (Ctrl)

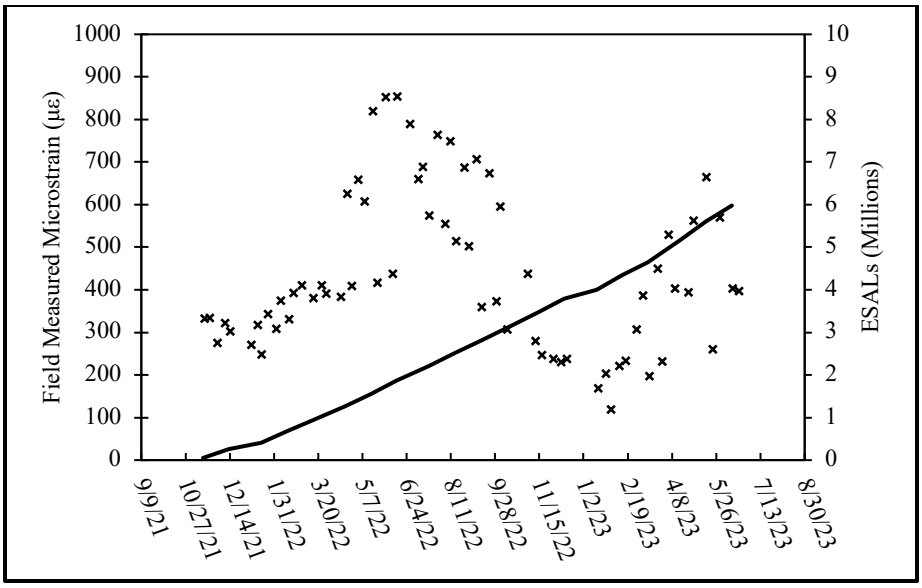

Figure 5.8.4: με versus Time and Trafficking Level for N7 (Ctrl)

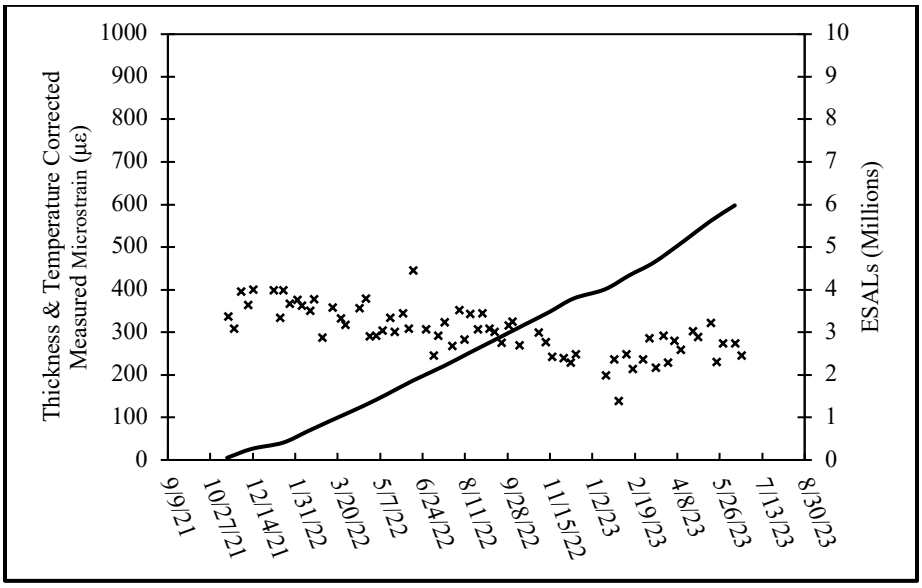

Figure 5.8.5: $\mu\varepsilon_{cor}$ versus Time and Trafficking Level for N7 (Ctrl)

5.9: Conclusion

This chapter provided a detailed insight into the construction, instrumentation, performance monitoring, and strain data collection for the full-scale AG sections at the NCAT Test Track. The next chapter will detail the results yielded from the full-scale field testing through June of 2023.

CHAPTER 6

Field Testing – Results & Discussion

6.1: Introduction

Performance data, including rut depth, cracking percentage, and ride quality, were recorded using a Pathways data collection van for each of the full-scale 200 ft AG sections at the NCAT Test Track. FWD testing was performed in the inside and outside wheelpaths, as well as between the wheelpaths, at 4 random stations within each test section. From this testing the asphalt concrete (E_{AC}), granular base (E_{GB}), and subgrade ($E_{Subgrade}$) layer moduli were backcalculated. Finally, the AG sections were instrumented with ASGs, EPCs, and thermocouple temperature probes in order to measure and characterize their structural behavior. These data sets are presented and discussed in this chapter.

6.2: Ride Quality, Rutting, & Cracking

Figure 6.2.1, *Figure 6.2.2*, and *Figure 6.2.3* display the ride quality, quantified via the International Roughness Index (IRI), versus trafficking level for the rubber-modified, fiber-modified, and plastic-modified AG test sections, respectively, relative to the control mixture. The IRI magnitude over the monitoring period should not be compared, since the initial differences displayed were caused by the thick-lift paving and surface grinding processes. Rather, any IRI changes with respect to time, or trafficking, should be compared. No obvious changes in IRI were observed for any of the AG sections though June 2023 (approximately 6 million ESALs) indicating excellent ride quality performance so far.

Figure 6.2.4, *Figure 6.2.5*, and *Figure 6.2.6* display rut depth versus trafficking level for the rubber-modified, fiber-modified, and plastic-modified AG test sections, respectively, relative to the control mixture through approximately 6 MESALs (million ESALs). As expected, the average rutting depth in each AG section has increased, albeit slightly, as trafficking has continued. Each test section displays a similar amount of rutting, which is far below the failure threshold of 0.50 in. Additive technology does not appear to have impacted rutting performance of the sections.

Figure 6.2.7 displays the percentage of cracking in the entire lane area for each AG section over time with MESALs also plotted on the secondary y-axis. *Figure 6.2.7* displays the percentage of cracking only in the wheelpath area. Only the cracking detected by the Pathways van was plotted on each figure. N1 (GTRDry) and S5 (DryPlastic) were the only test sections to display any amount of cracking though June 2023. Cracking was manually observed in section N1 (GTRDry) at approximately 2.51 million ESALs and was first detected by the Pathways van at 3.79 million ESALs. Cracking was manually observed in section S5 (DryPlastic) at approximately 5.17 million ESALs and was first detected by the Pathways van at 5.98 million ESALs. The cracking observed is relatively minor for N1 (GTRDry), and barely perceptible for S5 (DryPlastic). So far, the measured IRI for both sections does not appear to show any increases due to cracking.

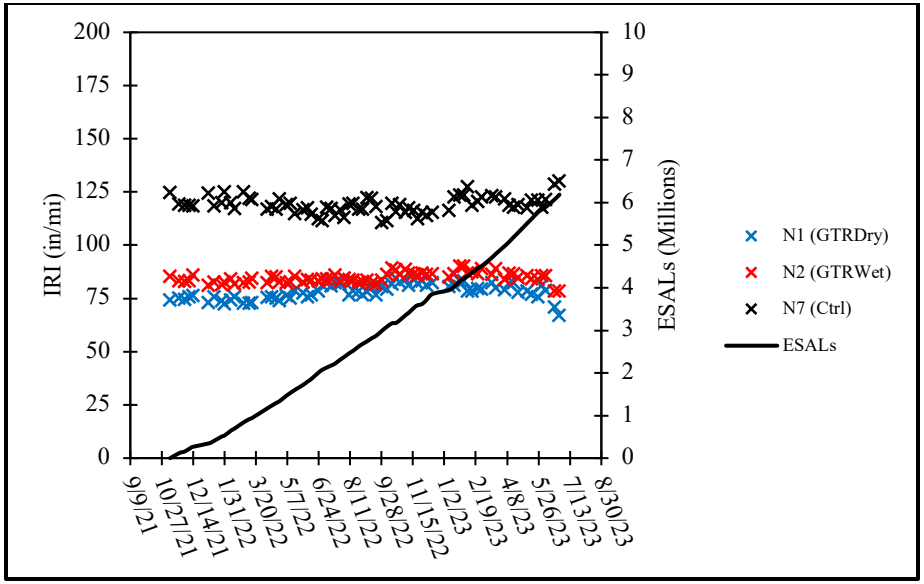

Figure 6.2.1: IRI (Rubber-Modified Test Sections)

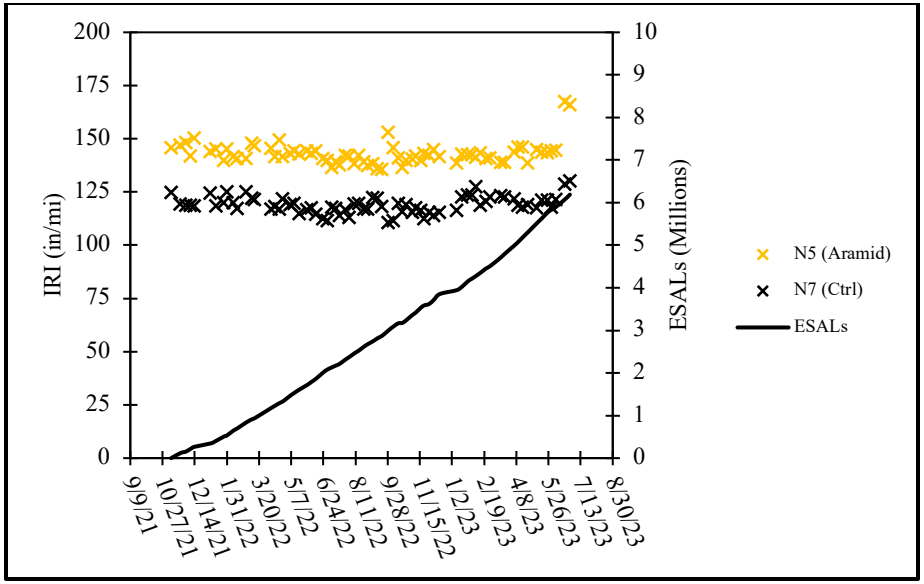

Figure 6.2.2: IRI (Fiber-Modified Test Section)

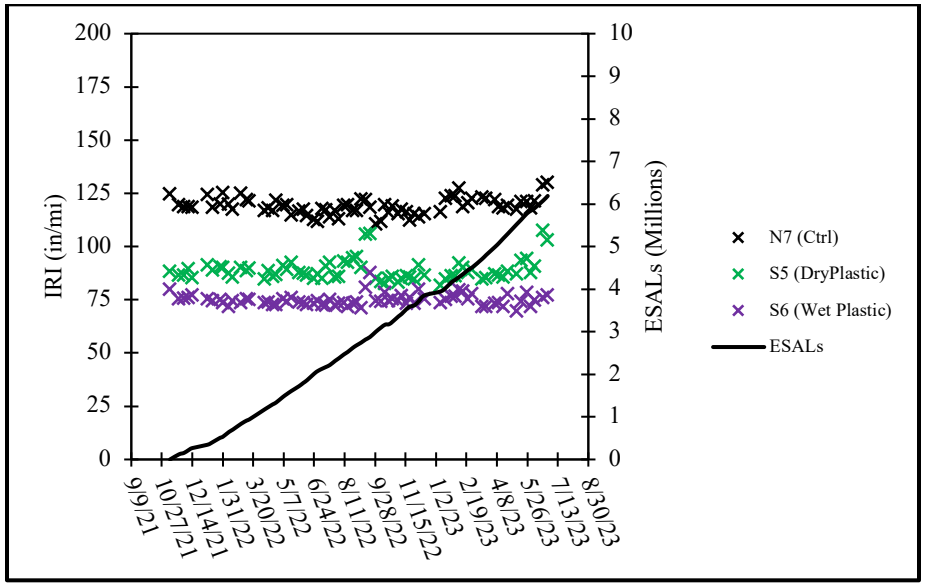

Figure 6.2.3: IRI (Plastic-Modified Test Sections)

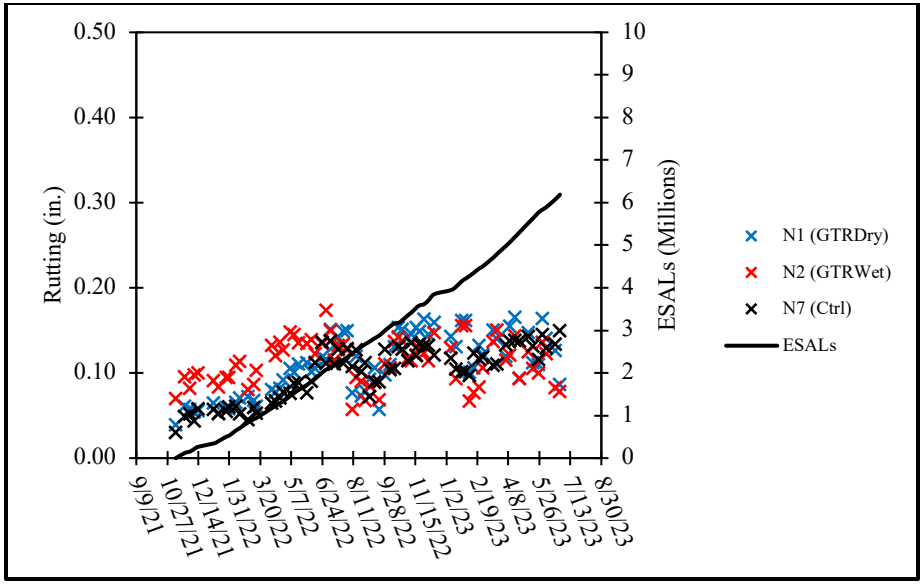

Figure 6.2.4: Rutting (Rubber-Modified Test Sections)

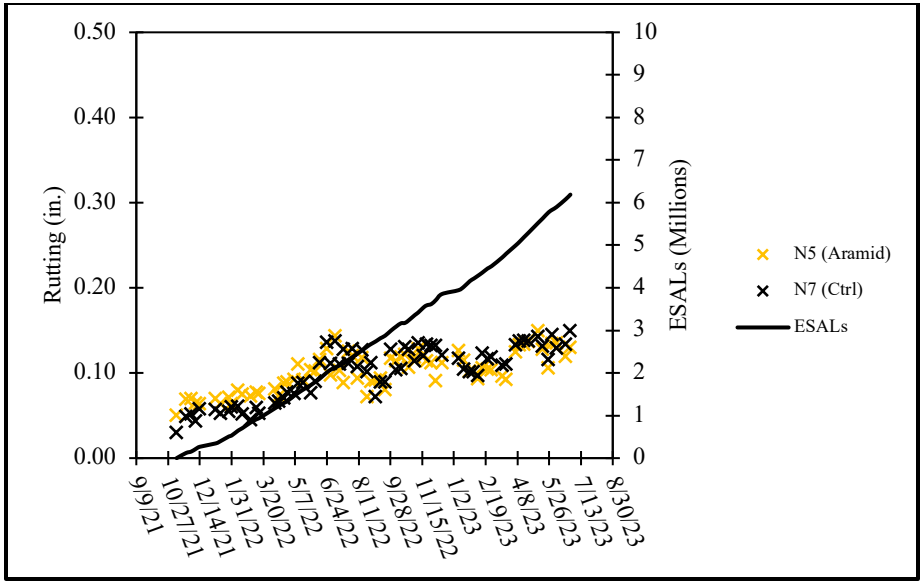

Figure 6.2.5: Rutting (Fiber-Modified Test Section)

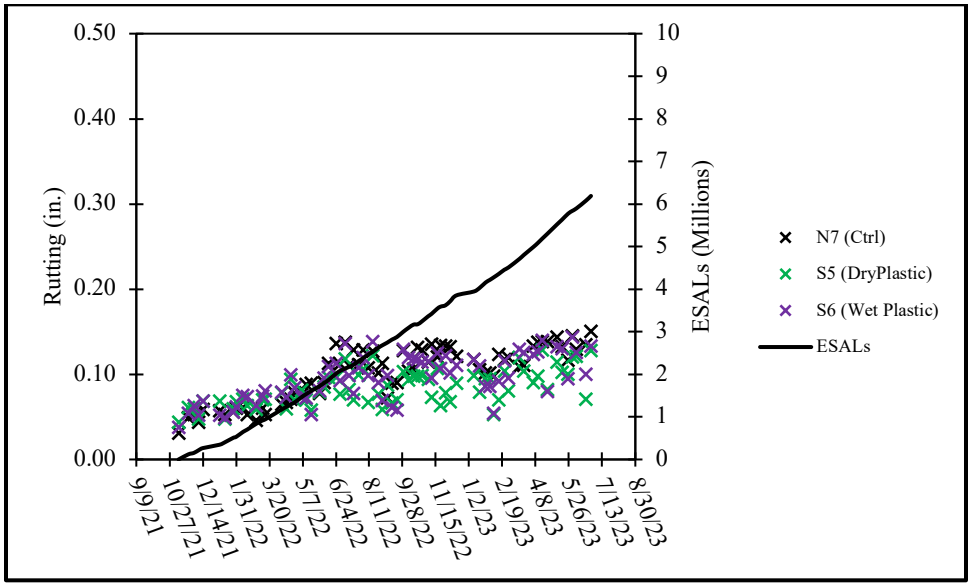

Figure 6.2.6: Rutting (Plastic-Modified Test Sections)

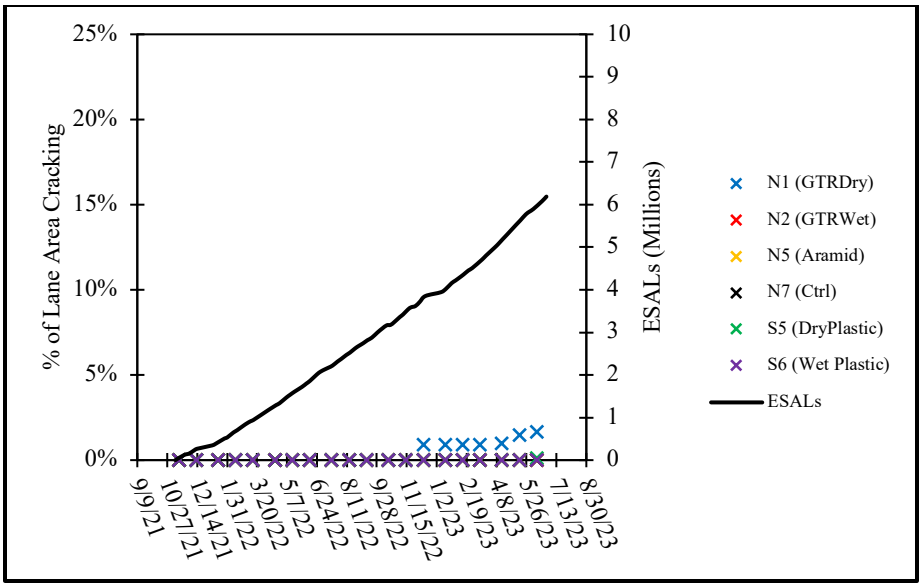

Figure 6.2.7: Percentage Lane Area Cracking

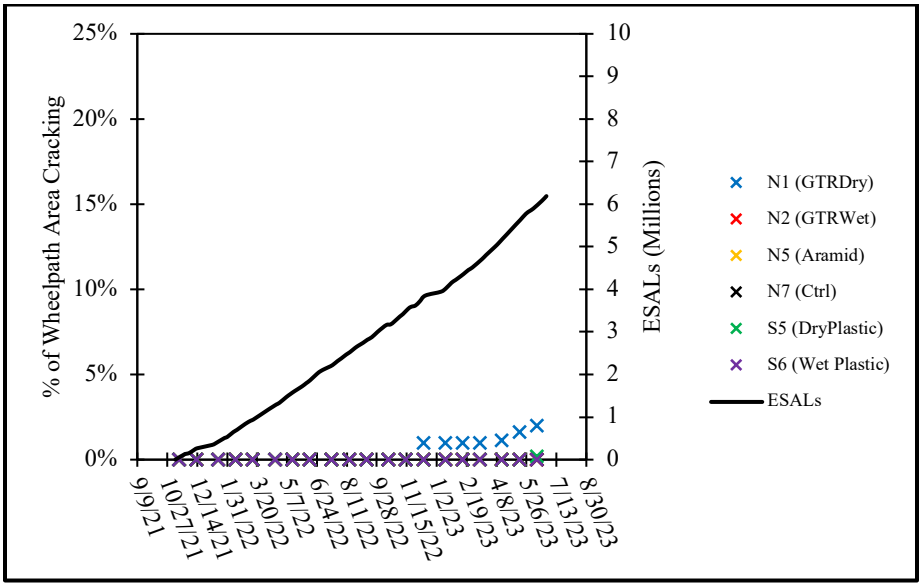

Figure 6.2.8: Percentage Wheelpath Area Cracking

6.3: FWD Backcalulation

Figure 6.3.1, *Figure 6.3.2*, and *Figure 6.3.3* display the backcalculated AC layer moduli (E_{AC}) (before temperature correction) for the rubber-modified, fiber-modified, and plastic-modified sections relative to the control, respectively. *Figure 6.3.4*, *Figure 6.3.5*, and *Figure 6.3.6* display the temperature-corrected, backcalculated AC layer moduli (E_{68}) for the rubber-modified, fiber-modified, and plastic-modified sections relative to the control, respectively. The backcalculated

AC moduli were normalized to 68°F to allow for any changes in the AC moduli as trafficking occurred to be observed independent of temperature effects. As of June 2023, none of the AG test sections have shown any obvious changes in their E_{68}. This includes sections N1 (GTRDry) and S5 (DryPlastic), both of which have had minor levels of cracking at this point. An ANOVA and Tukey-Kramer Analysis was performed, using an α of 0.05, to evaluate the average E_{68} for each test section (*Figure 6.3.7*) (see *Table B.1.1* and *Table B.1.2* for average E_{68} ANOVA and Tukey-Kramer computations, respectively). The average in-situ AC moduli of the sections were found to be statistically different. Both N1 (GTRDry) and N2 (GTRWet) had a lower average E_{68} in comparison to N7 (Ctrl), with N1 (GTRDry) displaying the lowest amongst all sections. The average E_{68} of N5 (Aramid) was very similar, albeit slightly lower than that of N7 (Ctrl). S5 (DryPlastic) and S6 (WetPlastic) had higher average E_{68} values in comparison to N7 (Ctrl), with S5 (DryPlastic) displaying the highest amongst all sections.

Figure 6.3.8 and *Figure 6.3.9* display the average backcalculated granular base (E_{GB}) and subgrade moduli ($E_{Subgrade}$), respectively. An ANOVA and Tukey-Kramer Analysis was performed, using an α of 0.05, to evaluate the average E_{GB} and $E_{Subgrade}$ for each test section (see *Table B.2.1* and *Table B.3.1* for the ANOVA computations and *Table B.2.2* and *Table B.3.2* for Tukey-Kramer computations for E_{GB} and $E_{Subgrade}$, respectively). Neither moduli are prone to significant temperature effects, therefore temperature correction was not necessary. It was observed that N7 (Ctrl) had a significantly average higher E_{GB} and $E_{Subgrade}$ relative to the other AG sections. Additionally, the average measured strain response in N7 (Ctrl) was found to be significantly lower in comparison to the other AG sections (*Figure 6.4.7*). Previous studies conducted at NCAT also found the $E_{Subgrade}$ of N7 (Ctrl) to be higher than the other sections on the northern tangent of the Test Track, including N1 (GTRDry), N2 (GTRWet), and N5 (Aramid) (Taylor, 2008 and Timm and Priest, 2006).

N1 (GTRDry) had the lowest average E_{GB} and an average $E_{Subgrade}$ that fell within the middle of the pack, N1 (GTRDry) also had the highest average measured strain response of all the sections (*Figure 6.4.4* and *Figure 6.4.7*). S5 (DryPlastic) was found to have the second highest average E_{GB} and the lowest average $E_{Subgrade}$. S5 (DryPlastic) was also found to have an average measured strain response greater than that of N7 (Ctrl), despite having a higher laboratory and field-evaluated stiffness. *Figure 6.4.8* and *Figure 6.4.9* plot E_{68} and E_{GB} versus the average temperature and thickness-corrected measured strain responses ($\mu\varepsilon_{cor}$). Predictably, there was good correlation between E_{68} and $\mu\varepsilon_{cor}$. However, it was also found that E_{GB} also displayed a good correlation with $\mu\varepsilon_{cor}$, independent of E_{68}. Similar trends were observed for E_{68} versus $\mu\varepsilon_{cor}$ and E_{GB} versus $\mu\varepsilon_{cor}$. An increase of either moduli resulted in a decrease in the magnitude of the average measured strain response. This result was expected, as a pavement with a higher AC modulus should exhibit lower magnitudes of tensile strain for the same applied load level (in this case the NCAT heavy weight vehicles). Similarly, increased foundational support from the granular base layer should also result in lower magnitudes of tensile strain (at the bottom of the AC layer) for the same applied load level. *Figure 6.4.10* indicated that there was no significant relationship between $E_{Subgrade}$ and $\mu\varepsilon_{cor}$. These findings led to several conclusions. The first being that the significantly lower $\mu\varepsilon_{cor}$ in the N7 (Ctrl) section was likely due to a combination of its higher granular base modulus and its above average E_{68}. The second conclusion was that the significantly higher $\mu\varepsilon_{cor}$ observed in section N1

(GTRDry) was likely due to a combination of lower granular base modulus and below average E_{68}. The third conclusion was that reduced granular base modulus will lead to increased tensile strain, independent of the AC modulus, as seen when comparing the $\mu\varepsilon_{cor}$ of sections N7 (Ctrl) and S5 (DryPlastic). As an additional note, previous investigations have confirmed the NCAT Test Tack foundation layers to be unconventional, with an $E_{Subgrade}$ greater than E_{GB}. Average ratios between E_{GB} and $E_{Subgrade}$ of 0.34 to 0.37 have been observed (Taylor, 2006 and Timm and Tutu, 2017). The interaction of all these variables will be further explored in the next chapter where lab and field data are considered in an in-depth analysis.

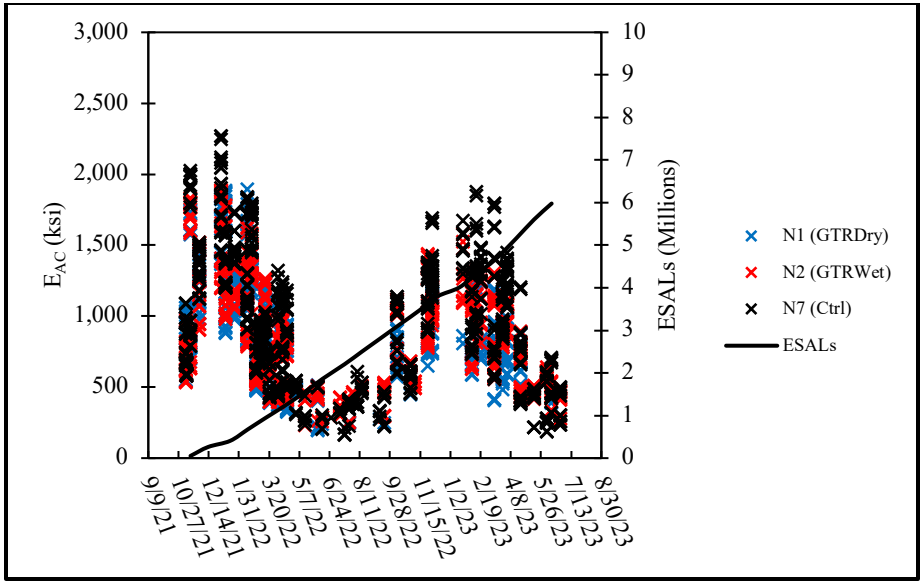

Figure 6.3.1: E_{AC} (Rubber-Modified Test Sections)

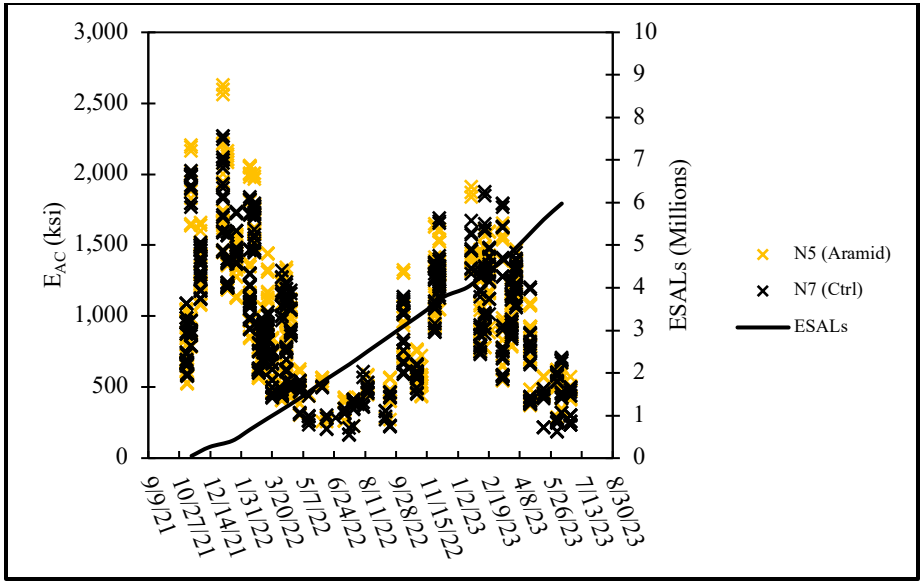

Figure 6.3.2: E_{AC} (Fiber-Modified Test Section)

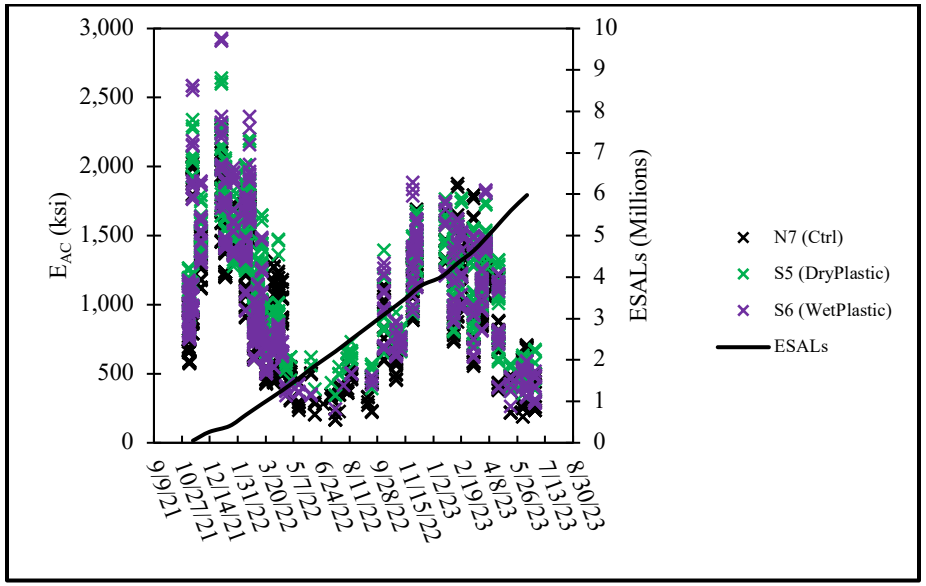

Figure 6.3.3: E_{AC} (Plastic-Modified Test Sections)

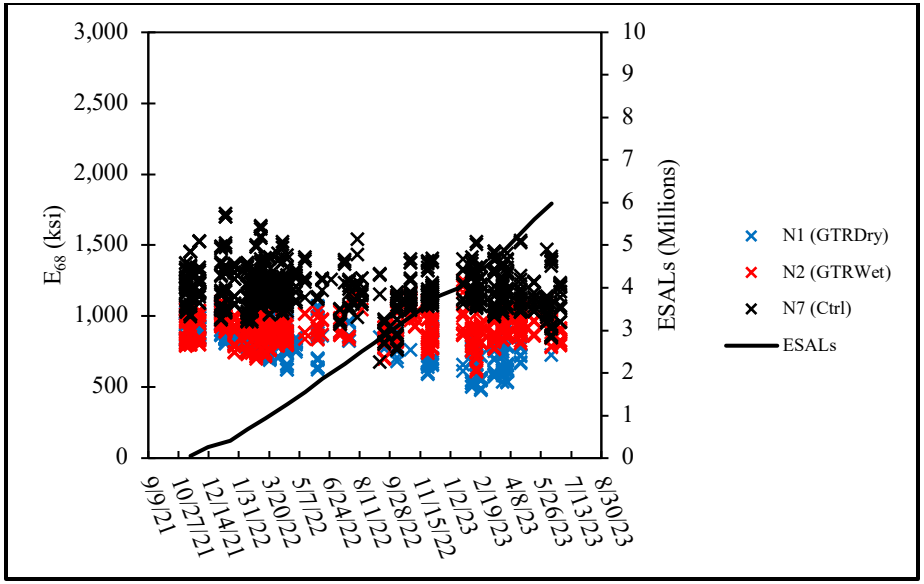

Figure 6.3.4: E_{68} (Rubber-Modified Test Sections)

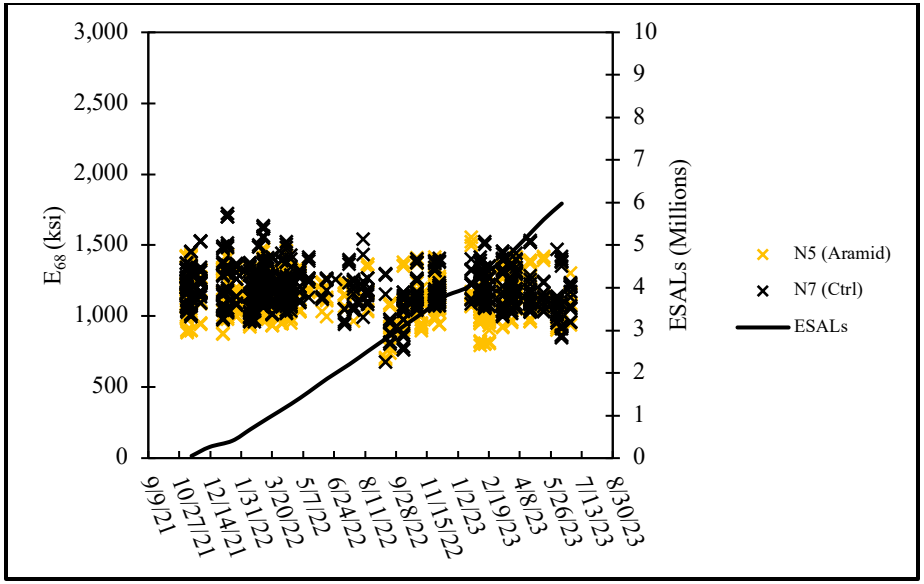

Figure 6.3.5: E_{68} (Fiber-Modified Test Section)

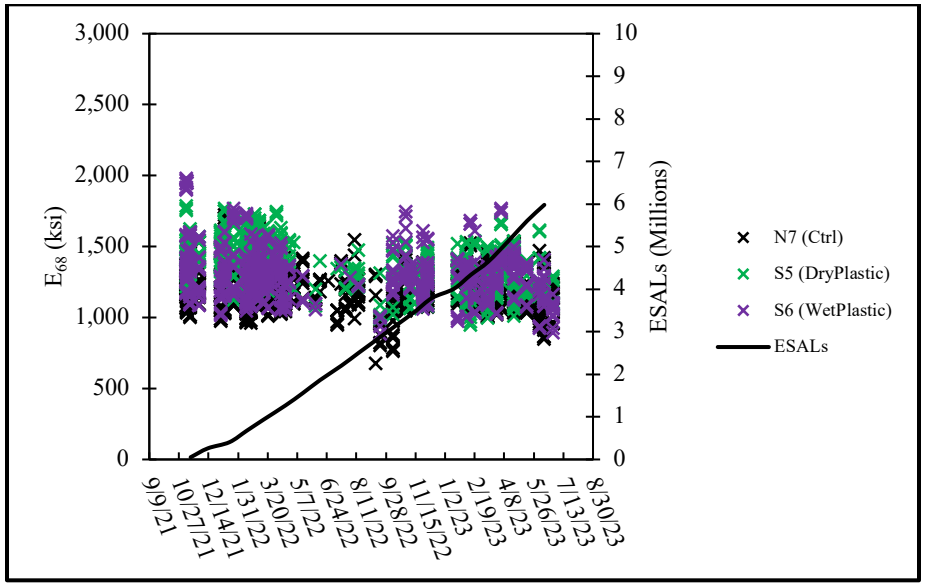

Figure 6.3.6: E_{68} (Plastic-Modified Test Sections)

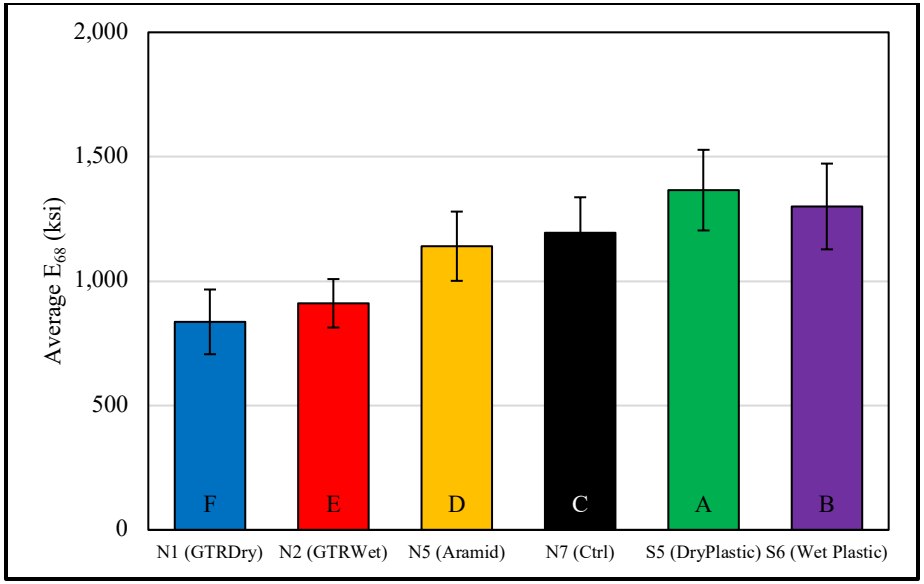

Figure 6.3.7: Average E_{68}

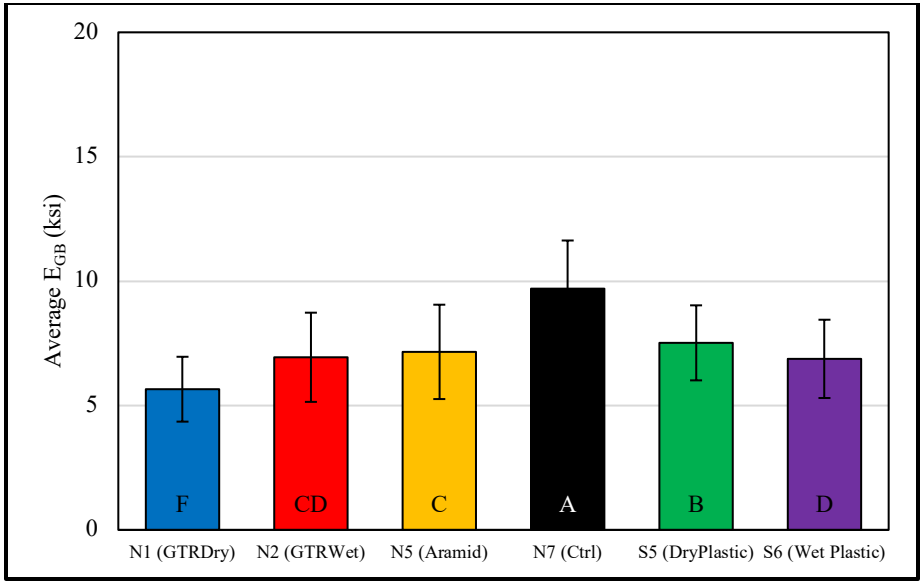

Figure 6.3.8: Average E_{GB}

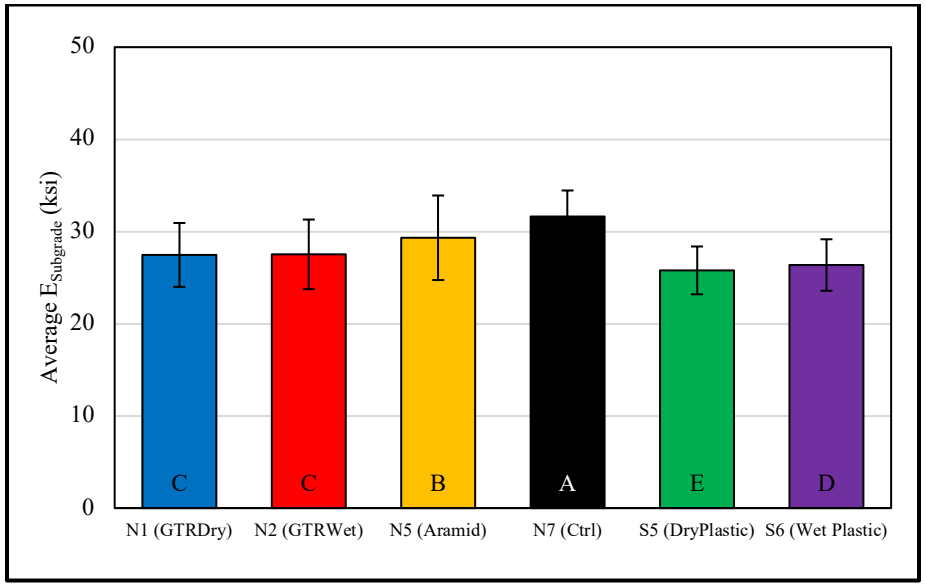

Figure 6.3.9: Average $E_{Subgrade}$

6.4: Strain Measurements

Figure 6.4.1, *Figure 6.4.2*, and *Figure 6.4.3* display the 95th percentile strain responses (before thickness and temperature corrections) that were recorded through June 2023 for the rubber-modified, fiber-modified, and plastic-modified test sections, respectively. *Figure 6.4.4*, *Figure 6.4.5*, and *Figure 6.4.6* display the thickness- and temperature-corrected 95th percentile strain responses ($\mu\varepsilon_{cor}$) for the rubber-modified, fiber-modified, and plastic-modified test sections, respectively. Also plotted is the cumulative ESALs through June 2023. The post-processed strain response data presents significant variation, and some remnants of the seasonal temperature effects are still observable (particularly so for N5 (Aramid)). Regardless, a number of sound observations were achieved. The first observation was that there have been no obvious increases in $\mu\varepsilon_{cor}$ for any of the AG sections as of June 2023. *Figure 6.4.7* displays the average thickness- and temperature-corrected field measured strain response for each section. An ANOVA and Tukey-Kramer analysis, using an α of 0.05, were performed to identify which sections had statistically different and/or similar average values of $\mu\varepsilon_{cor}$ (see *Table B.4.1* and *Table B.4.2* for average $\mu\varepsilon_{cor}$ ANOVA and Tukey-Kramer computations, respectively). N1 (GTRDry) was found to have the highest strain response, followed by N2 (GTRWet). N7 (Ctrl) had the lowest strain response, being less than half of what was measured for N1 (GTRDry). This increased strain level is what likely caused N1 (GTRDry) to display cracking before any of the other AG test sections. The increased strain level is likely due to a number of contributing factors, including the reduced stiffness of the mixture relative to N7 (Ctrl), as displayed by its E* master curve (*Figure 4.2.4*), its initial flexural stiffness (*Figure 4.4.1*), and its E_{68} (*Figure 6.3.7*). Additionally, N1 (GTRDry) had the lowest E_{GB} (low foundation modulus relative to the other sections). N1 (GTRDry) was also found to have average flexural strain-tolerance in the laboratory, as shown by its fatigue life transfer function (*Figure 4.4.2*). N2 (GTRWet) was also found to have high values of measured strain, however this mixture displayed excellent flexural strain-tolerance (*Figure 4.4.2*) in lab testing and has yet to display any signs of cracking. S5 (DryPlastic) was found to have statistically similar average values of strain with N5 (Aramid) and N7 (Ctrl). The early cracking that has been observed in the S5 (DryPlastic) test section is likely due to its reduced strain-tolerance, which was the lowest amongst all AG mixtures (*Figure 4.4.5*) in lab testing.

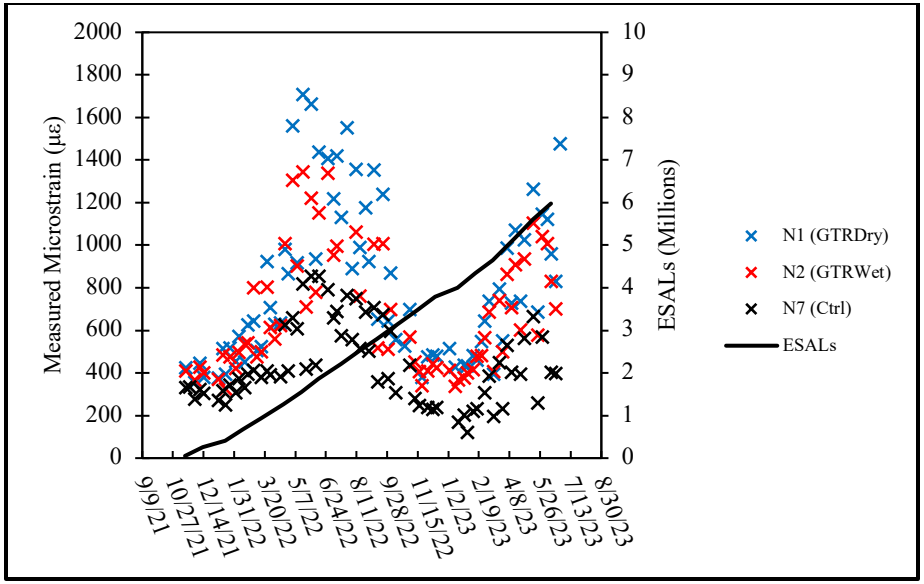

Figure 6.4.1: με (Rubber-Modified Sections)

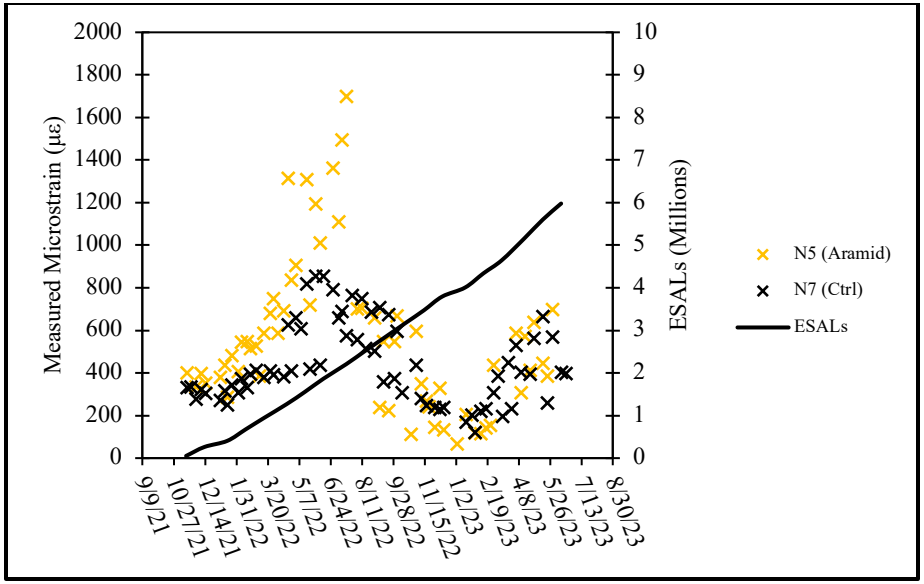

Figure 6.4.2: με (Fiber-Modified Section)

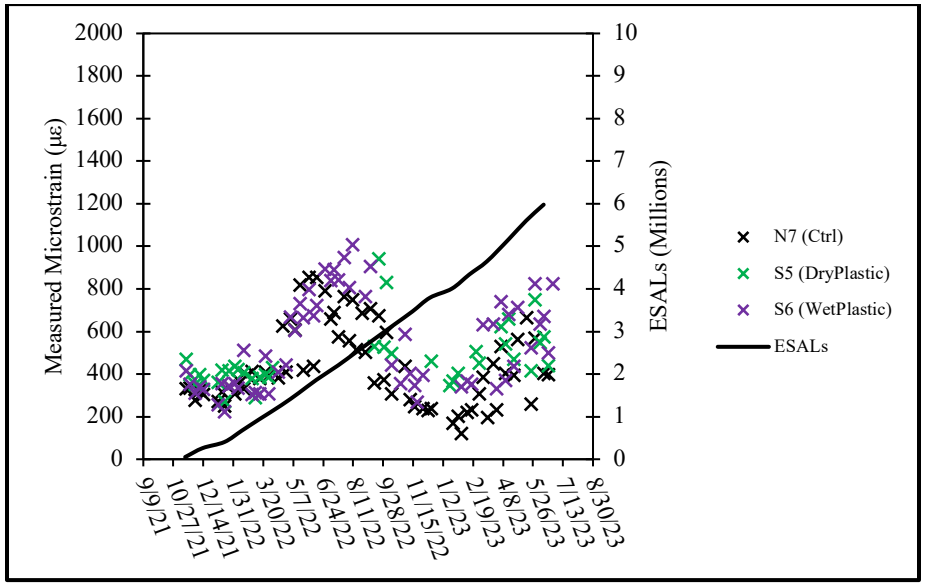

Figure 6.4.3: με (Plastic-Modified Sections)

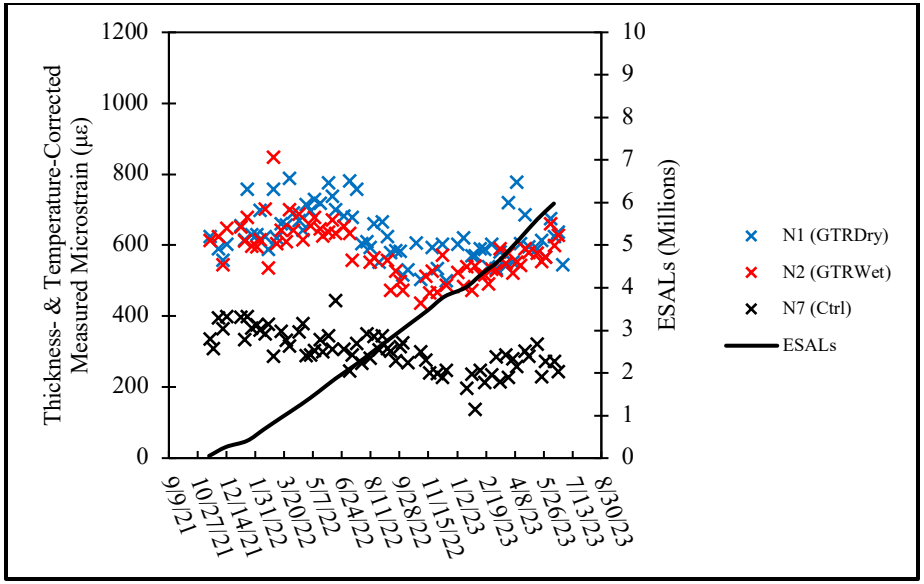

Figure 6.4.4: $\mu\varepsilon_{cor}$ (Rubber-Modified Sections)

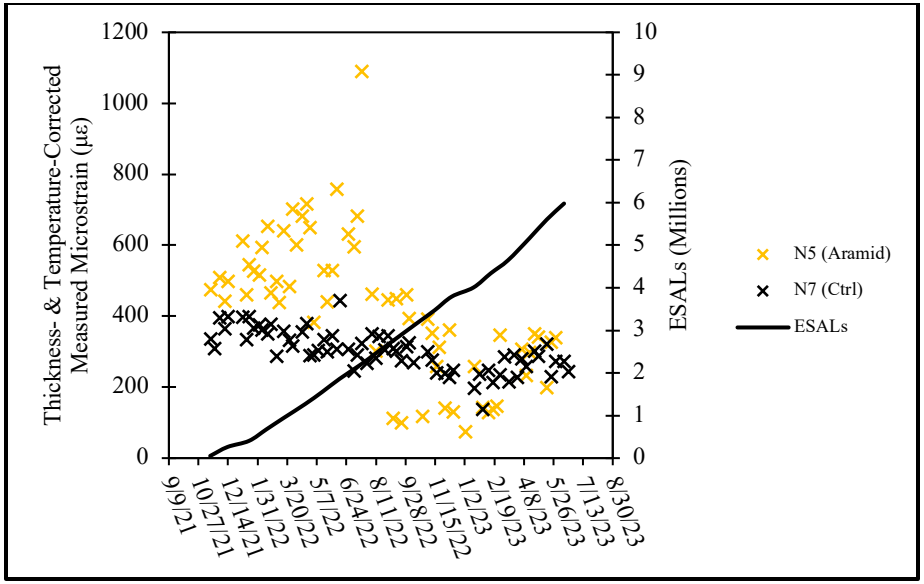

Figure 6.4.5: $\mu\varepsilon_{cor}$ (Fiber-Modified Section)

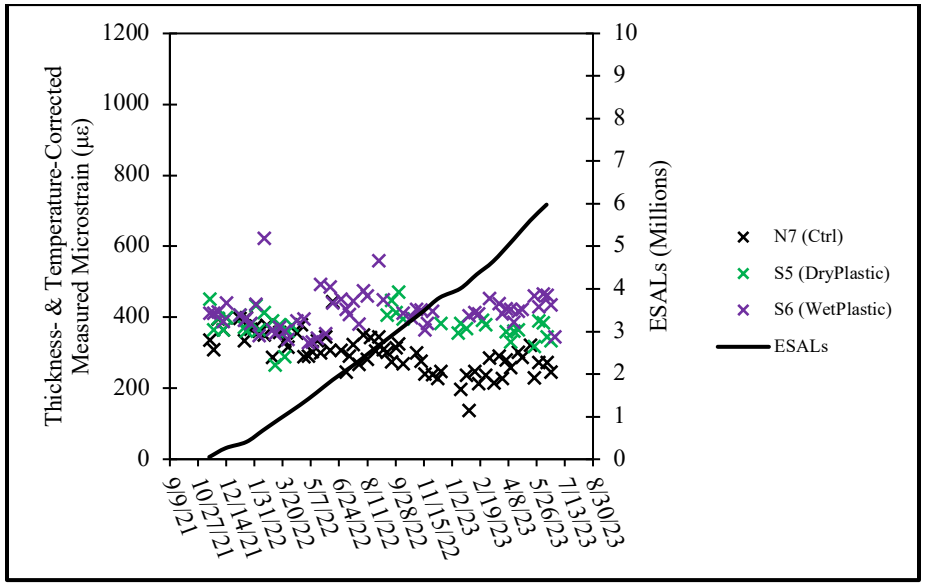

Figure 6.4.6: $\mu\varepsilon_{cor}$ (Plastic-Modified Sections)

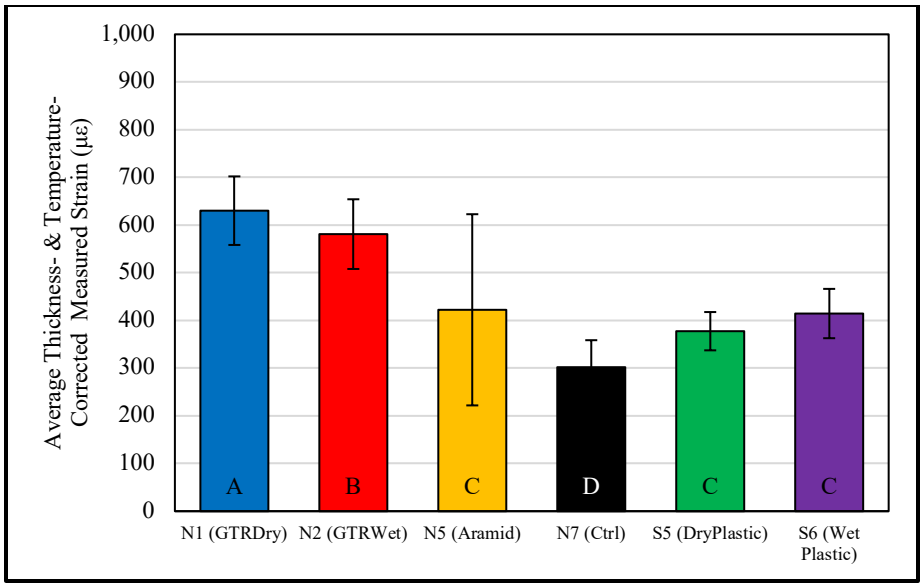

Figure 6.4.7: Average $\mu\varepsilon_{cor}$

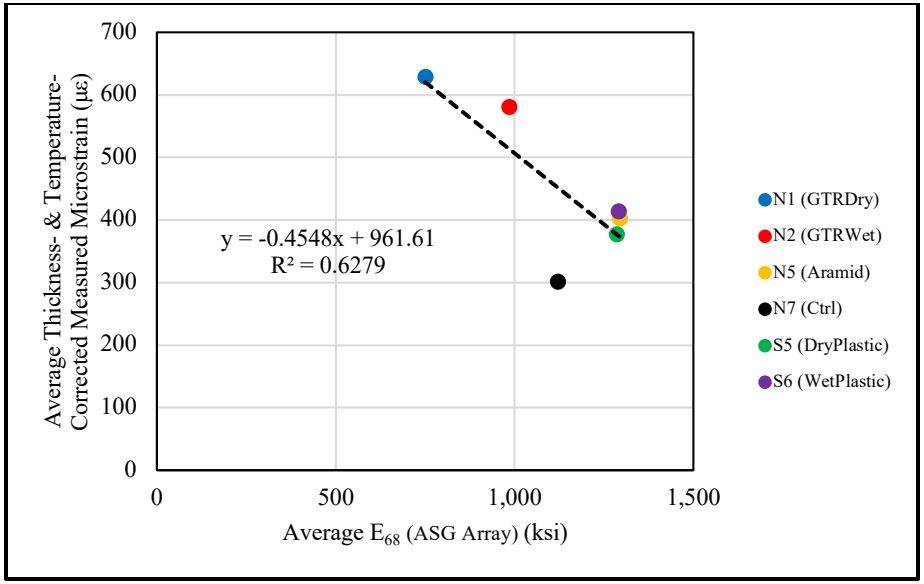

Figure 6.4.8: Average E_{68} (ASG Array) versus Average $\mu\varepsilon_{cor}$

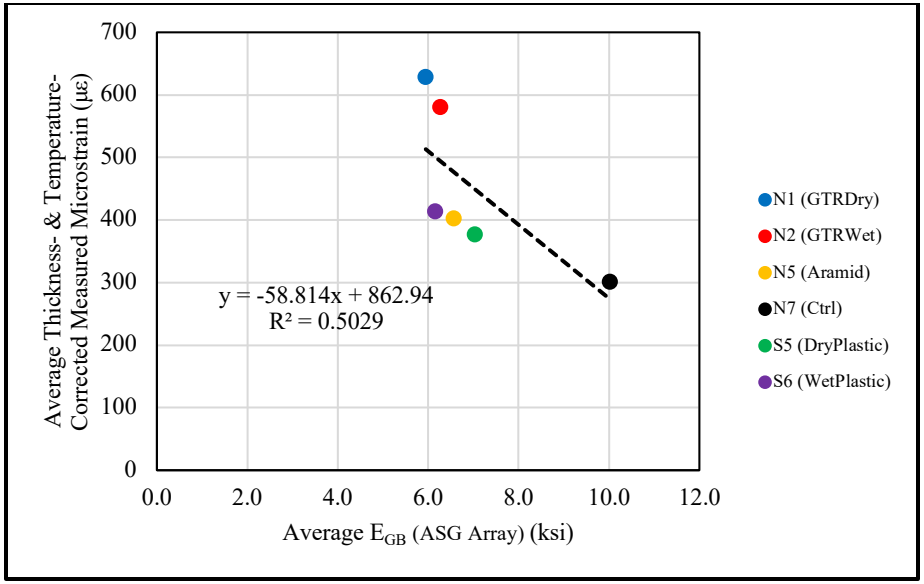

Figure 6.4.9: Average E_{GB} (ASG Array) versus Average $\mu\varepsilon_{cor}$

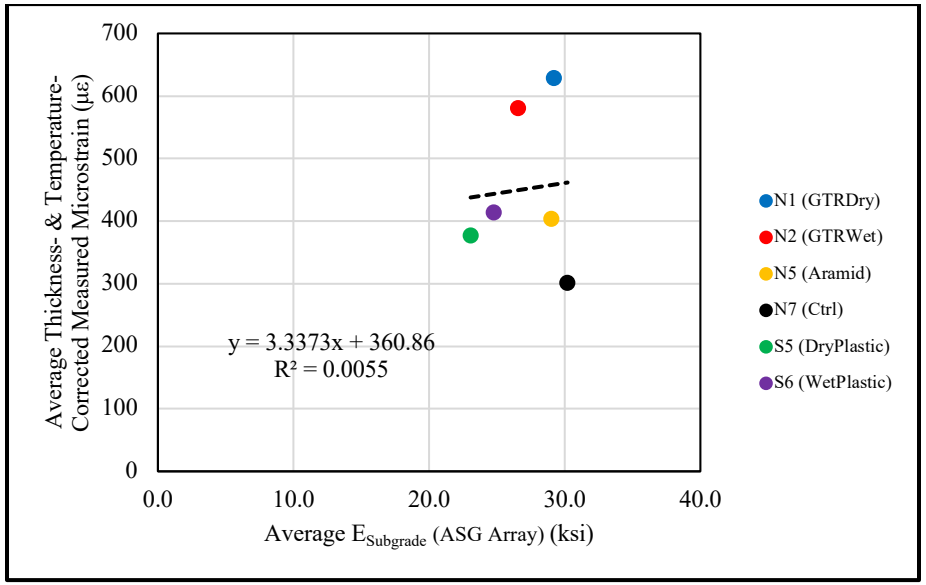

Figure 6.4.10: Average $E_{Subgrade}$ (ASG Array) versus Average $\mu\varepsilon_{cor}$

6.5: Findings

This chapter presented the results of the full-scale field evaluation of each of the AG mixtures. For each mixture, a 200 ft test section was paved and instrumented with ASGs, EPCs, and thermocouple temperature probes. Performance data (IRI, average rut depth, and cracking percentage) was recorded on a weekly basis. Backcalculated layer moduli data (E_{68}, E_{GB}, and $E_{Subgrade}$) and strain response data were recorded several times per month for each AG section. All field results presented in this chapter were based on field data obtained between the start of October 2021 through June 2023.

No changes in obvious changes IRI were observed for any of the sections (*Figure 6.2.1*, *Figure 6.2.2*, and *Figure 6.2.3*). Each section displayed a similar amount of rutting, far below the allowable threshold of 0.50 in (*Figure 6.2.4*, *Figure 6.2.5*, and *Figure 6.2.6*). Sections N1 (GTRDry) and S5 (DryPlastic) were the only to display any percentage of cracking (*Figure 6.2.7 and Figure 6.2.8*). Cracking in N1 (GTRDry) was likely due to the high values of measured strain (*Figure 6.4.7*) which were caused by the mixture's reduced stiffness (reflected by its E_{68}) and potentially by its poor granular base support relative to the other AG sections (this will be explored in the next chapter). The cracking measured in S5 (DryPlastic) was likely caused by the mixture's strain tolerance (fatigue life), which was the lowest amongst all mixtures (*Figure 4.4.5*). N7 (Ctrl) was found to have the lowest average value of measured strain response, though it was determined that this was likely due to its excellent foundational support (highest average E_{GB}) rather than its stiffness (E_{68}) or any other properties of the mixture itself. This observation in particular highlighted the importance of evaluating other external factors that may contribute to the overall performance of a particular mixture in the field. The final chapter will provide analysis of the relevant links between laboratory and full-scale field-testing results.

CHAPTER 7

Laboratory & Field Combined Analysis

7.1: Introduction

Linking the findings obtained from the suite of laboratory experiments with those from the full-scale field sections was one of the primary objectives of the AG experiment. To that end, this chapter explores relationships between the lab and field data.

7.2: Laboratory Stiffness and E_{68} Relationship

The linear relationships between E_{68} from backcalculation of FWD data and laboratory measured average dynamic modulus (E*) and average initial flexural stiffness are displayed in *Figure 7.2.1* and *Figure 7.2.2*, respectively. The data presented for both laboratory tests was gathered at 20°C, at a loading frequency of 10 Hz (understood to closely model to highway speeds). The backcalculated AC moduli were normalized to a temperature of 68°C (equivalent with 20°C) so that comparisons could be made independent of temperature effects. The average initial flexural stiffness provided a better fit, based upon the coefficient of determination (R^2) value, with average E_{68} in comparison to the average E* data. This finding makes sense given that beam fatigue testing applies a flexural strain rather than an axial strain (as with E*). Therefore, it more accurately models field loading conditions, and results in a stronger laboratory-to-field relationship. The variability seen in these relationships is due to many contributing factors, including, but not limited to, the differing foundational layer support (E_{GB} and $E_{Subgrade}$), as well as the inherent variability/error associated with average backcalculated AC moduli for each test section.

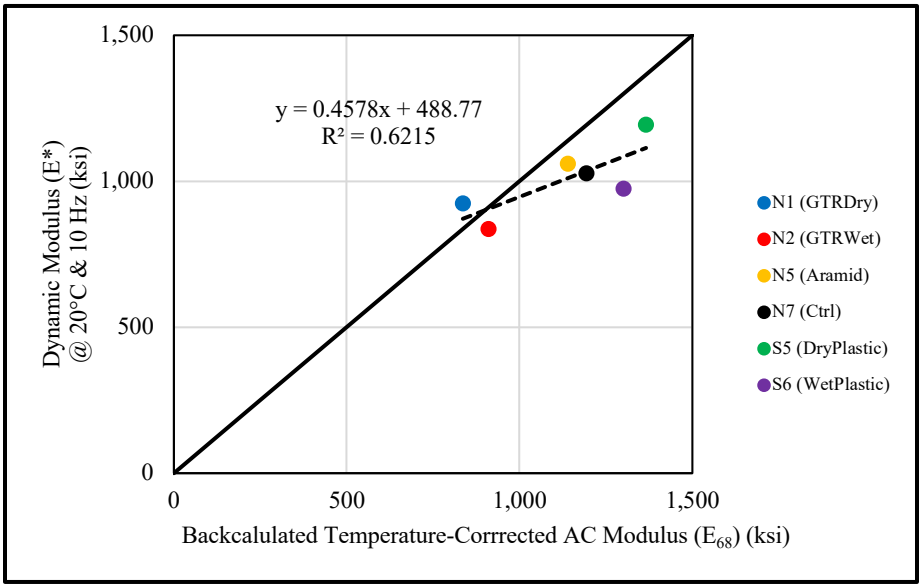

*Figure 7.2.1: E_{68} versus E**

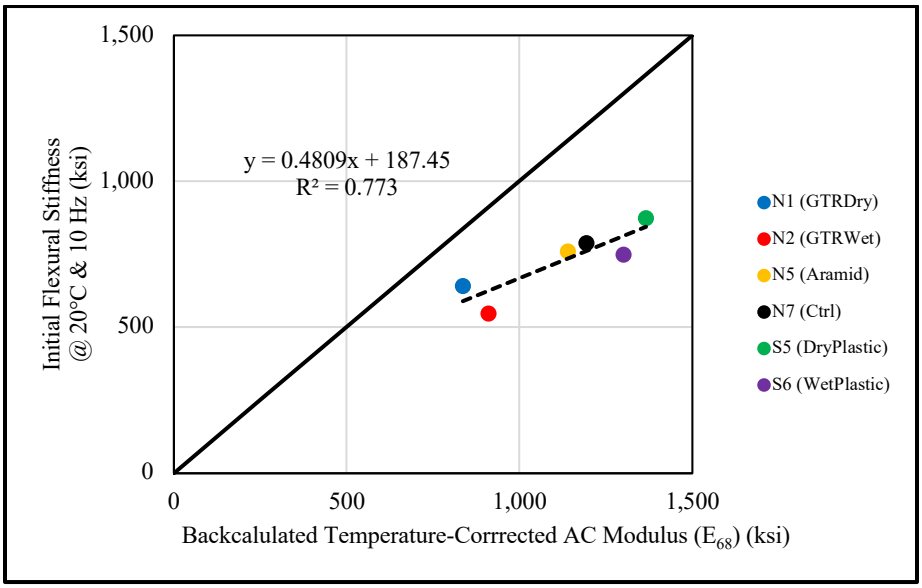

Figure 7.2.2: E_{68} versus Initial Flexural Stiffness

7.3: Laboratory Stiffness and Field-Measured Strain Response Relationship

The linear relationships between the average thickness- and temperature-corrected 95th percentile strain response ($\mu\varepsilon_{cor}$) and average dynamic modulus (E*) and average initial flexural stiffness are displayed by *Figure 7.3.1* and *Figure 7.3.2*, respectively. Like the modulus data presented above, the data presented for both laboratory tests was gathered at 20°C and a loading frequency of 10 Hz. Similar to the relationships displayed by *Figure 7.2.1* and *Figure 7.3.2*, the laboratory measured average initial flexural stiffness provided a better fit to the average field measured strain responses based upon the R^2 value. Again, this finding makes sense intuitively, given that the bending beam fatigue test more accurately resembles field loading conditions in comparison to the dynamic modulus (E*) test. A major source of variability within these relationships was error and limitations inherent to measuring the average 95th percentile strain response of each test section (a process that like layer moduli backcalulation, will never yield perfect results). Also, differences in foundational layer support (E_{GB} and $E_{Subgrade}$) likely contributed some level of variability to these linear relationships.

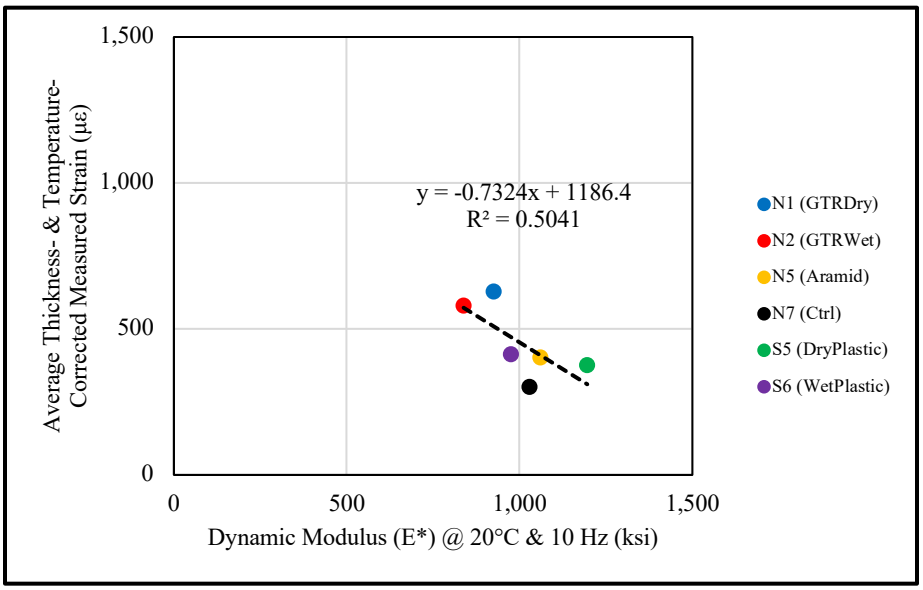

*Figure 7.3.1: $\mu\varepsilon_{cor}$ versus E**

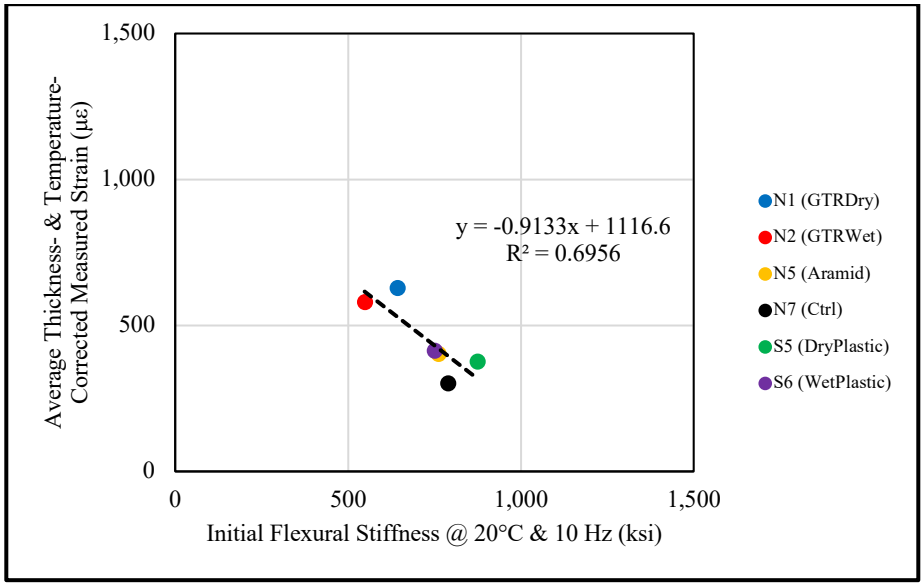

Figure 7.3.2: $\mu\varepsilon_{cor}$ versus Initial Flexural Stiffness

7.4: WESLEA Modeling

Individual statistical correlations between E_{AC}, E_{GB}, and $E_{Subgrade}$ and $\mu\varepsilon_{cor}$ (*Figure 6.4.8*, *Figure 6.4.9*, and *Figure 6.4.10*) were limited because they did not factor in the potential contributions of the other moduli. Therefore, the peak strain response of each AG section was modeled using WESLEA for Windows 3.0. This software utilizes layered elastic analysis, simulating strain levels at user specified locations (the bottom of the AC layer in this case). The WESLEA simulation

inputs included the layer moduli (E_{AC}, E_{GB}, and $E_{Subgrade}$) and the surveyed layer thicknesses (in the gauge array area for each section). *Table 7.4.1* provides a provides the section-specific moduli and thicknesses for WESLEA. The software default Poisson's ratios were used for the AC, GB, and subgrade layers (0.35, 0.40, and 0.45, respectively). A single axle, with a weight of 20,000 lbs and tire pressures of 110 psi, was used for the loading inputs. This specific axle wight was selected because it represented the average single axle weight amongst the NCAT heavy weight vehicles. The peak simulated microstrain value in the y-direction (longitudinal strain), occurring at the bottom of the AC layer, was selected.

Table 7.4.1: WESLEA Structural Inputs

Section ID	Layer Moduli (psi)			Layer Thickness (in)		
	E_{AC}	E_{GB}	$E_{Subgrade}$	AC	GB	Subgrade
N1 (GTRDry)	750,389	5,948	29,185	5.77	5.96	-
N2 (GTRWet)	985,807	6,263	26,561	5.90	6.03	-
N5 (Aramid)	1,295,658	6,564	28,990	5.59	5.95	-
N7 (Ctrl)	1,120,745	10,013	30,205	5.53	5.80	-
S5 (DryPlastic)	1,286,761	7,038	23,062	5.14	6.11	-
S6 (WetPlastic)	1,292,071	6,157	24,773	5.64	6.10	-

Figure 7.4.1 plots the peak WESLEA simulated strain response versus the average temperature-corrected 95th percentile strain response for each AG section. The line of equality is also displayed on the plot. Note that an AC layer thickness correction was not applied to the field-measured strain response data because layer thicknesses are a part of the WESLEA analysis inputs. Thus, the effect that AC layer thickness had on the strain response of each AG section was captured. The WESLEA analysis overpredicted the peak strain response of N7 (Ctrl) relative to the field-measured value. While the reason for this is not entirely clear, it may relate to the control section's higher than average in-place density (*Table 5.3.1*). This in-place density may have affected the measured strain response in a way that wasn't accounted for by the E_{AC} value alone. Regardless of this observation, the WESLEA analysis provided a reasonably accurate simulation of the field-measured strain responses for N1 (GTRDry), N2 (GTRWet), N5 (Aramid), S5 (DryPlastic), and S6 (WetPlastic), encompassing all of the sections that contained an experimental additive technology. Importantly, this layered elastic analysis accounted for the contributing effects of E_{AC}, E_{GB}, and $E_{Subgrade}$ (as well as layer thicknesses) on the peak strain response. This was unable to be done though a purely statistical analysis of the individual parameters in the previous chapter (*Figure 6.4.8*, *Figure 6.4.9*, and *Figure 6.4.10*).

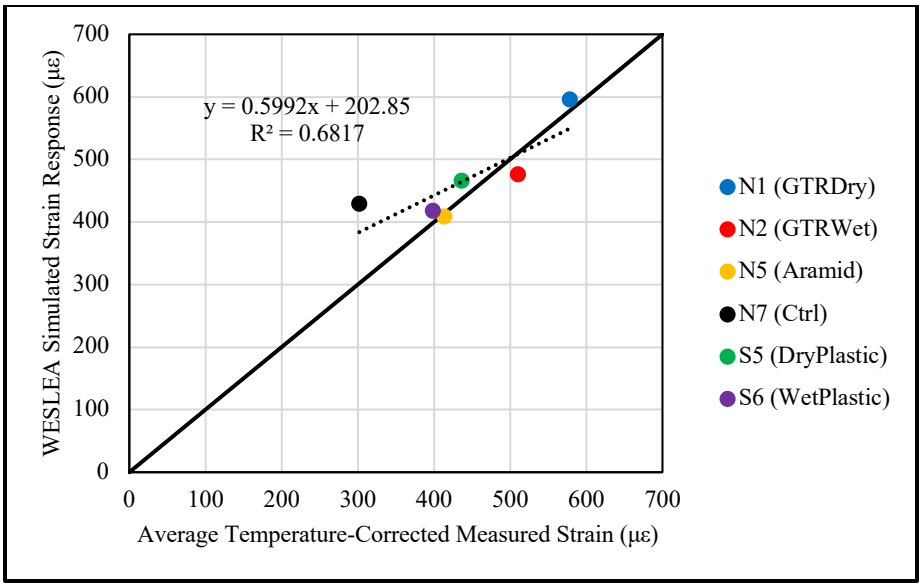

Figure 7.4.1: Strain Response: WESLEA Versus Field Measured

7.5: S_{app} Parameter and Field Cracking Relationship

One of the primary outputs of the direct tension cyclic fatigue test is S_{app}. This parameter is used to evaluate the relative fatigue performance of asphalt mixtures, therefore, its relationship with the cracking observed in the AG test sections was of interest. *Figure 7.5.1* provides a ranking of the S_{app} parameters calculated for each mixture (from highest to lowest) versus the percentage of lane area cracking. It should be noted that the cracking detected in sections N1 (GTRDry) and S5 (DryPlastic) is relatively minor so far (through June 2023) and has yet to influence IRI, FWD, or strain measurements. S5 (DryPlastic) was found to have the lowest S_{app} parameter and has subsequently displayed cracking within its test section. This result was encouraging as it indicated a connection between the of the direct tension cyclic fatigue test (laboratory) and cracking percentage (field). However, N1 (GTRDry) had the second highest S_{app} parameter, indicating it had the second-best laboratory fatigue performance. Yet, it has subsequently displayed cracking within its test section prior to N7 (Ctrl), N5 (Aramid), and S6 (WetPlastic), each of which had lower S_{app} parameter values. In fact, N1 (GTRDry) was the first AG test section to show any signs of cracking. While this finding seems to indicate a poor lab-to-field connection, it must be remembered that the laboratory evaluated S_{app} parameter only describes the fatigue performance of the asphalt mixture itself. It does not account for the other factors that contribute to field cracking, including, but not limited to, E_{GB}, $E_{Subgrade}$, or AC layer thickness. Each of these contribute to the strain response at the bottom of the AC layer, the magnitude of which primarily drives bottom-up fatigue cracking. The average measured strain response in section N1 (GTRDry) is more than double what has been measured in N7 (Ctrl). This is likely what led it to being the first test section to exhibit fatigue cracking. This investigation highlighted the limitations of correlating asphalt mixture laboratory test results and full-scale field results. That is, laboratory testing alone doesn't account for the many extraneous field conditions that influence the fatigue

performance of paved asphalt mixtures. As trafficking continues, and more AG test sections begin to display fatigue cracking, a more complete characterization of lab-to-field fatigue performance, utilizing S_{app}, will become available.

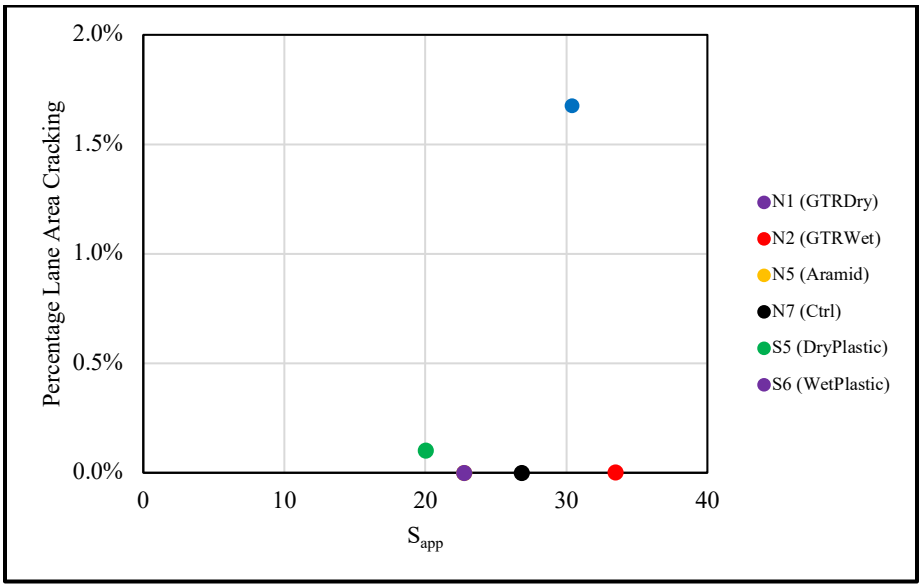

Figure 7.5.1: Percentage Lane Area Cracking Versus S_{app} Parameter

7.6: Fatigue Life Transfer Functions and Field Cracking Relationship

Laboratory beam fatigue testing resulted in fatigue life transfer functions for each AG mixture. These functions relate the applied flexural strain level to a number of cycles to failure (N_f) (*Figure 4.4.3*, *Figure 4.4.4*, *Figure 4.4.5*, and *Table 4.4.1*) and ultimately should be evaluated against measured cracking field performance. An estimation of N_f can be made given a flexural strain level input. These N_f estimations can be correlated to field cracking and may be used as predictors of test section fatigue failure. The strength of the correlation depends on the type of flexural strain input, explored in detail below.

Figure 7.6.1 displays N_f for each AG mixture, computed via their respective beam fatigue life transfer functions (in the form of *Equation 3.8.4*, using the coefficients in *Table 4.4.1*). Constant strain inputs of 600 με and 800 με were used to compute N_f. All of the AG mixtures were tested at these strain levels; therefore, they were selected for this analysis. Across both the 600 με and 800 με levels, S5 (DryPlastic) had the shortest fatigue life, while N1 (GTRDry) had the second highest. This ranking displayed a good agreement between S_{app} and N_f results (direct tension cyclic fatigue versus bending beam fatigue), however it was poorly correlated with the field observations of cracking (*Figure 7.5.1*). Similar to the S_{app} parameter, the laboratory evaluated N_f describes only the fatigue performance of the asphalt mixture, without accounting for any of the other variables (such as E_{GB}, $E_{Subgrade}$, or AC layer thickness) that contribute to the fatigue cracking of a full-scale test section.

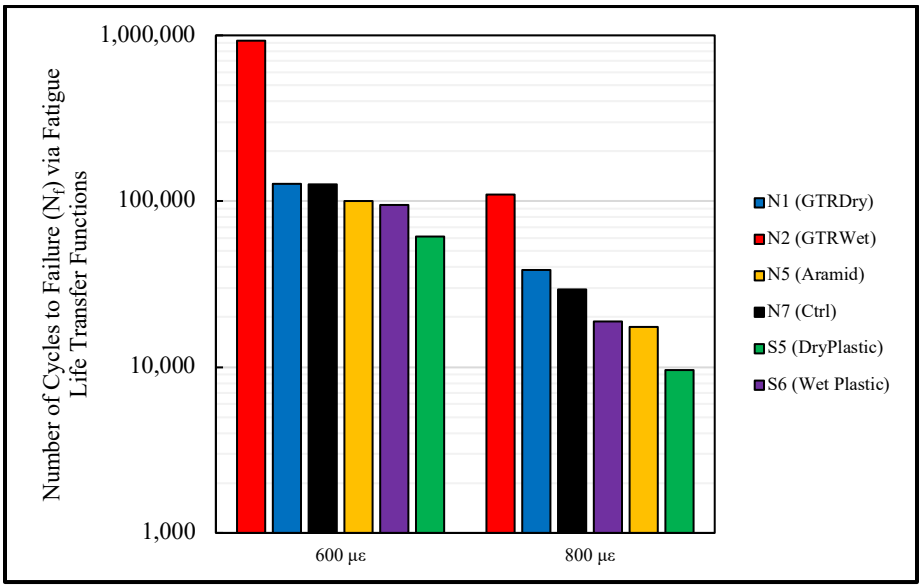

Figure 7.6.1: Fatigue Life Comparisons: Constant Strain

To overcome the deficiencies of evaluating the sections at constant strain levels, *Figure 7.6.2* displays the N_f for each AG mixture computed using its average field-measured temperature-corrected strain response. Also shown is Nf computed using the WESLEA simulated strain responses when layer thicknesses, E_{GB}, and $E_{Subgrade}$ are each held equal to N7 (Ctrl). This allowed the fatigue lives of each paved mixture to be judged in a more objective way, independent of the effects of layer thickness and foundational support. Pairing the field- measured strain response of each test section, along with that mixture's strain tolerance (individual fatigue life transfer function) resulted in the N_f values that correlated well with the observed levels of cracking thus far. N1 (GTRDry) had the lowest N_f, followed by S5 (DryPlastic). These sections have both displayed cracking in the field (*Figure 7.5.1*). When using the constant support moduli and layer thickness WESLEA simulated strain input, N1 (GTRDry) was still found to have the lowest N_f. This finding indicates that its cracking in the field is largely due to the mixture itself, and not necessarily the underlying support conditions or layer thicknesses. The N_f estimate increased for S5 (DryPlastic) and decreased for N7 (Ctrl). This finding indicated that N7 (Ctrl) was benefiting from favorable support conditions, while S5 (DryPlastic) could have been cracking earlier than expected due to its AC layer thickness (thinnest amongst all of the AG sections (*Figure 5.4.2*). Additionally, when each paved mixture was evaluated on equal footing, N2 (GTRWet) displayed the greatest N_f, indicating that it had the greatest amount of cracking resistance by a wide margin. Field cracking and the laboratory evaluated fatigue life relationships will be more fully evaluated at the conclusion of trafficking.

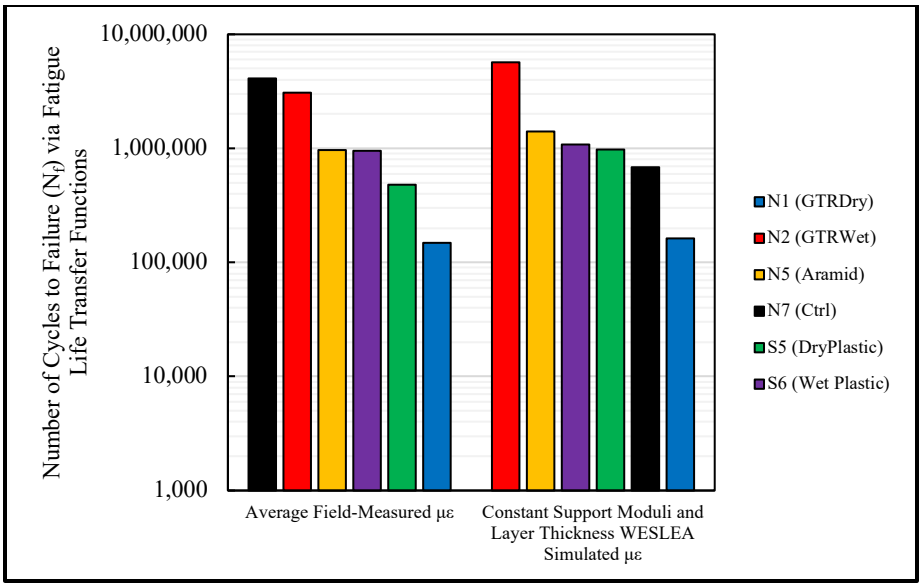

Figure 7.6.2: Fatigue Life Comparisons: Field-Measured Strain Versus Constant Support Moduli and Layer Thickness WESLEA Simulated Strain

7.7: Findings and Conclusions

This chapter investigated several connections between the results of the AG laboratory tests and the on-going, full-scale field experiment using data through June 2023. Both the average E* and the average initial flexural stiffness (evaluated at 20°C and 10 Hz) were found to correlate with the average temperature-corrected backcalculated AC modulus (E_{68}) (*Figure 7.2.1* and *Figure 7.2.2*). Both of these laboratory stiffness metrics were also found to be correlated with the average thickness- and temperature-corrected 95th percentile strain responses ($\mu\varepsilon_{cor}$) for each test section (*Figure 7.3.1* and *Figure 7.3.2*). Average Initial flexural stiffness provided the best fit with E_{68} and $\mu\varepsilon_{cor}$, likely because beam fatigue testing more accurately models the flexural loading conditions the pavement sections experience in the field.

WESLEA simulations were performed in order to quantify the peak longitudinal strain response (at the bottom of the AC layer) for each test section, while accounting for the compensatory effects of E_{AC}, E_{GB}, and $E_{Subgrade}$, and individual layer thicknesses. The resulting simulations correlated very well with field-measured strain responses (excluding N7 (Ctrl)) and demonstrated that the individual layer moduli were each influencing the peak strain response of the pavement layer (*Figure 7.4.1*). The previous attempts to statistically related E_{68}, E_{GB}, and $E_{Subgrade}$ individually with $\mu\varepsilon_{cor}$ were less successful by comparison (*Figure 6.4.8*, *Figure 6.4.9*, and *Figure 6.4.10*).

The agreement between the laboratory calculated S_{app} parameter of each asphalt mixture and the percentage of lane area cracking of the corresponding test section was found to be poor (*Figure 7.5.1*). This was likely due to the fact that the S_{app} parameter only evaluated the fatigue performance of the asphalt mixture. It was unable to account for other variables such as layer moduli and layer thickness that contribute to the strain response magnitude at the bottom of the

AC layer (known to be the primary factor driving bottom-up fatigue cracking). This exercise demonstrated the difficulties of correlating asphalt mixture laboratory test results with the measurements and observations of full-scale paved sections.

Constant strain inputs of 600 με and 800 με, as well as the average temperature-corrected 95th percentile strain response of each test section, were used as inputs into the fatigue life transfer functions of each mixture (determined from laboratory beam fatigue testing), resulting in 4 separate estimates of number of cycles to failure (N_f) (*Figure 7.6.1* and *Figure 7.6.2*). Both constant strain inputs provided poor agreement with the percentage of lane area cracking. However, utilizing the field-measured strain input provided excellent agreement with the percentage of lane area cracking. Pairing the approximate strain response of the test sections (field data) with their asphalt mixture's individual strain tolerance (lab data) resulted in the best estimate of field fatigue life. Additionally, N_f estimations independent of the differences in E_{GB}, $E_{Subgrade}$, and layer thicknesses between the test sections were made. These allowed the fatigue lives of the test sections to evaluated in the most objective way. N2 (GTRWet) was found to have the largest in-field N_f estimation, while N1 (GTRDry) had the largest. The N_f estimation for N1 (GTRDry) remained nearly unchanged when utilizing this method, indicating that the cracking seen in this section is due to the paved mixture itself rather than any effects from the supporting layer moduli or layer thicknesses. Additionally, the N_f estimation for N7 (Ctrl) decreased substantially, indicating that it was benefiting from favorable support conditions. Conversely, the N_f estimation for S5 (DryPlastic) increased. This was likely because it was the thinnest amongst all the AG sections which has contributed to the cracking seen in the field.

The field fatigue performance of asphalt mixtures could be evaluated in the future using the initial flexural stiffness and fatigue life transfer functions for each mixture determined from beam fatigue testing. For example, E_{68} could be estimated from the initial flexural stiffness value, using the relationship defined in *Figure 7.2.2*, and E_{GB}, $E_{Subgrade}$, and the layer thicknesses could be approximated. Together, these parameters would make up the necessary WESLEA inputs to provide an estimation of the peak strain response at the bottom of the AC layer. This strain level could then be used as an input into the fatigue life transfer function for the mixture (like in *Figure 7.6.2*), resulting in an estimation of N_f that predicts the field fatigue performance of the paved mixture. This method has the potential to yield an estimations of mixture field fatigue performance, without the need for the construction of full-scale test sections, saving a significant amount of resources and time.

Trafficking of the full-scale sections at the NCAT Test Track is currently ongoing and expected to be completed in 2024. The relationship investigated above will continue to be monitored as the AG test sections continue to deteriorate.

CHAPTER 8

Findings, Conclusions, and Recommendations

8.1: Summary

The AG experiment evaluated 5 additive-modified mixtures, as well as one SBS-modified control mixture, in both laboratory and field settings at the NCAT Test Track. Laboratory testing included modulus, stiffness, and phase angle characterizations of the mixtures, as well as an evaluation of their respective fatigue performance. Full-scale test sections were constructed for each mixture at the Test Track and accelerated trafficking was applied by heavy weight vehicles. Each test section was instrumented to measure the strain response of the asphalt pavement layers. AC, granular base, and subgrade moduli were backcalculated from FWD data. Rut depth, cracking, and ride quality measurements were also recorded for each test section. Relevant links between the laboratory and field-testing results were established. Additionally, a layered-elastic simulation tool was used to model the in-field conditions and simulate the strain responses of the pavement sections. Based on the data provided in this thesis, conclusions are recommendations are made in the following sections.

8.2: Laboratory Findings and Conclusions

Chapter 4 presented a comprehensive laboratory characterization of each of the AG mixtures from which the following key observations and conclusions are drawn:

- N2 (GTRWet) was found to have the lowest dynamic modulus (E*) and lowest initial flexural stiffness and (*Figure 4.2.4* and *Figure 4.4.1*). This mixture displayed the highest S_{app} parameter and fatigue life transfer function (*Figure 4.3.7* and *Figure 4.4.3*). Therefore it was concluded that this mixture had the greatest amount of laboratory-evaluated fatigue resistance.
- Conversely, S5 (DryPlastic) was found to have the highest dynamic modulus (E*) and highest initial flexural stiffness and (*Figure 4.2.6* and *Figure 4.4.1*). This mixture also displayed the lowest S_{app} parameter and fatigue life transfer function (*Figure 4.3.7* and *Figure 4.4.5*). Therefore, it was concluded that this mixture had the least amount of laboratory-evaluated fatigue resistance.
- The findings regarding the wet rubber and dry plastic modifiers were expected and were consistent with what is commonly understood about these additive types.
- The other AG mixtures, including N1 (GTRDry), N5 (Aramid), N7 (Ctrl), and S6 (WetPlastic) fell in between the wet rubber and dry plastic modified mixtures in terms of their stiffness and fatigue characteristics.

8.3: Field Findings

Chapter 6 presented the pavement strain responses, backcalculated layer moduli, and performance data that were collected for the AG sections. The data presented in this thesis were collected through June 2023, while trafficking of the test sections is expected to be completed in the Spring of 2024. The following key observations and conclusions are made:

- None of the AG test sections displayed significant changes in their average measured IRI with trafficking (*Figure 6.2.1*, *Figure 6.2.2*, and *Figure 6.2.3*), and all displayed similar levels of rutting (well below the allowable threshold) (*Figure 6.2.4*, *Figure 6.2.5*, and *Figure 6.2.6*).
- Through June 2023, sections N1 (GTRDry) and S5 (DryPlastic) were the only to experience any percentage of cracking (*Figure 6.2.7* and *Figure 6.2.8*).
- The cracking measured in N1 (GTRDry) was likely due to the high values of measured strain (*Figure 6.4.7*) which were caused by the mixture's reduced stiffness (reflected by its low E_{68}), coupled with the mixture's average strain tolerance (*Figure 4.4.3*) evaluated in the laboratory.
- The cracking measured in S5 (DryPlastic) was likely caused by the mixture's strain tolerance, which was the lowest amongst all mixtures (*Figure 4.4.5*) evaluated in the laboratory.

8.4: Combined Analysis Findings and Conclusions

Chapter 7 detailed the connections that were established between the laboratory and field data, as well as the results of the WESLEA simulations. Further relationships between the laboratory and field data will be established once the full trafficking of the test sections is completed in the Spring of 2024. Based on the data and ensuing analysis, the following key observations are conclusions are drawn:

- Initial flexural stiffness (obtained from the bending beam fatigue test) was found to correlate well with E_{68} and $\mu\varepsilon_{cor}$ in comparison to dynamic modulus (E*) (*Figure 7.2.2* and *Figure 7.3.2*). It was concluded that this was because beam fatigue applies a flexural strain to the test specimens, as opposed to an axial strain, and better replicates the loading conditions in the field.
- WESLEA simulations were performed to quantify the peak longitudinal strain response (at the bottom of the AC layer) for each test section, while accounting for the compensatory effects of E_{AC}, E_{GB}, and $E_{Subgrade}$, and individual layer thicknesses (*Figure 7.4.1*). This was done because the previous attempts to statistically relate E_{68}, E_{GB}, and $E_{Subgrade}$ individually with $\mu\varepsilon_{cor}$ in Chapter 6 were largely unsuccessful (*Figure 6.4.8*, *Figure 6.4.9*, and *Figure 6.4.10*).
- Excluding N7 (Ctrl), the resulting WESLEA simulations correlated very well with field-measured strain responses and demonstrated that the individual layer moduli were each influencing the peak strain response of the pavement layer.

- The agreement between the S_{app} parameter (a primary output of the direct tension cyclic fatigue test) and the measured field cracking of thee test sections was analyzed. It was found that there was poor agreement between these two factors, despite the S_{app} being an indicator of mixture fatigue performance (*Figure 7.5.1*).
- While no conclusions could be made as of June, 2023, the poor predictive capability of S_{app} could be attributed to its inability to account for other variables in the field, such as layer moduli and layer thickness, that contribute to the strain response of the pavement (known to be the primary factor driving bottom-up fatigue cracking). This exercise also demonstrated the difficulties of correlating any asphalt mixture laboratory test result with the measurements and observations of full-scale paved sections.
- As trafficking continues, and the test sections begin to develop more severe distresses, a stronger relationship between Sapp and field cracking may emerge.
- When using the bending beam fatigue testing transfer functions with constant strain inputs of 600 με and 800 με, poor agreement was found between N_f estimations the observed cracking in the field (*Figure 7.6.1*).
- It was concluded that using the average field-measured strain response of the test sections as an input into the fatigue life transfer functions resulted in the best estimations of field fatigue life (*Figure 7.6.2*).
- When N_f was estimated using WESLEA simulated strain responses with constant E_{GB}, $E_{Subgrade}$, layer thicknesses values, and section-specific AC moduli, it allowed the fatigue lives of the test sections to evaluated in a more objective way with the following findings.
    - N1 (GTRDry) was still found to have the lowest N_f estimate, indicating that the cracking observed in the field was not due to external factors (such as support conditions or layer thicknesses), but rather the paved mixture itself.
    - The N_f estimation for N7 (Ctrl) decreased substantially, indicating that it was benefiting from favorable support conditions.
    - Conversely, the Nf estimation for S5 (DryPlastic) increased. This was likely because it was the thinnest amongst all the AG sections which has contributed to its cracking.

8.5: Recommendations

It is recommended that a form of stress-controlled flexural beam testing be added to the available suite of laboratory tests. This would allow for the stiffness and fatigue characteristics of the asphalt mixtures to be evaluated simultaneously. Currently, strain-controlled flexural beam testing does not allow for this type of analysis. A stress-controlled testing mode could potentially result in better correlations between laboratory evaluated fatigue performance and bottom-up fatigue cracking full-scale test sections. It could also eliminate the need for WESLEA simulated fatigue life transfer function strain inputs, as the strain response of the beam fatigue samples themselves could be measured directly.

It is recommended that further strain and/or fatigue cracking modeling be conducted. Alternative simulation tools may present better correlations between the laboratory evaluated fatigue

performance of the asphalt mixtures and bottom-up fatigue cracking full-scale test sections. For example, PerRoad, a program that couples layered elastic analysis with Monte Carlo simulation, could be utilized as an alternative to simulate the peak longitudinal strain response at the bottom of the AC layers. Additionally, FlexPAVE, a program that uses a viscoelastic design method, could be used to simulate the number of cycles to failure (N_f) for each AG mixture. This N_f result could be compared to those detailed within this thesis.

It is recommended that additional additive technologies, as well as different mixture designs, be evaluated within the framework of the AG experiment.

8.6: Plans for Future Research

As has been mentioned previously, trafficking of the full-scale test sections is expected to be completed in the Spring of 2024. Further investigations linking the laboratory and field results will be able to be made once the data becomes available. The primary goal of the AG experiment as a whole is to establish a framework for the rapid evaluation of new and existing additive types. This framework will begin to be established by the NCAT research team once trafficking has been completed.

REFERENCES

Abdalfattah, I. A., W. S. Mogawer, and K. Stuart. Recycled polyethylene (RPE) modified asphalt mixtures: Performance predictions using pavement Mechanistic-Empirical design and evaluation of return on investment. *Construction and Building Materials,* Vol. 356, 2022.

ACE XP Polymer. Surface Tech. (2023). https://surface-tech.com/ace-xp/

Dantas, S., M. Farias, L. G. Mello, P. Pereira, and J. Pais. *The use of crumb rubber in asphalt mixtures using the dry process*. 2005.

Ding, J., Y. D. Wang, S. Gulzar, Y. R. Kim, and B. S. Underwood. Uncertainty Quantification of Simplified Viscoelastic Continuum Damage Fatigue Model using the Bayesian Inference-Based Markov Chain Monte Carlo Method. *Transportation Research Record*, 2674(4), 2020, pp. 247–260

Feiteira Dias, J. L., L. G. Picado-Santos, and S. D. Capitão. Mechanical performance of dry process fine crumb rubber asphalt mixtures placed on the Portuguese road network. *Construction and Building Materials,* Vol. 73, 2014, pp. 247-254.

Foshee, M.M. *Early Characterization and Performance of Flexible Pavements Utilizing Asphalt Additives*. Doctoral dissertation, Auburn University, 2022.

Hasheminejad, N., C. Vuye, A. Margaritis, W. Van den bergh, J. Dirckx, and S. Vanlanduit. Characterizing the Complex Modulus of Asphalt Concrete Using a Scanning Laser Doppler Vibrometer. *Materials*, Vol. 12, No. 21, 2019, p. 3542.

Jin, D., D. Ge, J. Wang, L. Malburg, and Z. You. Reconstruction of Asphalt Pavements with Crumb Rubber Modified Asphalt Mixture in Cold Region: Material Characterization, Construction, and Performance. *Materials, No. 16*, 2023.

Zhang J. and L. Bao. Determination of asphalt mixture's viscoelastic constitutive parameters for pavement response analysis using dynamic modulus transformation, *Construction and Building Materials*, Volume 315, 2022.

Kaloush, K. E., W. A. Zeiada, K. P. Biligiri, M. C. Rodezno, and J. Reed. *Evaluation of Fiber-Reinforced Asphalt Mixtures Using Advanced Material Characterization Tests*. Arizona State University, 2010.

Mamlouk, M., M. Souliman, W. Zeiada, and K. Kaloush. Refining HMA Beam Fatigue Testing Conditions. *Advances in Civil Engineering*, 1, 2012.

Mateos, A. and J. Harvey. Laboratory Evaluation of the Mechanical Properties of Asphalt Concrete Reinforced with Aramid Synthetic Fibers. University of California, Davis: Institute of Transportation Studies, 2019.

Noorvand, H., R. Salim, J. Medina, J. Stempihar, and B. S. Underwood. Effect of Synthetic Fiber State on Mechanical Performance of Fiber Reinforced Asphalt Concrete. *Transportation Research Record,* Vol. 2672, No. 28, 2018, pp. 42-51.

Queiroz, R. F. R., J. K. G. Rodrigues, J. D. Patricio, P. H. d. Silva, J. R. Carvalho, O. d. M. Melo Neto, L. G. Rodrigues, and R. K. B. d. Lima. Linear viscoelastic properties and fatigue S-VECD based evaluation of polymer-modified asphalt mixtures. Journal of Building Engineering, Vol. 75, 2023.

Raad, L., S. Saboundjian, and J. W. Corcoran. Remaining Fatigue Life Analysis: Comparison Between Dense-Graded Conventional Asphalt Concrete and Gap-Graded Asphalt-Rubber Hot Mix. *Transportation Research Record*, No. 1388, 1993, pp. 97-107.

"Research Needed on Using Recycled Plastics in Asphalt". 2021. www.eng.auburn.edu/research/centers/ncat/newsroom/2019-fall/plastics.html.

Spadoni, S., L. Paolo Ingrassia, D. Mocelin, Y. R. Kim, and F. Canestrari. Comparison of asphalt mixtures containing polymeric compounds and polymer-modified bitumen based on the VECD theory. *Construction and Building Materials*, Vol. 349, 2022.

"Scrap Tires in Asphalt". Asphalt Pavement Association of New Mexico, 2021. Apanm.org/scrap-tires-in-asphalt/.

"SmartMix". Liberty Tire, 2021. libertytire.com/our-product/smartmix/.

Taylor, A. J. *Mechanistic Characterization of Resilient Moduli for Unbound Pavement Layer Materials*. Doctoral dissertation, Auburn University, 2008.

Timm, D.H. *Design, Construction, and Instrumentation of the 2006 Test Track Structural Study*. Report No. 09-01, National Center for Asphalt Technology, Auburn University, 2009.

Timm, D.H., F. Yin, N. Tran, M.M. Foshee, C. Rodezno, "Comparison of Relative Structural Characterization Methods for Additive-Modified Asphalt Mixtures," Transportation Research Record, Vol. 2676 (11), Transportation Research Board, pp. 676-688, 2022.

Timm, D. H., & Priest, A. L. *Material properties of the 2003 NCAT test track structural study*. Report No. 06-01, National Center for Asphalt Technology, Auburn University, 2006.

Timm, D. H., & Tutu, K. A. Determination of an optimum backcalculation cross section for unconventional pavement profiles. *Transportation Research Record*, Vol. 2641, No. 1, 2017, pp. 48-57.

Xie, Z., and J. Shen. Performance properties of rubberized stone matrix asphalt mixtures produced through different processes. *Construction and Building Materials*, Vol. 104, 2016, pp. 230-234.

Yin, F. "LLDPE-rich PCR Sample_Picture1". Photo, 2022.

Zeiada, W. A., B. S. Underwood, T. Pourshams, J. Stempihar, and K. E. Kaloush. Comparison of conventional, polymer, and rubber asphalt mixtures using viscoelastic continuum damage model. *Road Materials and Pavement Design,* Vol. 15, No. 3, 2014, pp. 588-605.

Zhang, J., H. Li, P. Liu, M. Liang, H. Jiang, Z. Yao, and G. Airey. Experimental Exploration of Influence of Recycled Polymer Components on Rutting Resistance and Fatigue Behavior of Asphalt Mixtures. *Journal of Materials in Civil Engineering,* Vol. 32, No. 6, 2020.

APPENDIX

A.1: Dynamic Modulus (E) ANOVA and Tukey Kramer Analysis*

Table A.1.1: Dynamic Modulus (E) ANOVA*

Testing Frequency	Testing Temperature	N1 (GTRDry)	N2 (GTRWet)	N5 (Aramid)	N7 (Ctrl)	S5 (DryPlastic)	S6 (WetPlastic)	Variation	Sum of Squares	Degrees of Freedom	Mean Squares	F	$F_{critical}$
0.1 Hz	4 °C	6,995	6,268	8,013	8,184	9,338	8,276	Between Groups	14,594,064	5	2,918,813	30.45	3.11
		7,124	6,977	8,165	8,181	9,318	7,869	Within Groups	1,150,423	12	95,869		
		7,042	6,525	9,170	8,303	9,302	8,046	Total	15,744,487	17			
	20 °C	2,111	1,932	2,236	2,415	3,360	2,192	Between Groups	3,756,039	5	751,208	33.28	3.11
		2,328	2,215	2,217	2,182	3,422	1,945	Within Groups	270,897	12	22,575		
		2,075	1,985	2,636	2,157	3,324	2,048	Total	4,026,936	17			
	40 °C	349	324	262	283	522	266	Between Groups	157,400	5	31,480	38.83	3.11
		361	400	280	248	523	210	Within Groups	9,729	12	811		
		337	337	328	220	503	229	Total	167,129	17			
1 Hz	4 °C	9,695	8,625	11,060	11,188	11,954	11,233	Between Groups	19,510,305	5	3,902,061	29.70	3.11
		9,781	9,404	11,169	11,262	11,912	10,820	Within Groups	1,576,529	12	131,377		
		9,849	8,876	12,423	11,356	11,917	11,054	Total	21,086,834	17			
	20 °C	3,823	3,470	4,245	4,475	5,570	4,193	Between Groups	7,028,539	5	1,405,708	28.08	3.11
		4,166	3,828	4,232	4,195	5,630	3,809	Within Groups	600,826	12	50,069		
		3,785	3,513	4,907	4,180	5,494	3,990	Total	7,629,365	17			
	40 °C	837	764	703	776	1,265	723	Between Groups	658,068	5	131,614	35.54	3.11
		865	913	743	680	1,270	608	Within Groups	44,436	12	3,703		
		828	796	858	654	1,197	652	Total	702,504	17			
10 Hz	4 °C	12,665	11,225	14,155	14,360	14,568	14,257	Between Groups	23,406,054	5	4,681,211	28.46	3.11
		12,802	12,057	14,291	14,481	14,545	13,859	Within Groups	1,974,139	12	164,512		
		12,902	11,456	15,708	14,508	14,545	14,149	Total	25,380,194	17			
	20 °C	6,229	5,647	6,995	7,270	8,245	6,962	Between Groups	10,720,537	5	2,144,107	25.34	3.11
		6,676	6,030	6,993	7,012	8,301	6,470	Within Groups	1,015,447	12	84,621		
		6,212	5,664	7,947	6,982	8,186	6,727	Total	11,735,984	17			
	40 °C	1,844	1,655	1,754	1,868	2,692	1,787	Between Groups	1,933,427	5	386,685	33.14	3.11
		1,905	1,886	1,831	1,695	2,691	1,576	Within Groups	140,001	12	11,667		
		1,830	1,728	2,065	1,685	2,552	1,672	Total	2,073,428	17			

Table A.1.2: Dynamic Modulus (E) Tukey Kramer Analysis*

Testing Frequency	Testing Temperature	Comparison		Absolute Difference	Critical Range				
0.1 Hz	4 °C	N1	N2	464	849	Equal	N1	7,054	C
		N1	N5	1396	849	Different	N2	6,590	C
		N1	N7	1169	849	Different	N5	8,449	B
		N1	S5	2266	849	Different	N7	8,223	B
		N1	S6	1010	849	Different	S5	9,319	A
		N2	N5	1859	849	Different	S6	8,064	B
		N2	N7	1633	849	Different			
		N2	S5	2729	849	Different			
		N2	S6	1474	849	Different			
		N5	N7	227	849	Equal			
		N5	S5	870	849	Different			
		N5	S6	386	849	Equal			
		N7	S5	1097	849	Different			
		N7	S6	159	849	Equal			
		S5	S6	1256	849	Different			
	20 °C	N1	N2	127	412	Equal	N1	2,171	B
		N1	N5	192	412	Equal	N2	2,044	B
		N1	N7	80	412	Equal	N5	2,363	B
		N1	S5	1197	412	Different	N7	2,251	B
		N1	S6	110	412	Equal	S5	3,369	A
		N2	N5	319	412	Equal	S6	2,062	B
		N2	N7	207	412	Equal			
		N2	S5	1325	412	Different			
		N2	S6	18	412	Equal			
		N5	N7	112	412	Equal			
		N5	S5	1006	412	Different			
		N5	S6	301	412	Equal			
		N7	S5	1117	412	Different			
		N7	S6	190	412	Equal			
		S5	S6	1307	412	Different			
	40 °C	N1	N2	5	78	Equal	N1	349	B
		N1	N5	59	78	Equal	N2	354	B
		N1	N7	98	78	Different	N5	290	BC
		N1	S5	167	78	Different	N7	250	C
		N1	S6	114	78	Different	S5	516	A
		N2	N5	63	78	Equal	S6	235	C
		N2	N7	103	78	Different			
		N2	S5	163	78	Different			
		N2	S6	119	78	Different			
		N5	N7	40	78	Equal			
		N5	S5	226	78	Different			
		N5	S6	55	78	Equal			
		N7	S5	266	78	Different			
		N7	S6	15	78	Equal			
		S5	S6	281	78	Different			

Table A.1.2: Dynamic Modulus (E) Tukey Kramer Analysis*

1 Hz	4 °C	N1	N2	807	994	Equal	N1	9,775	B
		N1	N5	1776	994	Different	N2	8,968	B
		N1	N7	1494	994	Different	N5	11,551	A
		N1	S5	2153	994	Different	N7	11,269	A
		N1	S6	1261	994	Different	S5	11,928	A
		N2	N5	2582	994	Different	S6	11,036	A
		N2	N7	2300	994	Different			
		N2	S5	2959	994	Different			
		N2	S6	2067	994	Different			
		N5	N7	282	994	Equal			
		N5	S5	377	994	Equal			
		N5	S6	515	994	Equal			
		N7	S5	659	994	Equal			
		N7	S6	233	994	Equal			
		S5	S6	892	994	Equal			
	20 °C	N1	N2	321	613	Equal	N1	3,925	BC
		N1	N5	537	613	Equal	N2	3,604	C
		N1	N7	359	613	Equal	N5	4,461	B
		N1	S5	1640	613	Different	N7	4,283	B
		N1	S6	73	613	Equal	S5	5,565	A
		N2	N5	858	613	Different	S6	3,997	BC
		N2	N7	680	613	Different			
		N2	S5	1961	613	Different			
		N2	S6	394	613	Equal			
		N5	N7	178	613	Equal			
		N5	S5	1103	613	Different			
		N5	S6	464	613	Equal			
		N7	S5	1281	613	Different			
		N7	S6	286	613	Equal			
		S5	S6	1567	613	Different			
	40 °C	N1	N2	19	167	Equal	N1	844	B
		N1	N5	75	167	Equal	N2	824	BC
		N1	N7	140	167	Equal	N5	768	BC
		N1	S5	401	167	Different	N7	703	BC
		N1	S6	182	167	Different	S5	1,244	A
		N2	N5	56	167	Equal	S6	661	C
		N2	N7	121	167	Equal			
		N2	S5	420	167	Different			
		N2	S6	163	167	Equal			
		N5	N7	65	167	Equal			
		N5	S5	476	167	Different			
		N5	S6	107	167	Equal			
		N7	S5	541	167	Different			
		N7	S6	42	167	Equal			
		S5	S6	583	167	Different			

Table A.1.2: Dynamic Modulus (E) Tukey Kramer Analysis*

		N1	N2	1210	1112	Different	N1	12,790	B
		N1	N5	1928	1112	Different	N2	11,579	C
		N1	N7	1660	1112	Different	N5	14,718	A
		N1	S5	1763	1112	Different	N7	14,450	A
		N1	S6	1299	1112	Different	S5	14,553	A
		N2	N5	3139	1112	Different	S6	14,088	A
		N2	N7	2870	1112	Different			
	4 °C	N2	S5	2973	1112	Different			
		N2	S6	2509	1112	Different			
		N5	N7	268	1112	Equal			
		N5	S5	165	1112	Equal			
		N5	S6	630	1112	Equal			
		N7	S5	103	1112	Equal			
		N7	S6	361	1112	Equal			
		S5	S6	464	1112	Equal			
		N1	N2	592	797	Equal	N1	6,372	CD
		N1	N5	939	797	Different	N2	5,780	D
		N1	N7	716	797	Equal	N5	7,312	B
		N1	S5	1872	797	Different	N7	7,088	BC
		N1	S6	347	797	Equal	S5	8,244	A
		N2	N5	1531	797	Different	S6	6,720	BC
		N2	N7	1308	797	Different			
10 Hz	20 °C	N2	S5	2464	797	Different			
		N2	S6	939	797	Different			
		N5	N7	224	797	Equal			
		N5	S5	932	797	Different			
		N5	S6	592	797	Equal			
		N7	S5	1156	797	Different			
		N7	S6	368	797	Equal			
		S5	S6	1524	797	Different			
		N1	N2	103	296	Equal	N1	1,860	B
		N1	N5	24	296	Equal	N2	1,756	B
		N1	N7	110	296	Equal	N5	1,883	B
		N1	S5	785	296	Different	N7	1,749	B
		N1	S6	181	296	Equal	S5	2,645	A
		N2	N5	127	296	Equal	S6	1,678	B
		N2	N7	7	296	Equal			
	40 °C	N2	S5	889	296	Different			
		N2	S6	78	296	Equal			
		N5	N7	134	296	Equal			
		N5	S5	762	296	Different			
		N5	S6	205	296	Equal			
		N7	S5	896	296	Different			
		N7	S6	71	296	Equal			
		S5	S6	967	296	Different			

A.2: Phase Angle ANOVA and Tukey Kramer Analysis

Table A.2.1: Phase Angle ANOVA

Testing Frequency	Testing Temperature	N1 (GTRDry)	N2 (GTRWet)	N5 (Aramid)	N7 (Ctrl)	S5 (DryPlastic)	S6 (WetPlastic)	Variation	Sum of Squares	Degrees of Freedom	Mean Squares	F	$F_{critical}$
0.1 Hz	4 °C	15.1	14.4	14.9	14.4	11.5	14.3	Between Groups	29.06	5	5.81	48.12	3.11
		15.2	13.6	14.8	15.0	11.5	15.0	Within Groups	1.45	12	0.12		
		15.4	14.5	14.2	15.0	11.3	15.1	Total	30.51	17			
	20 °C	27.0	27.4	28.9	27.8	24.2	30.4	Between Groups	100.20	5	20.04	26.77	3.11
		27.0	25.4	30.6	30.0	23.8	31.7	Within Groups	8.98	12	0.75		
		27.8	26.8	29.1	30.2	23.7	31.5	Total	109.19	17			
	40 °C	31.1	30.7	34.6	32.7	32.8	33.3	Between Groups	22.36	5	4.47	5.64	3.11
		32.2	30.3	31.6	33.1	33.4	34.1	Within Groups	9.51	12	0.79		
		31.6	31.1	31.9	34.5	33.5	34.5	Total	31.87	17			
1 Hz	4 °C	11.8	11.5	11.4	11.0	9.0	10.9	Between Groups	16.92	5	3.38	72.49	3.11
		12.2	11.0	11.2	11.5	9.0	11.3	Within Groups	0.56	12	0.05		
		12.1	11.4	11.0	11.5	8.8	11.3	Total	17.48	17			
	20 °C	22.1	22.2	23.1	22.5	18.5	23.9	Between Groups	72.49	5	14.50	35.52	3.11
		22.1	20.9	23.8	24.2	18.3	25.1	Within Groups	4.90	12	0.41		
		22.8	22.0	22.9	24.4	18.3	24.9	Total	77.39	17			
	40 °C	30.7	30.0	35.3	32.2	31.7	34.1	Between Groups	47.48	5	9.50	14.36	3.11
		32.0	29.1	33.5	33.4	31.9	35.3	Within Groups	7.94	12	0.66		
		31.1	30.8	32.9	34.0	32.3	35.0	Total	55.42	17			
10 Hz	4 °C	9.5	9.3	8.8	8.6	7.2	8.6	Between Groups	11.89	5	2.38	126.33	3.11
		9.9	9.2	8.7	8.9	7.2	8.8	Within Groups	0.23	12	0.02		
		9.8	9.3	8.7	8.9	7.0	8.6	Total	12.11	17			
	20 °C	17.5	17.4	17.6	17.2	13.9	17.9	Between Groups	40.31	5	8.06	52.10	3.11
		17.3	16.8	17.6	18.4	13.8	18.7	Within Groups	1.86	12	0.15		
		17.9	17.4	17.3	18.5	13.8	18.6	Total	42.17	17			
	40 °C	29.3	28.4	33.2	31.7	28.0	32.6	Between Groups	83.07	5	16.61	38.37	3.11
		29.9	27.6	32.2	32.9	28.0	34.0	Within Groups	5.20	12	0.43		
		29.5	28.8	31.6	33.5	28.3	33.6	Total	88.26	17			

Table A.2.2: Phase Angle Tukey Kramer Analysis

Testing Frequency	Testing Temperature	Comparison		Absolute Difference	Critical Range				
0.1 Hz	4 °C	N1	N2	1.07	0.95	Different	N1	15.24	A
		N1	N5	0.61	0.95	Equal	N2	14.17	B
		N1	N7	0.43	0.95	Equal	N5	14.63	B
		N1	S5	3.82	0.95	Different	N7	14.81	AB
		N1	S6	0.45	0.95	Equal	S5	11.42	C
		N2	N5	0.46	0.95	Equal	S6	14.79	AB
		N2	N7	0.64	0.95	Equal			
		N2	S5	2.74	0.95	Different			
		N2	S6	0.62	0.95	Equal			
		N5	N7	0.18	0.95	Equal			
		N5	S5	3.21	0.95	Different			
		N5	S6	0.16	0.95	Equal			
		N7	S5	3.38	0.95	Different			
		N7	S6	0.02	0.95	Equal			
		S5	S6	3.36	0.95	Different			
	20 °C	N1	N2	0.77	2.37	Equal	N1	27.30	BC
		N1	N5	2.21	2.37	Equal	N2	26.53	C
		N1	N7	2.02	2.37	Equal	N5	29.51	AB
		N1	S5	3.38	2.37	Different	N7	29.32	AB
		N1	S6	3.88	2.37	Different	S5	23.92	D
		N2	N5	2.98	2.37	Different	S6	31.18	A
		N2	N7	2.79	2.37	Different			
		N2	S5	2.61	2.37	Different			
		N2	S6	4.64	2.37	Different			
		N5	N7	0.19	2.37	Equal			
		N5	S5	5.59	2.37	Different			
		N5	S6	1.67	2.37	Equal			
		N7	S5	5.40	2.37	Different			
		N7	S6	1.85	2.37	Equal			
		S5	S6	7.26	2.37	Different			
	40 °C	N1	N2	0.95	2.44	Equal	N1	31.63	AB
		N1	N5	1.06	2.44	Equal	N2	30.68	B
		N1	N7	1.79	2.44	Equal	N5	32.69	AB
		N1	S5	1.58	2.44	Equal	N7	33.42	A
		N1	S6	2.30	2.44	Equal	S5	33.21	A
		N2	N5	2.01	2.44	Equal	S6	33.93	A
		N2	N7	2.74	2.44	Different			
		N2	S5	2.53	2.44	Different			
		N2	S6	3.25	2.44	Different			
		N5	N7	0.73	2.44	Equal			
		N5	S5	0.52	2.44	Equal			
		N5	S6	1.25	2.44	Equal			
		N7	S5	0.21	2.44	Equal			
		N7	S6	0.51	2.44	Equal			
		S5	S6	0.73	2.44	Equal			

Table A.2.2: Phase Angle Tukey Kramer Analysis

1 Hz	4 °C	N1	N2	0.72	0.59	Different	N1	12.02	A
		N1	N5	0.83	0.59	Different	N2	11.30	B
		N1	N7	0.68	0.59	Different	N5	11.19	B
		N1	S5	3.10	0.59	Different	N7	11.34	B
		N1	S6	0.88	0.59	Different	S5	8.92	C
		N2	N5	0.11	0.59	Equal	S6	11.14	B
		N2	N7	0.04	0.59	Equal			
		N2	S5	2.38	0.59	Different			
		N2	S6	0.16	0.59	Equal			
		N5	N7	0.15	0.59	Equal			
		N5	S5	2.27	0.59	Different			
		N5	S6	0.05	0.59	Equal			
		N7	S5	2.42	0.59	Different			
		N7	S6	0.20	0.59	Equal			
		S5	S6	2.22	0.59	Different			
	20 °C	N1	N2	0.66	1.75	Equal	N1	22.35	B
		N1	N5	0.93	1.75	Equal	N2	21.69	B
		N1	N7	1.37	1.75	Equal	N5	23.27	AB
		N1	S5	3.98	1.75	Different	N7	23.72	A
		N1	S6	2.27	1.75	Different	S5	18.37	C
		N2	N5	1.59	1.75	Equal	S6	24.62	A
		N2	N7	2.03	1.75	Different			
		N2	S5	3.32	1.75	Different			
		N2	S6	2.93	1.75	Different			
		N5	N7	0.44	1.75	Equal			
		N5	S5	4.91	1.75	Different			
		N5	S6	1.34	1.75	Equal			
		N7	S5	5.35	1.75	Different			
		N7	S6	0.90	1.75	Equal			
		S5	S6	6.25	1.75	Different			
	40 °C	N1	N2	1.31	2.23	Equal	N1	31.27	BC
		N1	N5	2.63	2.23	Different	N2	29.96	C
		N1	N7	1.93	2.23	Equal	N5	33.91	A
		N1	S5	0.71	2.23	Equal	N7	33.21	AB
		N1	S6	3.49	2.23	Different	S5	31.98	BC
		N2	N5	3.95	2.23	Different	S6	34.76	A
		N2	N7	3.25	2.23	Different			
		N2	S5	2.02	2.23	Equal			
		N2	S6	4.80	2.23	Different			
		N5	N7	0.70	2.23	Equal			
		N5	S5	1.93	2.23	Equal			
		N5	S6	0.86	2.23	Equal			
		N7	S5	1.23	2.23	Equal			
		N7	S6	1.56	2.23	Equal			
		S5	S6	2.78	2.23	Different			

Table A.2.2: Phase Angle Tukey Kramer Analysis

10 Hz	4 °C	N1	N2	0.48	0.38	Different	N1	9.74	A
		N1	N5	1.01	0.38	Different	N2	9.26	B
		N1	N7	0.92	0.38	Different	N5	8.73	C
		N1	S5	2.64	0.38	Different	N7	8.82	C
		N1	S6	1.10	0.38	Different	S5	7.11	D
		N2	N5	0.53	0.38	Different	S6	8.64	C
		N2	N7	0.44	0.38	Different			
		N2	S5	2.16	0.38	Different			
		N2	S6	0.62	0.38	Different			
		N5	N7	0.09	0.38	Equal			
		N5	S5	1.63	0.38	Different			
		N5	S6	0.09	0.38	Equal			
		N7	S5	1.72	0.38	Different			
		N7	S6	0.18	0.38	Equal			
		S5	S6	1.54	0.38	Different			
	20 °C	N1	N2	0.35	1.08	Equal	N1	17.55	AB
		N1	N5	0.09	1.08	Equal	N2	17.20	B
		N1	N7	0.46	1.08	Equal	N5	17.47	AB
		N1	S5	3.70	1.08	Different	N7	18.01	AB
		N1	S6	0.85	1.08	Equal	S5	13.85	C
		N2	N5	0.27	1.08	Equal	S6	18.40	A
		N2	N7	0.81	1.08	Equal			
		N2	S5	3.35	1.08	Different			
		N2	S6	1.20	1.08	Different			
		N5	N7	0.54	1.08	Equal			
		N5	S5	3.62	1.08	Different			
		N5	S6	0.94	1.08	Equal			
		N7	S5	4.16	1.08	Different			
		N7	S6	0.39	1.08	Equal			
		S5	S6	4.55	1.08	Different			
	40 °C	N1	N2	1.36	1.80	Equal	N1	29.59	B
		N1	N5	2.70	1.80	Different	N2	28.23	B
		N1	N7	3.11	1.80	Different	N5	32.29	A
		N1	S5	1.50	1.80	Equal	N7	32.70	A
		N1	S6	3.77	1.80	Different	S5	28.10	B
		N2	N5	4.06	1.80	Different	S6	33.36	A
		N2	N7	4.47	1.80	Different			
		N2	S5	0.14	1.80	Equal			
		N2	S6	5.13	1.80	Different			
		N5	N7	0.41	1.80	Equal			
		N5	S5	4.19	1.80	Different			
		N5	S6	1.07	1.80	Equal			
		N7	S5	4.60	1.80	Different			
		N7	S6	0.66	1.80	Equal			
		S5	S6	5.26	1.80	Different			

A.3: Initial Flexural Stiffness ANOVA and Tukey Kramer Analysis

Table A.3.1: Initial Flexural Stiffness ANOVA

N1 (GTRDry)	N2 (GTRWet)	N5 (Aramid)	N7 (Ctrl)	S5 (DryPlastic)	S6 (Wet Plastic)	Variation	Sum of Squares	Degrees of Freedom	Mean Squares	F	$F_{critical}$
4,805	4,073	5,683	5,764	6,466	5,322	Between Groups	28,540,304	5	5,708,061	33.18	2.41
4,922	3,987	5,857	5,551	6,206	5,221	Within Groups	8,257,920	48	172,040		
4,724	3,798	5,320	5,840	6,035	5,482	Total	36,798,225	53			
4,654	3,545	5,464	5,691	6,080	5,417						
4,623	4,056	3,435	4,700	5,615	5,044						
4,285	3,827	5,321	5,683	6,199	5,394						
4,038	3,482	5,494	5,503	6,397	5,053						
4,049	3,567	5,276	5,188	5,538	4,563						
3,840	3,681	5,417	5,082	5,800	5,095						

Table A.3.2: Initial Flexural Stiffness Tukey Kramer Analysis

Comparison		Absolute Difference	Critical Range				
N1	N2	658	580	Different	N1	4,438	C
N1	N5	814	580		N2	3,780	D
N1	N7	1,007	580	Different	N5	5,252	B
N1	S5	1,599	580	Different	N7	5,445	B
N1	S6	739	580	Different	S5	6,037	A
N2	N5	1,472	580	Different	S6	5,177	B
N2	N7	1,665	580	Different			
N2	S5	2,258	580	Different			
N2	S6	1,397	580	Different			
N5	N7	193	580	Equal			
N5	S5	785	580	Different			
N5	S6	75	580	Equal			
N7	S5	592	580	Different			
N7	S6	268	580	Equal			
S5	S6	860	580	Different			

A.4: N_f ANOVA and Tukey Kramer Analysis

Table A.4.1: N_f ANOVA

Microstrain	N1 (GTRDry)	N2 (GTRWet)	N5 (Aramid)	N7 (Ctrl)	S5 (DryPlastic)	S6 (WetPlastic)	Variation	Sum of Squares	Degrees of Freedom	Mean Squares	F	$F_{critical}$
400	999,997	N/A	1,050,000	1,869,999	964,999	1,465,000	Between Groups	4.94E+11	4	1.23E+11	0.40	3.48
	437,999	N/A	1,970,000	1,224,996	1,079,998	1,150,000	Within Groups	3.10E+12	10	3.10E+11		
	569,997	N/A	494,997	382,500	959,999	321,497	Total	3.60E+12	14			
600	113,499	825,997	87,700	101,496	53,398	105,497	Between Groups	2.24E+12	5	4.49E+11	24.25	3.11
	179,998	1,409,996	189,997	277,500	29,348	194,500	Within Groups	2.22E+11	12	1.85E+10		
	189,496	974,999	186,998	90,000	39,947	106,500	Total	2.46E+12	17			
800	18,846	129,998	18,199	26,449	18,799	9,110	Between Groups	1.56E+10	5	3.12E+09	5.54	3.11
	43,698	128,500	12,147	31,900	16,299	31,196	Within Groups	6.75E+09	12	5.62E+08		
	47,947	35,596	12,450	26,349	6,168	13,599	Total	2.23E+10	17			
1000	N/A	32,797	N/A	N/A	N/A	N/A	Between Groups	N/A	N/A	N/A	N/A	N/A
	N/A	26,447	N/A	N/A	N/A	N/A	Within Groups	N/A	N/A	N/A		
	N/A	16,546	N/A	N/A	N/A	N/A	Total	N/A	N/A			

Table A.4.2: N_f Tukey Kramer Analysis

Microstrain	Comparison		Absolute Difference	Critical Range				
	N1	N2				N1	669,331	A
	N1	N5	502,335	1,526,892	Equal	N2		
	N1	N7	489,834	1,526,892	Equal	N5	1,171,666	A
	N1	S5	332,334	1,526,892	Equal	N7	1,159,165	A
	N1	S6	309,501	1,526,892	Equal	S5	1,001,665	A
	N2	N5				S6	978,832	A
	N2	N7						
400	N2	S5						
	N2	S6						
	N5	N7	12,501	1,526,892	Equal			
	N5	S5	170,000	1,526,892	Equal			
	N5	S6	192,833	1,526,892	Equal			
	N7	S5	157,500	1,526,892	Equal			
	N7	S6	180,333	1,526,892	Equal			
	S5	S6	22,833	1,526,892	Equal			
	N1	N2	909,333	372,825	Different	N1	160,998	B
	N1	N5	6,099	372,825	Equal	N2	1,070,331	A
	N1	N7	4,666	372,825	Equal	N5	154,898	B
	N1	S5	120,100	372,825	Equal	N7	156,332	B
	N1	S6	25,499	372,825	Equal	S5	40,898	B
	N2	N5	915,432	372,825	Different	S6	135,499	B
	N2	N7	913,999	372,825	Different			
600	N2	S5	1,029,433	372,825	Different			
	N2	S6	934,832	372,825	Different			
	N5	N7	1,434	372,825	Equal			
	N5	S5	114,001	372,825	Equal			
	N5	S6	19,399	372,825	Equal			
	N7	S5	115,434	372,825	Equal			
	N7	S6	20,833	372,825	Equal			
	S5	S6	94,601	372,825	Equal			

Table A.4.2: N_f Tukey Kramer Analysis

800	N1	N2	61,201	65,005	Equal	N1	36,830	AB
	N1	N5	22,565	65,005	Equal	N2	98,031	A
	N1	N7	8,598	65,005	Equal	N5	14,265	B
	N1	S5	23,075	65,005	Equal	N7	28,233	B
	N1	S6	18,862	65,005	Equal	S5	13,755	B
	N2	N5	83,766	65,005	Different	S6	17,968	B
	N2	N7	69,799	65,005	Different			
	N2	S5	84,276	65,005	Different			
	N2	S6	80,063	65,005	Different			
	N5	N7	13,967	65,005	Equal			
	N5	S5	510	65,005	Equal			
	N5	S6	3,703	65,005	Equal			
	N7	S5	14,477	65,005	Equal			
	N7	S6	4,213	65,005	Equal			
	S5	S6	4,213	65,005	Equal			
1000	N1	N2				N1		
	N1	N5				N2	25,263	
	N1	N7				N5		
	N1	S5				N7		
	N1	S6				S5		
	N2	N5				S6		
	N2	N7						
	N2	S5						
	N2	S6						
	N5	N7						
	N5	S5						
	N5	S6						
	N7	S5						
	N7	S6						
	S5	S6						

B.1: E_{68} ANOVA and Tukey Kramer Analysis

Table B.1.1: E_{68} ANOVA

SUMMARY						
Groups	*Count*	*Sum*	*Average*	*Variance*		
N1 (GTRDry)	574	479,972	836	16,921		
N2 (GTRWet)	728	662,991	911	9,507		
N5 (Aramid)	774	882,540	1,140	19,372		
N7 (Ctrl)	790	943,494	1,194	20,359		
S5 (DryPlastic)	649	886,330	1,366	26,267		
S6 (Wet Plastic)	702	912,591	1,300	29,710		
ANOVA						
Source of Variation	*SS*	*df*	*MS*	*F*	*P-value*	*F crit*
Between Groups	144,241,667	5	28,848,333	1,421	0	2
Within Groups	85,492,891	4,211	20,302			
Total	229,734,558	4,216				

Table B.1.2: E_{68} Tukey Kramer Analysis

Comparison		Absolute Difference	Standard Error	q	q_{crit}			
N1	N2	75	5.62	13.25	4.03	Different	N1	F
N1	N5	304	5.55	54.78	4.03	Different	N2	E
N1	N7	358	5.53	64.81	4.03	Different	N5	D
N1	S5	529	5.77	91.72	4.03	Different	N7	C
N1	S6	464	5.67	81.80	4.03	Different	S5	A
N2	N5	230	5.20	44.12	4.03	Different	S6	B
N2	N7	284	5.18	54.79	4.03	Different		
N2	S5	455	5.44	83.65	4.03	Different		
N2	S6	389	5.33	73.04	4.03	Different		
N5	N7	54	5.10	10.61	4.03	Different		
N5	S5	225	5.36	42.04	4.03	Different		
N5	S6	160	5.25	30.42	4.03	Different		
N7	S5	171	5.34	32.11	4.03	Different		
N7	S6	106	5.23	20.22	4.03	Different		
S5	S6	66	5.49	11.97	4.03	Different		

B.2: E_{GB} ANOVA and Tukey Kramer Analysis

Table B.2.1: E_{GB} ANOVA

SUMMARY						
Groups	*Count*	*Sum*	*Average*	*Variance*		
N1 (GTRDry)	574	3,246	6	1.70		
N2 (GTRWet)	728	5,051	7	3.21		
N5 (Aramid)	774	5,538	7	3.60		
N7 (Ctrl)	790	7,661	10	3.75		
S5 (DryPlastic)	649	4,879	8	2.27		
S6 (Wet Plastic)	702	4,826	7	2.48		
ANOVA						
Source of Variation	*SS*	*df*	*MS*	*F*	*P-value*	*F crit*
Between Groups	17047.7	5	3409.54	289.347	8.475E-267	2.21622
Within Groups	49620.5	4211	11.7836			
Total	66668.2	4216				

Table B.2.2: E_{GB} Tukey Kramer Analysis

Comparison		Absolute Difference	Standard Error	q	q_{crit}			
N1	N2	1.28	0.14	9.47	4.03	Different	N1	F
N1	N5	1.50	0.13	11.22	4.03	Different	N2	CD
N1	N7	4.04	0.13	30.36	4.03	Different	N5	C
N1	S5	1.86	0.14	13.40	4.03	Different	N7	A
N1	S6	1.22	0.14	8.93	4.03	Different	S5	B
N2	N5	0.22	0.13	1.73	4.03	Equal	S6	D
N2	N7	2.76	0.12	22.12	4.03	Different		
N2	S5	0.58	0.13	4.43	4.03	Different		
N2	S6	0.06	0.13	0.50	4.03	Equal		
N5	N7	2.54	0.12	20.70	4.03	Different		
N5	S5	0.36	0.13	2.81	4.03	Equal		
N5	S6	0.28	0.13	2.22	4.03	Equal		
N7	S5	2.18	0.13	16.94	4.03	Different		
N7	S6	2.82	0.13	22.42	4.03	Different		
S5	S6	0.64	0.13	4.87	4.03	Different		

B.3: $E_{Subgrade}$ ANOVA and Tukey Kramer Analysis

Table B.3.1: $E_{Subgrade}$ ANOVA

SUMMARY						
Groups	*Count*	*Sum*	*Average*	*Variance*		
N1 (GTRDry)	574	15,765	27	12.01		
N2 (GTRWet)	728	20,040	28	14.26		
N5 (Aramid)	774	22,698	29	21.02		
N7 (Ctrl)	790	24,988	32	7.98		
S5 (DryPlastic)	649	16,735	26	6.74		
S6 (Wet Plastic)	702	18,512	26	7.79		
ANOVA						
Source of Variation	*SS*	*df*	*MS*	*F*	*P-value*	*F crit*
Between Groups	17047.7	5	3409.54	289.347	8.475E-267	2.21622
Within Groups	49620.5	4211	11.7836			
Total	66668.2	4216				

Table B.3.2: $E_{Subgrade}$ Tukey Kramer Analysis

Comparison		Absolute Difference	Standard Error	q	q_{crit}			
N1	N2	0.06	0.14	0.46	4.03	Equal	N1	C
N1	N5	1.86	0.13	13.92	4.03	Different	N2	C
N1	N7	4.17	0.13	31.30	4.03	Different	N5	B
N1	S5	1.68	0.14	12.08	4.03	Different	N7	A
N1	S6	1.09	0.14	8.01	4.03	Different	S5	E
N2	N5	1.80	0.13	14.35	4.03	Different	S6	D
N2	N7	4.10	0.12	32.91	4.03	Different		
N2	S5	1.74	0.13	13.29	4.03	Different		
N2	S6	1.16	0.13	9.01	4.03	Different		
N5	N7	2.31	0.12	18.78	4.03	Different		
N5	S5	3.54	0.13	27.40	4.03	Different		
N5	S6	2.96	0.13	23.36	4.03	Different		
N7	S5	5.85	0.13	45.46	4.03	Different		
N7	S6	5.26	0.13	41.79	4.03	Different		
S5	S6	0.58	0.13	4.42	4.03	Different		

B.4: $\mu\varepsilon_{cor}$ ANOVA and Tukey Kramer Analysis

Table B.4.1: $\mu\varepsilon_{cor}$ ANOVA

SUMMARY						
Groups	*Count*	*Sum*	*Average*	*Variance*		
N1 (GTRDry)	73	46,005	630	5,166.16		
N2 (GTRWet)	68	39,511	581	5,339.66		
N5 (Aramid)	61	25,762	422	40,183.91		
N7 (Ctrl)	68	20,537	302	3,203.02		
S5 (DryPlastic)	38	14,345	377	1,611.97		
S6 (WetPlastic)	59	24,455	414	2,674.58		
ANOVA						
Source of Variation	*SS*	*df*	*MS*	*F*	*P-value*	*F crit*
Between Groups	5267083.429	5	1053417	106.5182	7.59244E-69	2.23899
Within Groups	3570125.851	361	9889.55			
Total	8837209.28	366				

Table B.4.2: $\mu\varepsilon_{cor}$ Tukey Kramer Analysis

Comparison		Absolute Difference	Standard Error	q	q_{crit}			
N1	N2	49.17	11.85	4.15	4.05	Different	N1	A
N1	N5	207.88	12.20	17.04	4.05	Different	N2	B
N1	N7	328.20	11.85	27.69	4.05	Different	N5	C
N1	S5	252.71	14.07	17.97	4.05	Different	N7	D
N1	S6	215.71	12.31	17.52	4.05	Different	S5	C
N2	N5	158.71	12.40	12.80	4.05	Different	S6	C
N2	N7	279.03	12.06	23.14	4.05	Different		
N2	S5	203.54	14.24	14.29	4.05	Different		
N2	S6	166.54	12.51	13.31	4.05	Different		
N5	N7	120.32	12.40	9.70	4.05	Different		
N5	S5	44.83	14.53	3.09	4.05	Equal		
N5	S6	7.83	12.84	0.61	4.05	Equal		
N7	S5	75.49	14.24	5.30	4.05	Different		
N7	S6	112.49	12.51	8.99	4.05	Different		
S5	S6	37.01	14.63	2.53	4.05	Equal		